

INTEGRATING WORLDVIEW-3, ASTER AND AEROMAGNETIC DATA FOR LINEAMENT STRUCTURAL INTERPRETATION AND TECTONIC EVOLUTION OF THE HAIB AREA, NAMIBIA

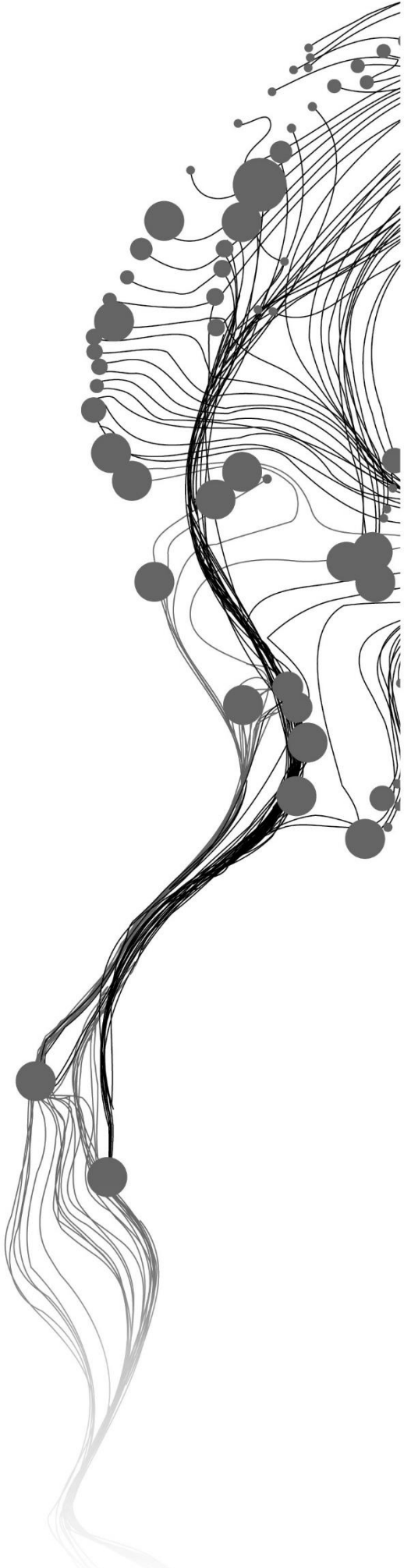
EMMANUEL CHINKAKA

February 2019

SUPERVISORS:

Dr. Robert Hewson

Prof. Dr. Mark van der Meijde



INTEGRATING WORLDVIEW-3, ASTER AND AEROMAGNETIC DATA FOR LINEAMENT STRUCTURAL INTERPRETATION AND TECTONIC EVOLUTION OF THE HAIB AREA, NAMIBIA

EMMANUEL CHINKAKA

Enschede, The Netherlands, February 2019

Thesis submitted to the Faculty of Geo-Information Science and Earth Observation of the University of Twente in partial fulfilment of the requirements for the degree of Master of Science in Geo-information Science and Earth Observation.

Specialization: Applied Earth Sciences – Geological Remote Sensing

SUPERVISORS:

Dr. Robert Hewson

Prof. Dr. Mark van der Meijde

THESIS ASSESSMENT BOARD:

Prof. Dr. F.D. van der Meer (Chair)

Dr. Martin Schodlok (External Examiner, BGR, Germany)

DISCLAIMER

This document describes work undertaken as part of a programme of study at the Faculty of Geo-Information Science and Earth Observation of the University of Twente. All views and opinions expressed therein remain the sole responsibility of the author and do not necessarily represent those of the Faculty.

ABSTRACT

Structural lineament interpretation helps in the understanding of the tectonic and geodynamic processes of an area. Optical remote sensing datasets such as ASTER and WorldView-3 multispectral data are typically used in highlighting regional and local geological lineament structures. However, these datasets do not provide subsurface structural information because they are affected by surface distortions such as vegetation and manmade linear features. Subsurface lineament structures are critical for tectonic interpretation and can be extracted using geophysical data. As such, joint interpretation of lineaments extracted from optical remote sensing and geophysical data provides an enhancement and confidence in the understanding of the tectonic framework of an area.

The study derived a tectonic evolution and geodynamic model of the Haib prospective study area, southern Namibia by integrating geological lineament structures delineated from ASTER, WorldView-3 and magnetic data together with the previously published geological and structural map of the area to improve the tectonic understanding of the area. Integrating these datasets is very useful since the limitations of one dataset are overcome by the other, thus providing a robust compilation of structural information. The study area is of interest because of its mineral and exploration significance as it hosts a Precambrian copper porphyry deposit. Furthermore, the area is a semi-arid region that provides favourable conditions for optical remote sensing. As such, a better understanding of the tectonic lineament structures in the Haib area is very important for mineral exploration purposes. The structural lineaments were automatically extracted from ASTER and WorldView-3 principal component orthogonal bands using the PCI Geomatica LINE Module algorithm. The field-based faults on the published geological map were used as reference in the LINE Module algorithm parameter adjustment process to extract the lineaments. The lineaments extracted from ASTER and WorldView-3 optical remote sensing data were compared in terms of spatial pattern, orientation, length and frequency in order to assess how different these datasets are in mapping structural lineaments. Furthermore, these lineaments were compared in their placement to the ones automatically extracted by utilizing a collocated method of enhancing lineament-related gradients from magnetic maps. To produce a new structural map of the area, the lineaments delineated from all the datasets and the faults from the previously published geological map were integrated for tectonic and geodynamic interpretation of the study area. The following integration criteria was undertaken: collocation of lineaments from at least two of the datasets; lineaments correlation with the topographic expression, and lineament connectivity. A total of three ASTER band ratios and hill-shaded Digital Elevation Models were used in the verification and interpretation of the integrated lineaments.

Analysis and interpretation indicated that ASTER and WorldView-3 data extracted lineaments differently due to differences in the image solar acquisition angles, and seasons and spectral variations. However, orientation patterns of WorldView-3 and magnetics lineaments were found to be similar compared to ASTER extracted lineaments. The proposed tectonic evolution and geodynamics indicated that the study area is controlled by two main fault systems, trending NE-SW representing the Orange River Orogeny (2.0-1.7Ga) and the NW-SE regional trend that represent the Namaqua Orogeny (1.4-1.1Ga), overprinting the previous structures. These lineaments were formed under the compressional tectonic stress regimes generated during these tectonic events. Finally, analysis of the two-dimensional (2D) schematic models revealed topographic lows within the crustal blocks which may be related to the Namaqua Wilson Cycle extension and spreading (1.6-1.2Ga). The integration of the results obtained in this study and literature gave structural insight into the tectonic evolution and geodynamics of the Haib area.

ACKNOWLEDGMENTS

I would like to express my heartfelt gratitude to my supervisors: Dr. Robert Hewson, and Prof. Dr. Mark van der Meijde for their untiring support, guidance and fruitful discussions throughout my MSc research period. Their advice shaped this work and made it a success. Besides my supervisors, I would like to thank Dr. Islam Fadel for the advice and encouragement when my research journey got rough.

My sincere thanks go to the DigitalGlobe Foundation Inc. for providing and supporting this research work with WorldView-3 multispectral optical data and the Geological Surveys of Namibia for providing us with the aeromagnetic data and geological map.

Special thanks to my family: my mother, Mrs. E. Chinkaka, my brothers: Lawrence, Peter, Patrick and Gerald, and my sisters: Joyce and Patricia for all the love and support rendered during my MSc study. I am also grateful to my best friend Ruth 'Theoma' Mangulenje for the love and encouragement throughout my study period.

Above all, from the depths of my heart, I give thanks and glory to God for giving me strength and grace throughout my studies at ITC, University of Twente. Surely, the Lord cares.

**I dedicate this thesis to my dearest mother,
Mrs Elizabeth Chinkaka.
The strongest woman on Earth.
I love you mum**

TABLE OF CONTENTS

Abstract	i
Acknowledgements	ii
Table of contents	iii
List of figures.....	v
List of tables	viii
1. INTRODUCTION.....	1
1.1. Background.....	1
1.2. Problem statement	2
1.3. Research objectives	3
1.4. Research questions	3
1.5. Thesis structure.....	3
2. STUDY AREA AND DATASETS	4
2.1. Location of study area	4
2.2. Tectonic framework of southern Africa region	4
2.3. Regional structural and tectonic setting of the study area.....	5
2.4. Geology of the study area	6
2.5. Dataset description.....	7
3. METHODOLOGY	9
3.1. Introduction	9
3.2. Data pre-processing.....	10
3.3. Geological lineament structural mapping.....	12
3.4. Principal component analysis.....	12
3.5. ASTER and WorldView-3 data automatic lineaments structural mapping.....	13
3.6. ASTER and WorldView-3 data automatic lineaments comparison and analysis.....	15
3.7. Aeromagnetic data automatic lineaments structural mapping.....	16
3.8. Analysis and Interpretation of ASTER and WorldView-3 automatic extracted lineaments.....	18
3.9. Lineaments kinematics and sense of motion of ASTER, WorldView-3 and Magnetic data	19
3.10. Lineaments integration from ASTER, WorldView-3 and magnetic data.....	19
3.11. ASTER band ratios	20
4. RESULTS	21
4.1. Principal component analysis.....	21
4.2. ASTER and WorldView-3 data automatic lineaments structural mapping.....	22
4.3. ASTER and WorldView-3 data automatic lineaments comparison and analysis.....	23
4.4. Aeromagnetic data automatic lineaments structural mapping.....	25
4.5. Analysis and interpretation of ASTER and WorldVieww-3 automatic extracted lineaments	28
4.6. Lineaments kinematics and sense of motion of ASTER, WorldView-3 and Magnetic data	29
4.7. Lineaments integration from ASTER, WorldView-3 and Magnetic data.....	32
4.8. ASTER Band ratios.....	36
5. TECTONIC EVOLUTION AND GEODYNAMIC INTERPRETATION.....	37
5.1. Introduction	37
5.2. Tectonic evolution	37
5.3. Tectonic evolution and geodynamic model interpretation	39

6.	DISCUSSION.....	44
6.1.	Introduction	44
6.2.	Similarities and differences of the ASTER and WorldView-3 extracted lineaments	44
6.3.	Comparison of ASTER, WorldView-3 and magnetic lineaments kinematics, sense of motion and tectonic implications	45
6.4.	Tectonic evolution and geodynamics of Haib area	46
7.	CONCLUSION AND RECOMMENDATION	47
7.1.	Conclusion.....	47
7.2.	Recommendation	49
	List of references	50
	Appendix.....	54

LIST OF FIGURES

Chapter 2

Figure 2-1: False Colour Composite of WorldView-3 image (RGB = 753) showing the Haib area	4
Figure 2-2: Simplified tectonic framework of Southern Africa (modified after Schijndel, 2013) showing the Richtersveld Sub-province. The insert map shows the boundary of Namibia and the location of the Haib study area within the Richtersveld Sub-province	5
Figure 2-3: The tectonic subdivisions of the Namaqua – Natal Province, modified after Cornell et al., 2006	6
Figure 2-4: Geology of the Haib area modified after (Blignault, 1972) and Barr & Reid (1992).	7
Figure 2-5: Earth observation datasets: SRTM DEM(a), Reduced to pole magnetic data(b), ASTER False Colour Composite (RGB) = 321 and WorldView-3 False Colour Composite (RGB) = 753.....	8

Chapter 3

Figure 3-1: Summarised workflow of the research (Note: TDHR = Total horizontal derivative of the tilt angle, TDXN = Normalized total horizontal derivative and NSTD = Normalized standard derivative of the reduced to pole data).....	9
Figure 3-2: FCC (RGB = 753) WorldView-3 VNIR(a), NDVI result for WorldView-3 VNIR showing highlighted green vegetation(b), FCC (RGB = 321) ASTER(c) and NDVI result for ASTER image with no green vegetation highlighted(d)	10
Figure 3-3: Hill shaded SRTM DEM images at different illumination directions (00, 450, 900 and 1350) a, b, c and d respectively represented by blue arrows. The weighted summed multidirectional shaded image shown in (e).	11
Figure 3-4: Execution flowchart for the LINE Module algorithm automatic lineaments extraction.....	14

Chapter 4

Figure 4-1: ASTER PC1, unclear and blurry(a), ASTER PC2, from where the lineaments were automatically extracted(b), World View-3 PC1, from where the lineaments were automatically extracted(c) and WorldView-3's PC2, unclear and blurry, with the middle line showing the effect of image mosaicking(d)	21
Figure 4-2: ASTER automatic extracted lineaments overlaid on ASTER PC 2 image.....	22
Figure 4-3: WorldView-3 automatic extracted lineaments overlaid on WorldView-3 PC 1 image.....	22
Figure 4-4: Lineament maps extracted from ASTER data overlaid on ASTER PC2 image(a) and WorldView-3 data overlaid on WorldView-3 PC1 (b) showing the distribution patterns of the extracted lineaments, with a few examples of similar extracted lineaments in yellow solid circles and different lineaments in green dotted circles.....	23
Figure 4-5: Rose diagrams extracted from ASTER data (a) and WorldView-3 data (b) Note the general orientations in the NW-SE dominant direction and the minor NE-SW direction, more pronounced in the ASTER in NNE-SSW direction.....	24
Figure 4-6: Lineaments length and frequency histograms extracted from ASTER (a) and WorldView-3 (b) datasets showing a similar right skewed frequency distribution.....	25
Figure 4-7: Reduced to pole magnetic input data (a), Normalised standard deviation (NSTD) derivative of the input data (b), Total horizontal derivative of the tilt angle (TDHR) (c) and the normalised horizontal derivative (TDXN) (d). These derivatives (b, c and d) were collocated to delineate lineaments	26

Figure 4-8: Automatic extracted magnetic lineament structures overlaid on First Vertical Derivative (FVD) of the Reduced to Pole (RTP)	26
Figure 4-9: Rose diagram from magnetic extracted lineaments showing dominant NW-SE direction and NE-SW minor direction	27
Figure 4-10: ASTER interpreted lineaments showing main linear features in the study area.....	28
Figure 4-11: WorldView-3 interpreted lineaments showing main linear features in the study area.....	29
Figure 4-12: The ASTER lineament kinematics and sense of motion showing strike-slip faulting. The yellow arrows show the movement of the lineaments. (Inserts show evidence of strike slip motion of the lineaments).....	30
Figure 4-13: The WorldView-3 lineament kinematics and sense of motion showing strike-slip faulting. The yellow arrows show the movement of the lineaments. (Inserts show evidence of strike slip motion of the lineaments).....	30
Figure 4-14: The Magnetics lineament overlaid on the Reduced to pole (RTP) grid showing strike-slip sense of motion. The yellow arrows show the movement of the lineaments (Inserts indicate evidence of strike slip motion of the lineaments)	31
Figure 4-15: Shows the kinematics of lineaments in ASTER data (a), WorldView-3 data(b) and Magnetic data(c) (Note that the NW and NE trend lines represent the NW-SE and NE-SW lineaments in each dataset based on their corresponding Rose diagram orientation angles	32
Figure 4-16: Integrated lineaments from ASTER, WorldView-3 and Magnetics with NW-SE and NE-SW spatial patterns draped over a hill-shaded SRTM DEM and the Rose diagram showing dominant NW-SE and NE-SW orientations more pronounced at 285 and 45 degrees respectively.....	33
Figure 4-17: The combination of old (published) and new lineaments to produce the new structural map of Haib area; (A) Faults from the published structural map by Blignault, (1972) (B) Lineament delineated from this study (C) The new structural map of Haib area based on the analysis as presented in this study and published map (Blignault, 1972)	34
Figure 4-18: Haib study area lineaments kinematics diagram (A) and sense of motion (B) derived from integrated lineaments from ASTER, WorldView-3, Magnetic data and previously published structural map	35
Figure 4-19: ASTER Cudahy (2012) band ratio-based algorithm (a) Al-OH mineral group content (b) Mg-OH/Carbonate mineral group content (c) Ferric oxide mineral content (d) RGB combination of Al-OH, Mg-OH/Carbonate, Ferric oxide with the lineaments showing the structural relationship	36

Chapter 5

Figure 5-1: Major tectonic events in the study area (A) Collision of San Francisco and Congo Cratons forming NE-SW ductile strike-slip faulting of the Orange River Orogeny (2.0 – 1.7Ga) (B) Collision of the Namaqualand and Zimbabwe-Kaapvaal Craton forming NW-SE ductile strike-slip faulting of the Namaqua Orogeny (1.4-1.1Ga) after Thomas et al., (1993) and Cornell et al.,(2006).....	38
Figure 5-2: Geodynamic interpretation of the Haib area, with the topographical expression (cross section lines A, B and C) and the delineated lineaments from this study over the lithological formations. The compressional forces A, B, C and D in the NW-SE and NE-SW are representing the Orange River and Namaqua tectonic force directions respectively. The smaller red arrows represent extensional forces from the Namaqua Wilson Cycle.....	39
Figure 5-3: A cross-section of the topographical (geomorphological landform) impression and tectonic model across Lower feldspar porphyry and Upper feldspar porphyry units.	40
Figure 5-4: A cross-section of the topographical (geomorphological landform) impression and tectonic model across the Granitoid, Upper feldspar porphyry, Amphibolite and Lower feldspar porphyry.	40

Figure 5-5: A cross-section of the topographical (geomorphological landform) impression and tectonic model across the Undifferentiated granite through the Leucocratic granite to another unit of the Undifferentiated granite.....41

Figure 5-6: Proposed tectonic evolution model sketch of Haib area from 2.0 Ga to 1.1 Ga (a)Shows pre-Paleoproterozoic tectonic state with emplacement of the Orange River Group (b) Paleoproterozoic tectonism of the Orange River Orogeny with NW-SE compression force causing strike-slip faulting (c) Prolonged plutonism and deformation creates a weaker zone and extension in the Namaquan Wilson Cycle that resulted in the intrusion (amphibolite intrusion) and the Vioolsdrift and Richtersveld Intrusive Suites (d)The Mesoproterozoic compression of the Namaqua Orogeny with NE-SW tectonic force direction causing strike-slip faulting. (Note: the starting geology in (a) is not fully known and based on Barr & Reid 1992).....43

LIST OF TABLES

Chapter 2

Table 2-1: A summary of the data specifications used in this study (a detailed description of these datasets is given in appendix VIII).....	8
--	---

Chapter 3

Table 3-1: Differences between Automatic and Manual lineament extraction approaches after Hung et al., (2005).....	13
--	----

Table 3-2: Optimal parameters for the automatic lineament extraction for ASTER and WorldView-3 data	15
---	----

Table 3-3: Cudahy (2012) defined algorithm for ASTER data for Al-OH, Mg-OH/Carbonate and FeO mineral content groups	20
---	----

Chapter 5

Table 5-1: Characterisation of the observed structures in Haib area and their corresponding mechanisms and tectonic events based on the structural results from this study, Cornell et al., 2006, Sithole 2013, Macey 2017 and Thomas et al., 1993.....	42
---	----

1. INTRODUCTION

1.1. Background

Multiple remote sensing data integration in recent years has effectively and increasingly become a useful approach in geological mapping programs. This integration involves datasets that have different spatial and spectral specifications and consequently different abilities in their applications for surface and subsurface mapping (Eldosouky et al., 2017). Optical remote sensing data such as ASTER and WorldView-3 multispectral data play a major role in geological studies by highlight regional and local geological lineament structures; however, this data does not provide subsurface geological information. Such information can be extracted using geophysical data (Bahiru & Woldai, 2016). As such, joint interpretation of remote sensing and geophysical data helps in mapping the surface and subsurface geological structures to improve the understanding of the tectonic framework of an area (Yeomans et al., 2018).

Geological structural lineaments mapping plays a vital role in geological studies, especially in mineral exploration, mining, and petroleum industry. Most detailed geological studies involve an understanding of lineament and subsurface geological information because they are often associated with mineral deposit emplacement and tectonic evolution processes (Meshkani et al, 2013). According to Adiri et al. (2017), lineament structural features may correspond to natural objects, including structural alignment, geomorphologic consequences, structural weakness, faults, fractures, dykes, granitic or porphyry intrusions, bedding planes and lithological boundaries separating different formations. Such geological structures are important because they contribute to the understanding of the crustal tectonic evolution and distribution of mineralization (Eberle, Andritzky, & Wackerle, 1995). Remote sensing datasets have been frequently used in geological structural mapping. For example, Chaabouni et al., (2012) focused on geological lineament mapping in the Jenein area, southern Sudan using edge detection and edge linking algorithms developed by Argialas et al., (2003) on Landsat TM and ETM+ multispectral images. Mdala (2015), applied LINE Module and TecLine algorithms in extracting lineaments using ASTER, Landsat ETM⁺ 7 and Shuttle Radar Topography Mission (SRTM) Digital Elevation Model (DEM) in the southern and northern provinces of Malawi, situated on the western branch of the East African Rift System (EARS).

Normally, processing optical remote sensing datasets such as ASTER and WorldView-3, as pointed out earlier, only provides surface information. But deep-seated geological lineament structures, which are ultimately important for tectonic modeling, are revealed and delineated by geophysical data such as aeromagnetic data because it is not influenced by surface distortions (Eldosouky et al., 2017). However, Hung et al., (2005) argue that geological surface linear structures observed from optical remote sensing images may reflect the subsurface geology. And importantly, for structural interpretation and tectonic evolution, it is interesting to understand how subsurface structures are shaped in relation to mineral occurrence and lineament structures. This subsurface structural information can be extracted from gravity or aeromagnetic data using several techniques. For example, Almasi et al. (2014), discusses techniques such as reduced to pole, upward continuation, and edge detection filters like analytical signal, vertical, horizontal and tilt derivative calculations. Chisenga (2015), applied these filters on aeromagnetic and gravity data to derive the tectonic boundary structures and geodynamic model of Botswana in the attempt to improve the understanding of its tectonic evolution.

1.2. Problem statement

Research has been done in analyzing and interpreting geological structural lineaments with the attempt to understand the tectonic frameworks of different areas from optical remote sensing and geophysical data. The Landsat Multispectral Scanner remote sensing imagery was used by Csillag & Stogicza (1987), to detect lineament structures for tectonic interpretation in Mecsek Mountains, Hungary. Zhumabek et al., (2017), derived geodynamic models of Ulytau area in Kazakhstan based on the automatically detected lineaments from digital elevation model data. Furthermore, Malik et al., (2018) integrated lineaments delineated from Landsat-7 ETM, SRTM-DEM and aeromagnetic data in interpreting the tectonic deformations in the Shanono Basement Complex, Nigeria. In addition, Sukumar & Nelson (2017) extracted lineaments from ASTER satellite images for mineral exploration studies at Afar Depression region within the East African Rift in Ethiopia. However, no published study has been done combining ASTER and the newly launched WorldView-3 multispectral satellite data together with aeromagnetics in mapping geological lineament structures. At the same time, there is no research work on the structural interpretation of the Haib area, southern Namibia, to understand its tectonic framework. Even though Corner (2000), interpreted the crustal framework of Namibia derived from magnetic and gravity data, the interpretation was based on a regional scale including the offshore areas of the country. As such, the interpretation does not encompass detailed structures of the Haib study area at a local scale such as attempted in this study.

Furthermore, to the knowledge of this research, the Haib area does not have a high resolution integrated tectonic and geodynamic process model derived from multiple datasets of ASTER, WorldView-3, and aeromagnetic data. This model shall help to improve the understanding of the tectonic evolution of the Haib area. Therefore, this research integrates WorldView-3 and ASTER data in combination with high-resolution aeromagnetic data in lineaments structural mapping to understand the tectonic framework in the Haib area, southern Namibia. The Haib area is of interest because of its mineral exploration and mining significance as it hosts a Precambrian porphyry copper mineralization deposit (Anhaeusser, 1990; Ngcofe et al. 2013; Connelly et al., 2018). The deposit was discovered in the 1800s with much interest from the European prospectors. Since the 1950s, a number of exploration companies including the Teck Cominco Namibia Ltd, which conducted several exploration programs in the area including the airborne Hyperspectral mineral alteration mapping program in 2009, but the structural interpretation is still speculative (Connelly et al., 2018; Teck Cominco Namibia Ltd, 2009)

1.3. Research objectives

The main objective of this research is to make an integrated interpretation of WorldView-3 and ASTER remote sensing data in combination with aeromagnetic data in mapping structural lineaments in the Haib area for tectonic framework interpretation. Below are the research specific objectives and questions:

1. To assess the contribution of WorldView-3 and ASTER remote sensing data in geological lineament structural mapping.
2. To analyze the kinematics and sense of motion of lineaments (inferred faults) derived from ASTER, WorldView-3, and aeromagnetic data.
3. To improve the understanding of the tectonic evolution of the study area by combining structural information from ASTER, WorldView-3, and aeromagnetic data.
4. To construct the geodynamic processes model of the study area by integrating structural information from ASTER, WorldView-3, aeromagnetic, topographical and geological data.

1.4. Research questions

1. How comparable are WorldView-3 and ASTER datasets in extracting geological linear structural features in terms of spatial distribution pattern, orientation, length, and frequency?
2. Does each of ASTER, WorldView-3, and aeromagnetic data derive lineaments sense of motion and relative age of the main deformational tectonic episodes?
3. What improvement does the integration of ASTER, WorldView-3, and Aeromagnetic data have on our understanding of the structures and tectonics of the Haib area? Are there new structures identified compared to the published structural map by Blignault (1972)?
4. Can the delineated lineament structures in the study area be linked with the tectonic events that have affected the area?
5. Is it possible to derive the tectonic evolution and geodynamic model of the study area in relation to the tectonic events?

1.5. Thesis structure

Chapter 1: Introduction

Explains the background to the study, the problem statement, research objectives and questions.

Chapter 2: Study area and datasets

Description of the study area including the geology, tectonic setting, and the datasets

Chapter 3: Methodology

A detailed description of the methodology undertaken

Chapter 4: Results

Shows the results obtained in this research

Chapter 5: Tectonic evolution and geodynamic interpretation

This chapter presents the tectonic evolution of the Haib area, and finally, a proposed tectonic evolution model and geodynamic process interpretation.

Chapter 6: Discussion

Discussion of the results obtained in this research and tectonic evolution model

Chapter 7: Conclusion and recommendation

2. STUDY AREA AND DATASETS

2.1. Location of study area

The study area lies within the southern African tectonic region. It is situated in the Karas region southern Namibia, north of the Orange River which is close to the South African border. It occupies approximately 130 square kilometers bounded by $17^{\circ} 45'$ and $17^{\circ} 59'$ East of the prime meridian and latitude $28^{\circ} 37'$ and $28^{\circ} 44'$ South of the Equator. The Haib study area is an arid area with excellent geological exposure that is suitable for remote sensing studies (Ngcofe et al., 2013) (Figure 2-1.)

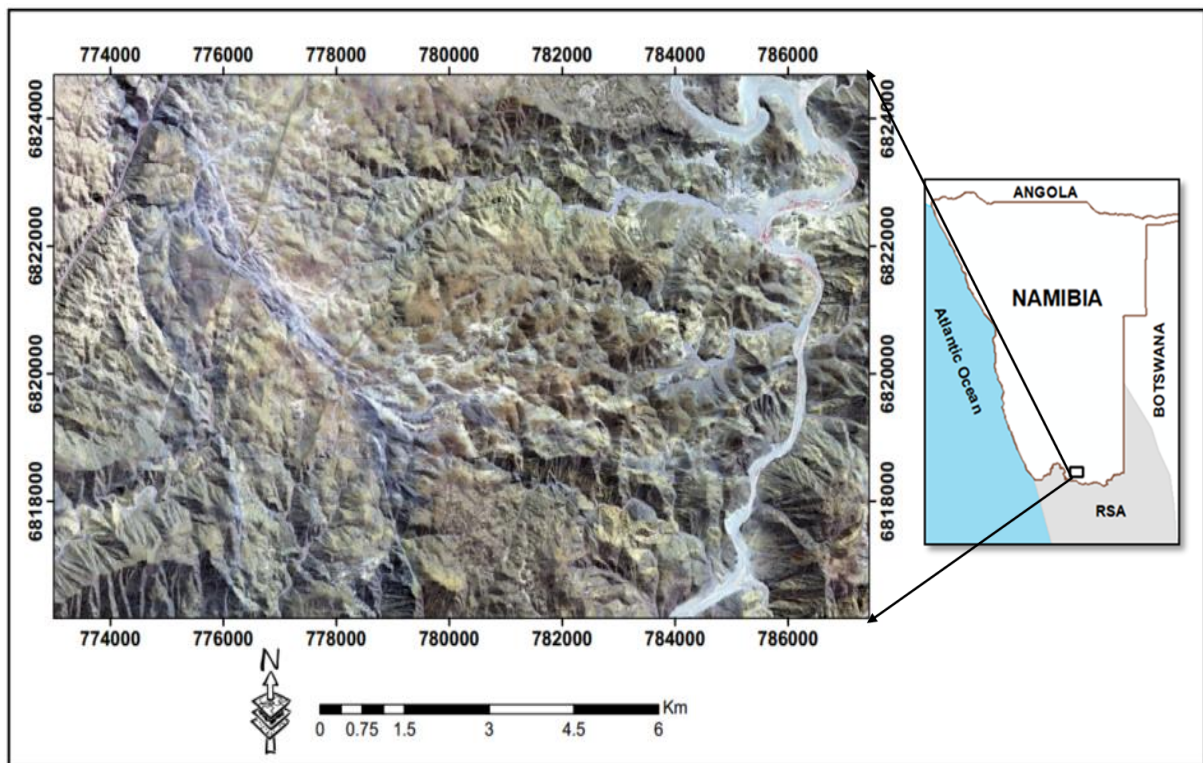


Figure 2-1: False Colour Composite of WorldView-3 image (RGB = 753) showing the Haib area

2.2. Tectonic framework of the southern Africa region

The tectonic framework of Southern Africa as shown in the Figure 2-2 below is made up of several major cratons of the Archean age and smaller cratonic fragments, stitched together by various other younger orogenic mobile belts (Schijndel, 2013). The current configuration state of the tectonic framework was established during the late Neoproterozoic to Cambrian Pan African orogenic event (Begg et al, 2009). The Kalahari craton, which constitutes the main part of Southern Africa covering the countries including Zimbabwe, Botswana, Namibia, South Africa and some parts of Mozambique, is an aggregate of the Kaapvaal and Zimbabwe cratons. This massive craton forms the Archean nucleus and is surrounded by the Proterozoic provinces (Schijndel, 2013; Sithole, 2013). Furthermore, Jacobs et al., (2008) argue that the Kalahari craton has been stable since the Mesoproterozoic times and previously formed part of the Rodinia supercontinent.

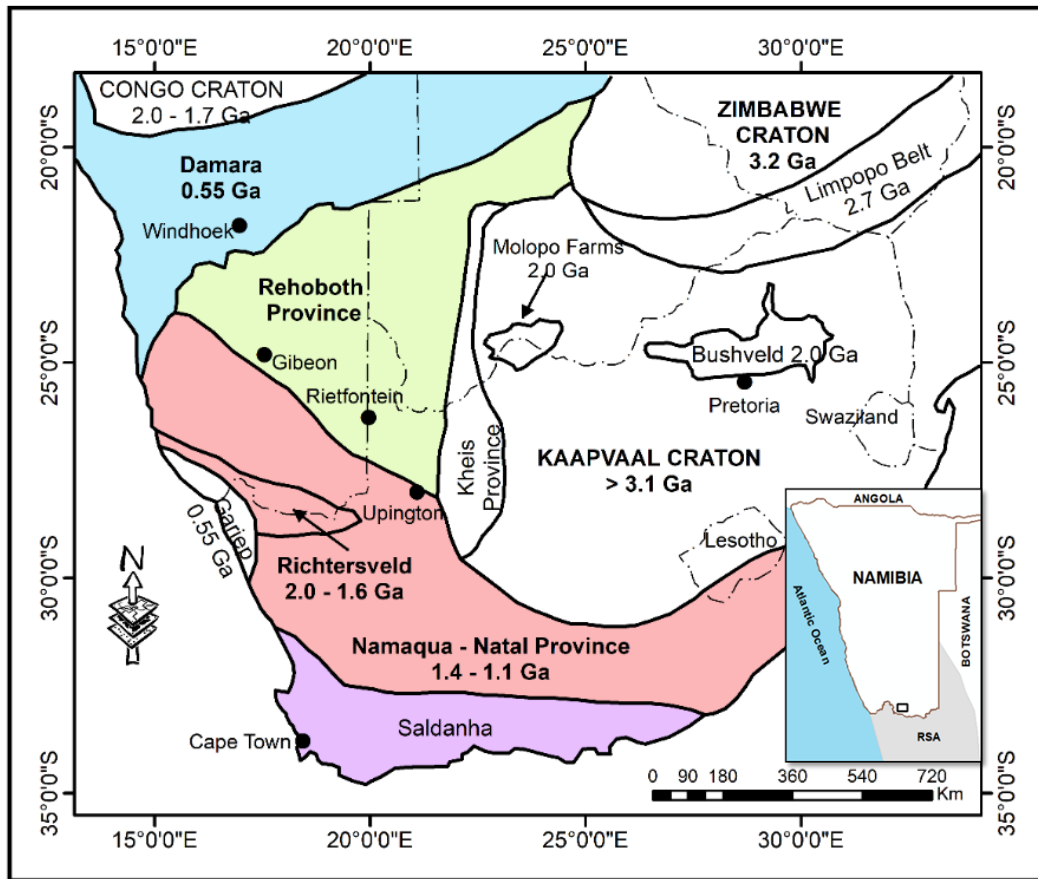


Figure 2-2: A simplified tectonic framework of Southern Africa (modified after Schijndel, 2013) showing the Richtersveld Sub-province. The insert map shows the boundary of Namibia and the location of the Haib study area within the Richtersveld Sub-province

2.3. Regional structural and tectonic setting of the study area

This section summarizes the structural and tectonic setting of the study area as a background to the interpretation and discussion of the results obtained in this research work. The border region between South Africa and Namibia (including the study area) in Figure 2-3 below, straddles tectonostratigraphic terranes that were formed during two different orogenic episodes, these being the Orange River Orogeny (2.0 to 1.7 Ga) and the Namaqua Orogeny (1.4 to 1.1 Ga) (Colliston & Schoch, 2000). The Namaqua-Natal Province is a metamorphic belt that records a complex and extended history of igneous activity and deformation. The structural evolution of terranes in the Namaqua – Natal Province is composed of four-fold phases related to the deformation events (D1 – D4) (Sithole, 2013). The western part of the Namaqua – Natal Province also known as the Namaqua Sector is subdivided into three main tectonostratigraphic terranes namely the Haib hosted Richtersveld terrane, Bushmanland terrane, and the Gariiep terrane. The subdivision is based on marked changes in the lithostratigraphy across structural discontinuities, tectonic history and metamorphic grade (Cornell, 2006; Macey et al., 2017). These terranes display all four major deformation phases. The D1-fabrics within the Richtersveld terrane are thought to have developed in the Paleoproterozoic coeval and have been named the Orange River Orogeny (Blignault, 1977) and preserved in xenoliths in the Goodhouse Suite granites. This early folding event, D1, is seen as isolated fold closures in Bushmanland. The second D2 is dominated by regional recumbent ENE-trending folds, along with the D3 ENE striking open folding. D4 is mainly related to NW trending movements along subvertical shear zones and faults, related to compression from SW and affected by the geometry of the wedge-shaped Kaapvaal Craton around Prieska and not the previous terranes (Sithole, 2013). The D2 to D4 deformations are considered phases of the Mesoproterozoic Namaqua Orogeny and D3 is a kilometer-scale F3 fold structure with localized foliation and lineation (Blignault, 1977).

The Richtersveld Subprovince in the western Namaqualand represent the most extensive area in the southern Africa formed during the 2 Ga the Kheisian (Paleoproterozoic) (NE-SW direction of faulting) known as the Orange River Orogeny, at the same time event of the Eburnean and Ubendian Orogenies elsewhere in Africa (Thomas et al., 1993; Cornell, 2006). An early D1 deformation in this province and Haib area, in particular, is observed with open to isoclinal folds, F1 which are cut by Vioolsdrift granite suite well exposed around Nous in the Vioolsdrift region. The Namaqua orogeny that produced the F2, fold generation refolded F1 into NW-SE directional structures forming low to medium grade supracrustal rocks and intrusions in the NW Namaqua sector. The Richtersveld Subprovince is a tectonically bounded sliver of crust that lies ‘sandwiched’ between the Bushmanland and Kakamas terrenes (Macey et al., 2017). Figure 2-3 below shows the current tectonic subdivisions of the Namaqua – Natal Province.

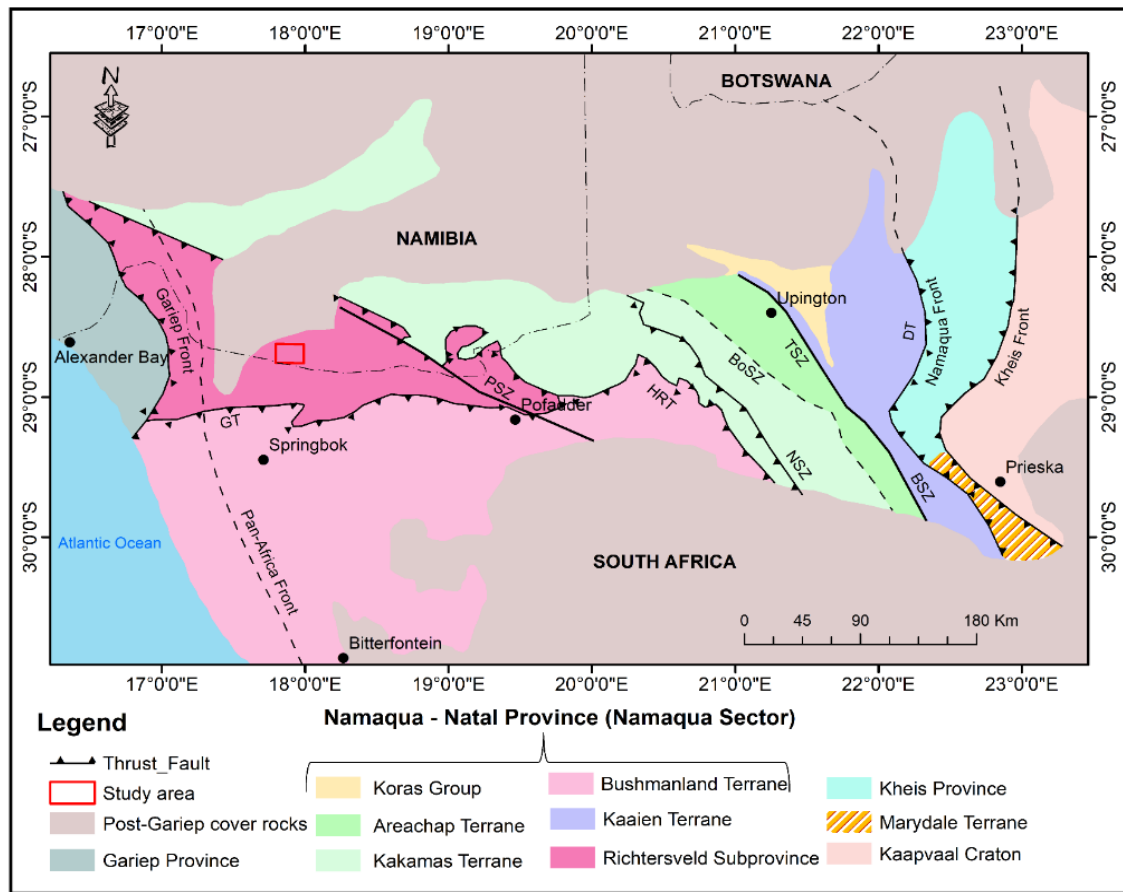


Figure 2-3: The tectonic subdivisions of the Namaqua – Natal Province, modified after Cornell et al., 2006

2.4. Geology of the study area

The Haib area forms part of the Namaqua – Natal Province in the sub-terrane known as the Richtersveld geological sub-province. The Namaqua – Natal is the tectonostratigraphic province that spans 1400 km across South Africa and Namibia and is approximately 400 km wide (Fransson, 2008). It is NW-SE trending Proterozoic metamorphic belt that extends beneath the Phanerozoic Karoo Supergroup (Blignault, 1977). Haib area comprises the regionally greenschist facies of metamorphosed Proterozoic rock units shown in Figure 2-4 (Blignault, 1972). These units are further subdivided into volcano-sedimentary sequence locally known as Orange River Group, Vioolsdrift Intrusive Suite, Richtersveld Intrusive Suite and the Haib recent alluvial cover (Connelly et al., 2018). Geochronologically, the Orange River Group is the oldest rock units in the study area and represents the spectrum of calc-alkaline volcanic rock types, ranging in composition from basalt to rhyolite (Barr & Reid, 1992). It is sub-divided into the Nous Formation and Basal Tsams Formation, which includes the metabasic and metafelsic lavas in the Haib prospect vicinity (Minnitt, 1986).

The Feldspar Porphyry (FP) which host the copper mineralization, volcanic flows of intermediate to acid tuff, metamorphosed tuff, undifferentiated granite, and chert are dominant units of the Orange River Group (Sithole, 2013). The Vioolsdrift Intrusive Suite intrudes into the Orange River Group and consists of the mineralized Quartz Feldspar Porphyry, basic – ultrabasic complexes, diorite, tonalite, granodiorite, adamellite, and leucogranite. These were emplaced during the main two phases of intrusive activities in the Haib area. And the Richtersveld Intrusive Suite intrudes into both the Orange River Group and Vioolsdrift Intrusive Suite forming amphibolite, syenite and granite rocks. All these rock groups were eventually overlain by the Haib recent alluvial sedimentary sequence (Adegboyega, 2016; Indongo, 2017).

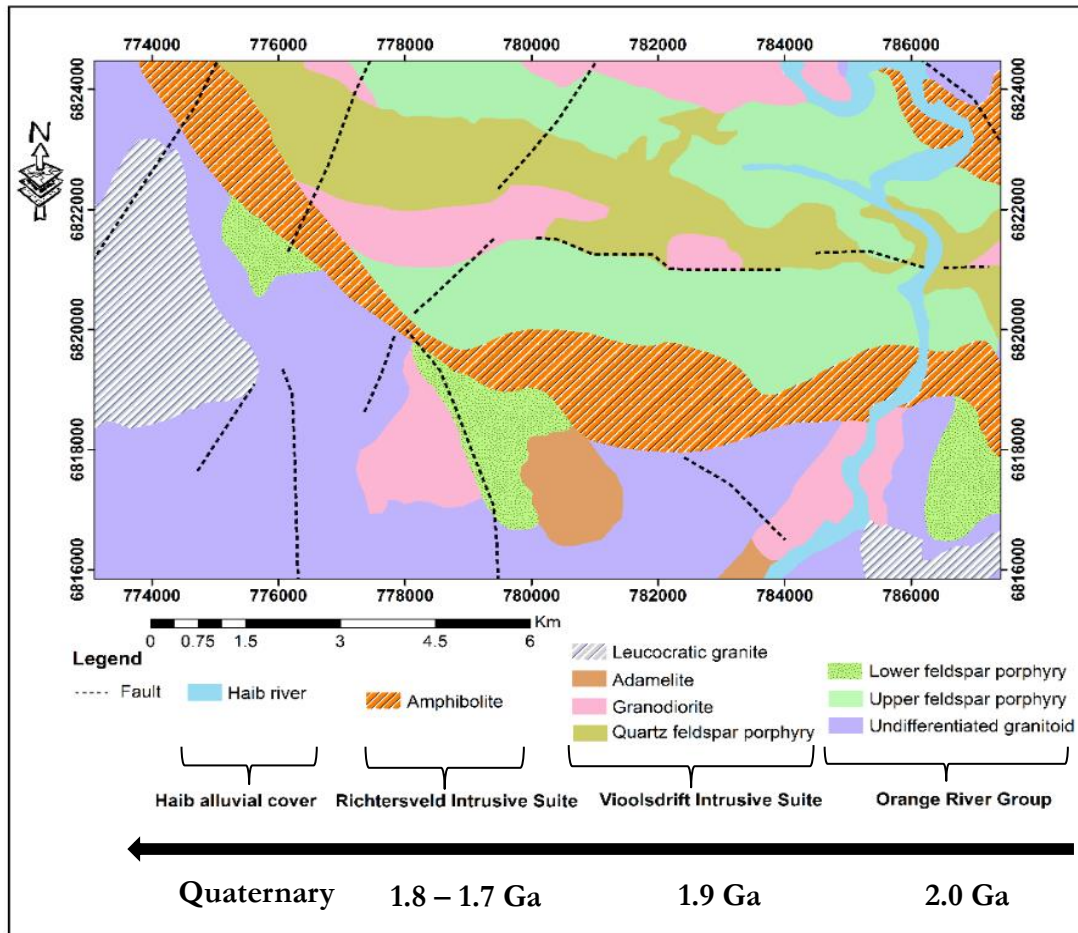


Figure 2-4: Geology of the Haib area modified after (Blignault, 1972) and Barr & Reid (1992).

2.5. Dataset description

This research utilized the multispectral WorldView-3's Visible-Near Infrared (VNIR) data, which is the commercial data provided by the DigitalGlobe Foundation as part of the sponsorship for this research, ASTER VNIR and Short-Wave Infrared (SWIR) freely available data, Shuttle Radar Topography Mission (SRTM) Digital Elevation Model (DEM), published Geological map, and aeromagnetic data. As shown in Table 2-1 below, the WorldView-3 data comprised of two VNIR (radiance-at-sensor) images acquired on the same date, the 18th April 2018. The WorldView-3 sensor covers the VNIR and SWIR ranges at 1.2m and 7.5m spatial resolutions respectively and is the only multispectral sensor with high spatial and spectral resolution on the market so far (Kruse et al., 2000; Liu et al., 2014; Ye et al., 2017). On the other hand, the ASTER data comprised of a total of four scenes Level 2 surface reflectance. This data included two VNIR and two crosstalk corrected SWIR surface reflectance images which were downloaded freely from NASA's Earthdata portal through their website (<https://search.earthdata.nasa.gov/search>).

The two ASTER VNIR-SWIR image pairs over the study area were acquired on the 9th of December 2005 and 18th December 2005. These acquisition dates were chosen to ensure that high sun angle, less vegetation, and cloud-free images are obtained. The ASTER satellite system covers the VNIR, SWIR and Thermal Infrared (TIR) ranges of the electromagnetic spectrum at 15m, 30m, and 90m spatial resolutions respectively. Further details on these datasets are provided in appendix VIII.

Sensor	Swath width (km)	Subsystem	Band number	Spatial resolution (m)
WorldView-3	13.1	Multispectral VNIR	8	1.2
ASTER	60	Multispectral VNIR	3	15
		Multispectral SWIR	6	30
Space Shuttle	-	TOPSAR	-	30
Magnetics	-	-	-	50

Table 2-1: A summary of the data specifications used in this study (a detailed description of these datasets is given in appendix VIII)

The SRTM DEM was obtained from NASA’s Earth Explorer (<https://earthexplorer.usgs.gov/>). The geological map (Figure 2-4) and aeromagnetic data were provided by the Geological Surveys of Namibia. This geological map compiled in 1972 at the scale of 1:100,000 while the aeromagnetic data was collected during the country-wide geophysical campaign in 1994 at 200 meters line spacing, 80 meters flying height and processed into 50 meters resolution grid. All the data used in this research were then co-registered to UTM zone 33S and WGS-84 projection datum. The Figure 2.5 shows earth observation data (SRTM DEM (a), Reduced to pole magnetics (b), ASTER False Colour Composite (FCC) (c) and WorldView-3 False Colour Composite (FCC) (d)) used in this study.

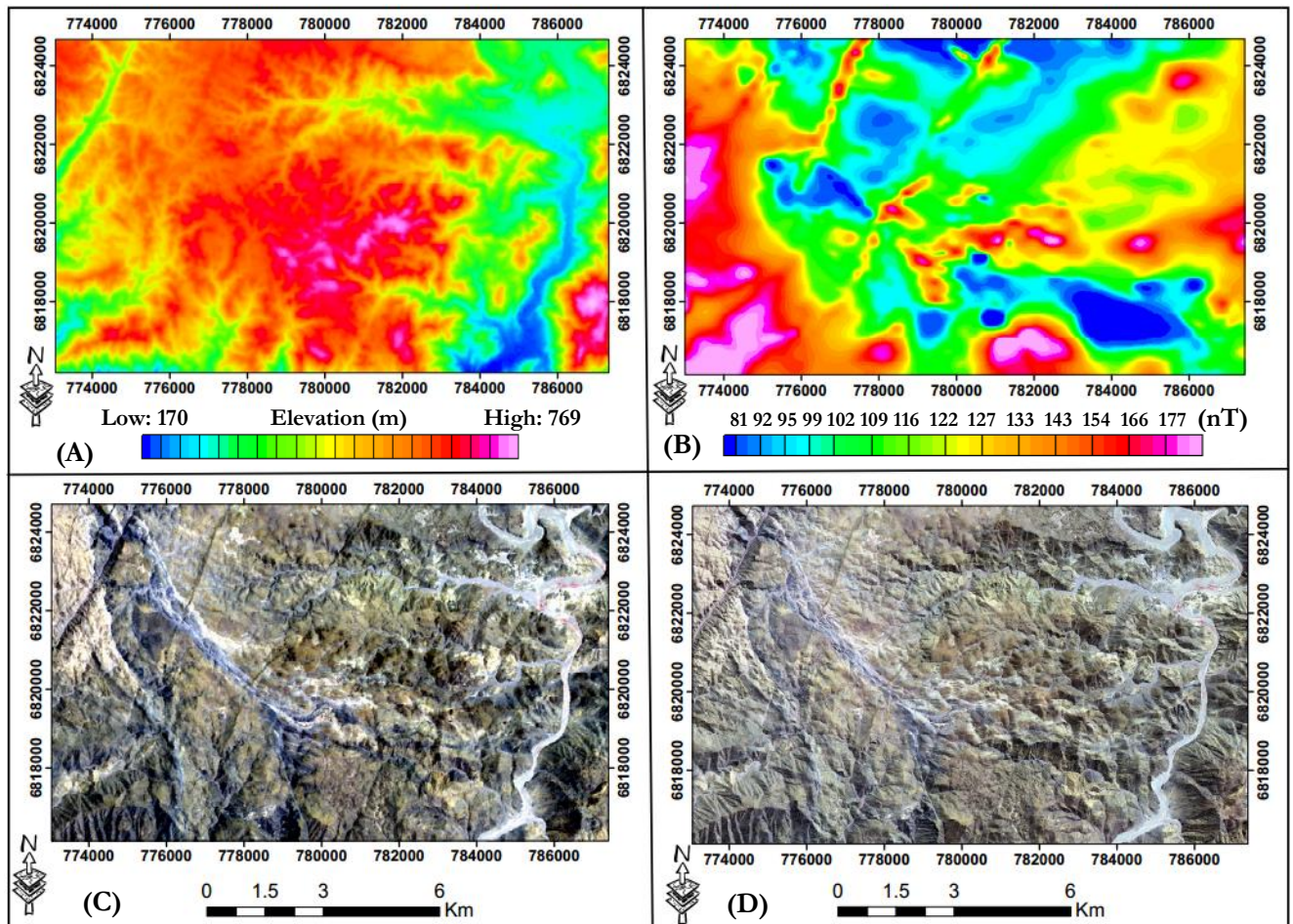


Figure 2-5: Earth observation datasets: SRTM DEM(a), Reduced to pole magnetic data(b), ASTER False Colour Composite (RGB) = 321 and WorldView-3 False Colour Composite (RGB) = 753

3. METHODOLOGY

3.1. Introduction

The main objective of this research was to make an integrated interpretation of ASTER and WorldView-3 remote sensing satellite data in combination with aeromagnetic data in mapping lineaments structures in the Haib area for tectonic interpretation. With regards to this research, “lineaments are considered to be natural surface expressions, resulting from structural alignments, geomorphological processes, structural weaknesses, faults, fractures, dykes, boundaries of granitic or porphyry intrusions, bedding planes and lithological boundaries separating different formations” (Adiri et al., 2017). The methodology used in this research is summarized and shown in the flowchart in Figure 3-1 below. The research used the following datasets: Multispectral WorldView-3, ASTER, SRTM DEM remote sensing data, geological map, and aeromagnetic geophysical data.

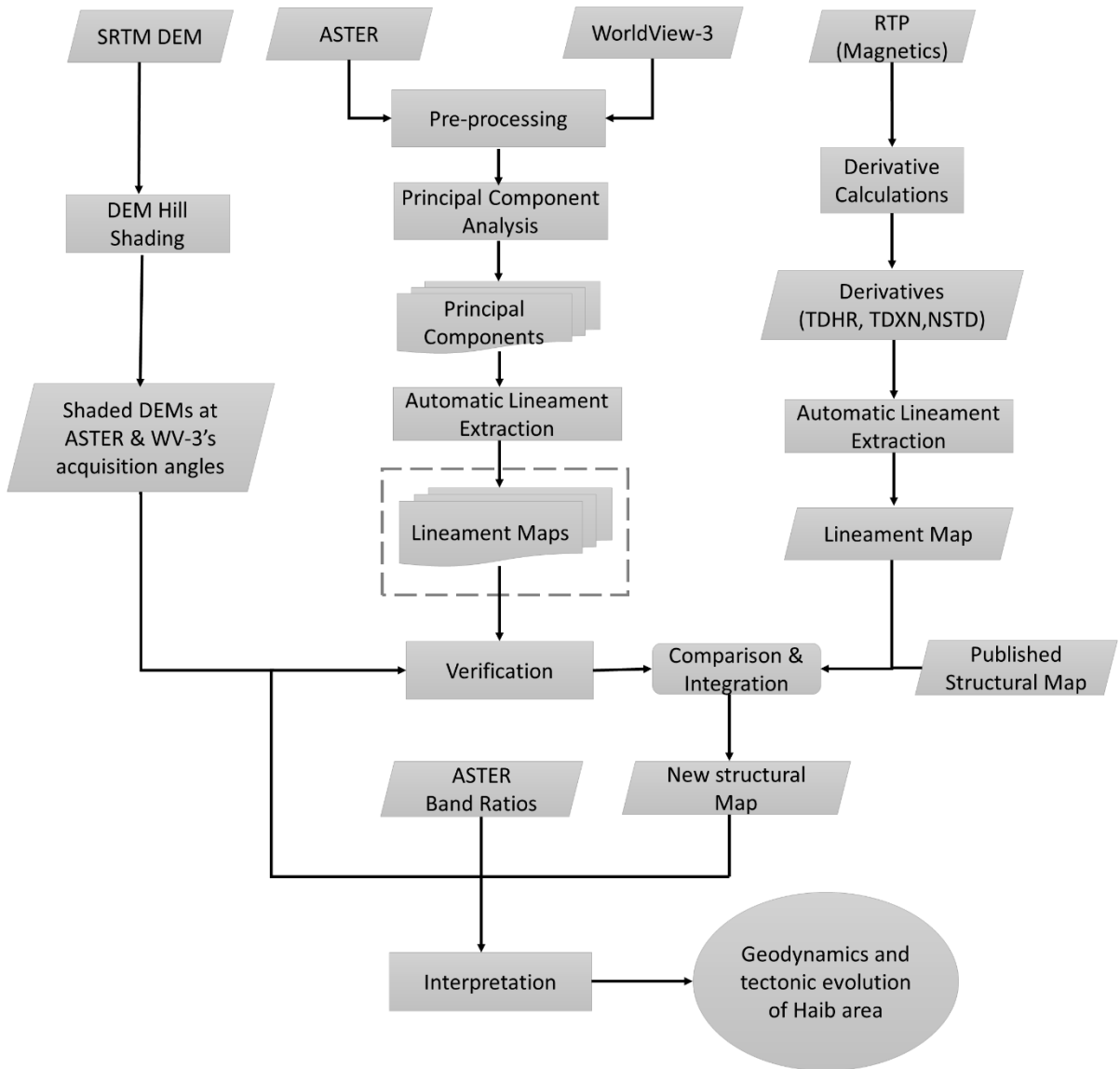


Figure 3-1: Summarised workflow of the research (Note: TDHR = Total horizontal derivative of the tilt angle, TDXN = Normalized total horizontal derivative and NSTD = Normalized standard derivative of the reduced to pole data)

3.2. Data pre-processing

Several pre-processing steps were performed on the ASTER and WorldView-3 data before the automatic lineament extraction was done. These pre-processing steps for each dataset are described below. In addition, the SRTM-DEM was also pre-processed prior to its use in lineaments verification and interpretation.

3.2.1. ASTER

The two multispectral Level 2 surface reflectance VNIR ASTER scenes and the other two crosstalk corrected SWIR ASTER scenes were mosaicked separately and then layer stacked and resampled to 15m VNIR spatial resolution using the Nearest neighbour algorithm. The layer stacked 9 bands surface reflectance of ASTER VNIR-SWIR image (Figure 3-2c), was subset to the Haib study area extent. A Normalized Difference Vegetation Index (NDVI) (Chao et al, 2011) was calculated using ASTER Bands 2 and 3 as Red and NIR bands respectively (Figure 3-2d). Based on the interactive adjustment of the linear stretch values and visual inspection of the image and spectral profile, a threshold level value of 0 – 0.4 was determined. And it revealed that there was no green vegetation highlighted in the image. Therefore, there was no need for vegetation masking on the ASTER images. All the ASTER images were cloudless making them ideal for this research work.

3.2.2. WorldView-3

The WorldView-3 data comprised of two scenes of multispectral VNIR (radiance-at-sensor). The two scenes were atmospherically corrected separately using Fast Line-of-sight Atmospheric Analysis of Hypercubes (FLAASH) algorithm (Kruse, 2014) in ENVI 5.3, converting radiance at sensor data into surface reflectance data ranging between 0 – 1. These two surface reflectance images were mosaicked and subset to the same study area's spatial extent as the ASTER data (Figure 3-2a). For a consistent comparison of the lineaments delineated from ASTER and WorldView-3 optical datasets, the WorldView-3 data was resampled to 15m spatial resolution. Then, a Normalized Difference Vegetation Index (NDVI) (Chao et al, 2011) was calculated using bands 5 and 7 as Red and NIR respectively. Similar linear stretch threshold level determination process as in ASTER data was applied and the same threshold value of 0 - 0.4 was determined. The NDVI calculation highlighted patches of vegetated areas (Figure 3-2b) which were then masked out before further analysis to suppress its effect on lineament structural mapping.

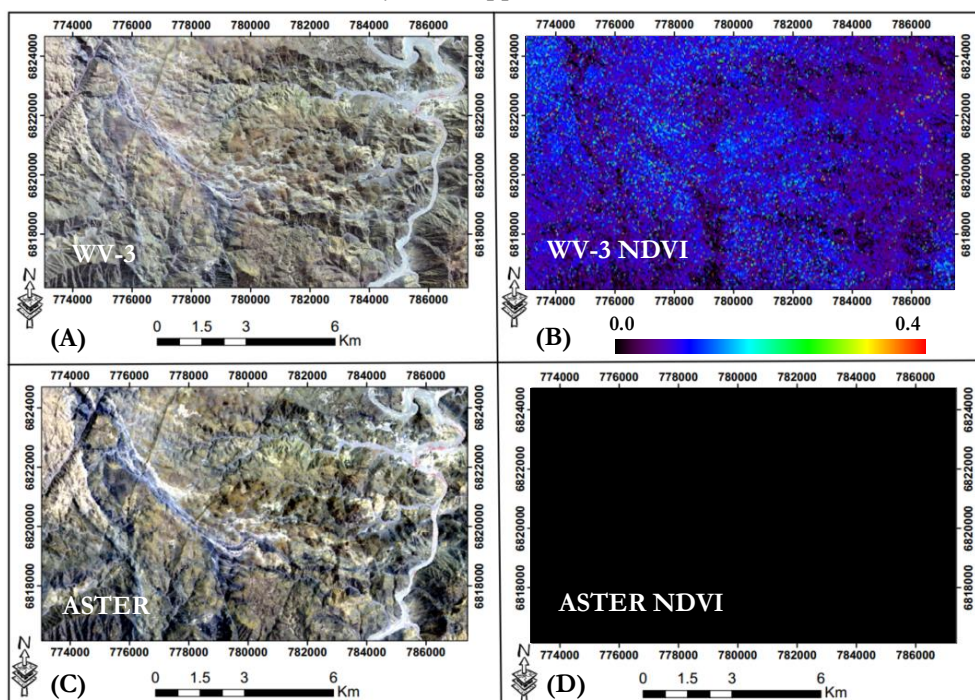


Figure 3-2: FCC (RGB = 753) WorldView-3 VNIR(a), NDVI result for WorldView-3 VNIR showing highlighted green vegetation(b), FCC (RGB = 321) ASTER(c) and NDVI result for ASTER image with no green vegetation highlighted(d)

3.2.3. Shuttle Radar Topography Mission (SRTM) Digital Elevation Model (DEM)

The Shuttle Radar Topography Mission (SRTM) Digital Elevation Model (DEM) was used in this research to verify the geological structural lineaments that were extracted using LINE module algorithm as implemented in the PCI Geomatica software (Hashim et al., 2013) from ASTER and WorldView-3 multispectral satellite data. Extraction of these lineaments from satellite images is mostly affected by the brightness levels of the satellite images (Liu et al., 2018). Hence, lineaments verification was significant in this research work. In addition to lineaments verification, the SRTM DEM was used in the lineaments' integration from all the datasets and also in the final tectonic interpretation.

Pre-processing the SRTM DEM involved construction of hill-shaded images in four different illumination directions 0° , 45° , 90° and 135° as developed by Muhammad & Awdal (2012), in order to enhance the geological structures that are related to topographic features in the study area (Figure 3-3). The blue arrows in each hill shaded DEM in the figure 3-3(a-d) represent the direction of the Sun Azimuth Angle and in all these images the Sun Elevation Angle of 45° was used. Furthermore, the hill-shaded DEMs at the ASTER's and WorldView-3's image solar illumination acquisition angles (azimuth: 81° , elevation: 67° and azimuth: 28° , elevation: 49° respectively; corresponding to WorldView-3 and ASTER's solar sun angles) were also constructed and overlaid by the automatically extracted lineaments for verification process (see Appendix I). The construction of these directional hill shaded DEM images was performed in ENVI 5.3 software and the images were saved in GeoTIFF format and exported to ArcGIS 10.5.1 for further processing. The combined multidirectional hill shaded DEM image from the different illumination directions (0° , 45° , 90° and 135°) shown in Figure 3-3(e) was produced in ArcGIS 10.5.1 using the overlay technique to ensure that all structures from each hill shaded image illumination direction are visible. The overlay technique in ArcGIS 10.5.1 applies a weighted sum of the raster input images to produce a single output image that is representative of all illumination directions of the input images (Chaabouni et al., 2012; Mdala, 2015). During this process, all the four directional hill-shaded DEM images (Figure 3-3(a-d)) were given equal weights.

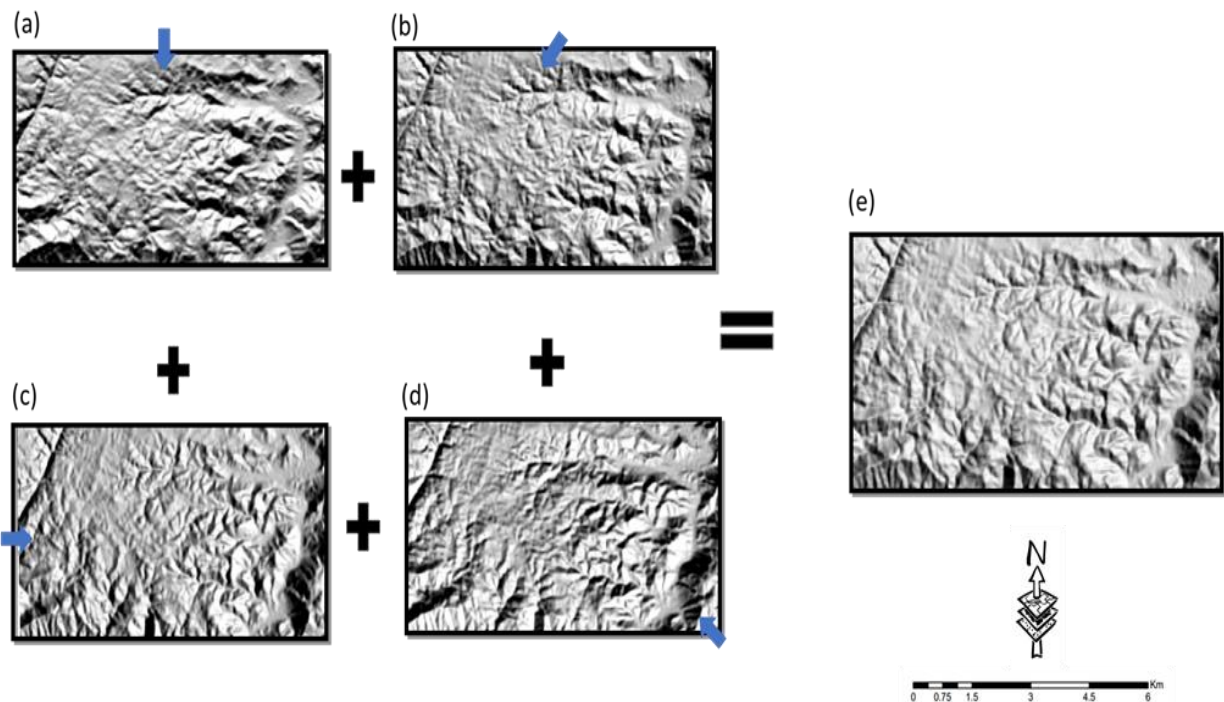


Figure 3-3: Hill shaded SRTM DEM images at different illumination directions (0° , 45° , 90° and 135°) a, b, c and d respectively represented by blue arrows. The weighted summed multidirectional hill-shaded image is shown in (e).

3.2.4. Aeromagnetic data

The aeromagnetic data was provided as an already pre-processed total magnetic intensity, gridded to a spatial resolution of 50 meters and corrected for International Geomagnetic Reference Field (IGRF) of the study area by the Geological Survey of Namibia. The total magnetic intensity was processed into reduced to the pole grid, which is the positioning of the magnetic anomalies in the data directly above their causative sources (Figure 2-5b in section 2.5).

3.3. Geological lineament structural mapping

Lineaments mapping certainly plays an important role in geological studies that attempt to understand tectonic crustal development of an area (Thomas & Cornell, 1994; Eglington, 2006; Marghany & Hashim, 2010). Lineaments are manifestations of deeper geological structures on the earth surface, reflecting important tectonic units in the crust and zones of favourable conditions for mineral formation, controlling of groundwater, geological disasters, geothermal resources and geomorphology (Adiri et al., 2017). Hence, in-depth lineament analysis studies are of theoretical and practical significance.

This section outlines the detailed methodology undertaken in this research in extracting geological lineament structures from ASTER, WorldView-3 and aeromagnetic data using automatic approaches. Firstly, lineament structures were extracted from principal component images (PCs) of ASTER and WorldView-3 multispectral satellite data based on Adiri et al., (2017). This was followed by lineaments analysis of how comparable the ASTER and WorldView-3 datasets extracted the lineaments in terms of their trending patterns, orientations, length and frequency analysis. Secondly, a full suite of three derivative-based magnetic enhanced images: Total horizontal derivative of the tilt angle (TDHR), Normalised total horizontal derivative (TDXN) and the Normalised standard derivative of reduced to pole magnetic data (NSTD) were calculated. These derivatives were then collocated into one edge detector from which lineaments were automatically extracted (Niccoli, 2015). Thirdly, lineaments extracted from ASTER and WorldView-3 satellite data were compared with the ones extracted from the collocated magnetic image, though bearing in mind that magnetic data also extracts subsurface structures. The aim of this comparison was to analyze how optical data (ASTER and WorldView-3) derived surface lineaments represent the subsurface delineated lineaments from magnetic data. Finally, the lineaments extracted from all the dataset were integrated to produce an up-to-date structural map of the area for tectonic interpretation to improve the understanding of the tectonic evolution and geodynamics of the study area.

3.4. Principal component analysis

The Principal Component Analysis (PCA) was performed on both ASTER and WorldView-3 multispectral images as an image enhancement technique in order to highlight the lineament structural information (Adiri et al., 2017). According to Li (2010), the principal component analysis is more efficient in the identification of lineaments as compared to other image enhancement techniques such as band ratios, histogram equalization, and high pass filters. Several studies have been based on the principal component analysis in the detection of lineaments from satellite data. For instances, Paganelli et al., (2003) used principal component bands in mapping lineaments on OLI and ASTER images in the Buffalo Head Hills area, northern central Alberta, Canada. Satellite images have been widely used in geological applications for extraction of lineaments and faults (Csillag & Stogicza, 1987; Li, 2010; Chaabouni et al., 2012; Yeomans et al., 2018; Zhumabek et al., 2017). Lineaments show up as lines or linear structures that are significantly brighter or darker than the background pixels in any greyscale remote sensing image. They provide a variety of spectral reflection of different features on the earth's surface, making it possible to determine, define and produce valuable information regarding the geological structural phenomenon (Meshkani et al., 2013).

Principal component analysis is a statistical technique widely used in extracting geological lineament structures (Adiri et al, 2016). It compresses information present in the reflectance image bands into new bands that are orthogonal to one another called Principal Components (PCs). This transformation technique eliminates the data redundancy, isolates the noise in the latest principal component and then enhances the target information in the input image, which is lineament structures in this case (Adiri et al., 2017). The technique transforms several correlated spectral bands into uncorrelated bands. A standard principal component analysis was performed in this research on the layer stacked VNIR-SWIR ASTER and WorldView-3 VNIR multispectral satellite image data from which the lineaments were extracted. According to Liu et al. (2018), the first three principal components contain 99% of the information including structural data and any of them can be used for lineament mapping. The first three components from ASTER and WorldView-3 data were inspected visually to check which principal component among them display clear structural information. Based on Liu et al. (2018), each of the first three principal components from each dataset were visually compared with the faults on the published geological map of the area (Blignault, 1972) in Figure 2-4.

3.5. ASTER and WorldView-3 data automatic lineaments structural mapping

Lineament extraction can be done using two approaches: automatic and manual lineaments extraction techniques as defined by Hung et al., (2005). Both approaches are useful depending on the circumstances as stipulated in Table 3-1 below. The automatic lineament approach uses computer-aided techniques that are based on edge filtering methods. It is very quick; however, non-geological lineaments (e.g. vegetated area boundaries) are often extracted as well. Hence, filtering such lineaments is necessary. The manual lineament extraction approach, on the other hand, the user manually visualizes and digitizes the lineaments after applying image enhancement techniques. This process is very tedious and depends on the user's experience, but it has the advantage that the user can detect and separate non-geological lineaments such as roads, fences, and drainage from geological lineaments. In this research, an automatic lineament extraction algorithm known as the LINE module of the PCI Geomatica 2018 software was implemented on ASTER PC2 and WorldView-3 PC1. The choice of using these principal components is explained in chapter 4, section 4.1. As a way of verifying and increasing confidence of the extracted lineaments, the lineaments were overlaid on multidirectional hill shaded DEM with different illumination angles with enhanced structures in all directions (Figure 3-3e) At the same time, the ASTER extracted lineaments were overlaid on the hill-shaded DEM at the ASTER's solar illumination acquisition angle and the WorldView-3 extracted lineaments were overlaid on the WorldView-3's solar illumination acquisition angle to visually check and increase confidence that extracted lineaments were true geological lineaments. (Appendix I shows the ASTER and WorldView-3 lineaments overlaid on the DEM illuminated images).

Automatic Lineament Extraction	Manual Lineament Extraction
- Depends only on the quality of the image	- Depends on the quality of the performance of the image (on screen and/or paper)
- Totally depends on the complexity of the research area	- Partly depends on the complexity of the research area
- Rapid	- Time consuming
- Little effect from human subjectiveness	- Strong effect on human subjectiveness
- Cannot recognise the origin of lineament, so the result may be confused	- Easy to distinguish the origin of lineament (tectonic setting, manmade, etc.)
- Totally depends on the mathematical function software and input assumptions	- Strongly depends on the human experience and ability
- Complex but an objective approach	- Simple but subjective approach

Table 3-1: Differences between Automatic and Manual lineament extraction approaches after Hung et al., (2005))

3.5.1. LINE Module lineament extraction algorithm

The LINE module algorithm as implemented in the PCI Geomatica software was used to detect and extract lineaments from ASTER-PC2 and WorldView-3-PC1 8bit images. According to Hashim et al, (2013), the LINE module delineates lineaments from the input 8bit grey scale image in three main stages. These stages include Edge detection, Thresholding, and Curve extraction as illustrated in figure 3-5 below.



Figure 3-4: Execution flowchart for the LINE Module algorithm automatic lineaments extraction

3.5.1.1. Edge Detection

Edge detection is the first stage in the LINE module lineaments extraction which involves the use of the Canny edge detection algorithm (Green, 2002) to produce an edge strength image from the input 8bit image. The Canny edge detector filters the image to suppress noise using the Gaussian function whose radius is defined by the parameter called Filter Radius (RADI). Then the gradient is computed from the filtered image and highlights regions with a high gradient. The RADI defines the radius of edge detection in pixels and determines the size of the Gaussian filter which shall be used as a kernel during edge detection (Nugroho & Tjahjaningsih, 2016). The RADI parameter range can be set with a range of 0 – 8192.

The Canny method is the first derivative edge detector that highlights image edges. According to Mdala (2015), the LINE module uses the Canny edge detector because it has the ability of high probability of detecting edges, good localization of edges on an image and having one response to a single edge. These characteristics enable the Canny edge detector to smooth the image and suppress noise, find gradients on the image and then highlights such regions with high spatial derivatives (Green, 2002). After highlighting these regions, the Canny edge detector tracks these areas and if it finds any pixels that are not reaching the maximum value, it suppresses them and the remaining non-suppressed pixels are tracked along in the process called hysteresis. (Green, 2002). This process uses two thresholds to determine the edge pixels on an input image. The input image pixels are tested for and any pixels lower than the first threshold are turned into masks and assigned zeros (non-edge pixels) with the remaining ones assigned as edges (Green, 2002). Finally, the LINE module algorithm later inputs these as line segments for further automatic extraction.

3.5.1.2. Thresholding

In the second stage of the LINE module, the edge strength image produced in the first stage is thresholded to obtain a binary image. The value of the threshold is defined by the Edge Gradient Threshold (GTHR) parameter and it defines the threshold for the minimum level of the gradient for the edge pixel to get the binary image. The GTHR value can range from 0 – 255 (Adiri et al., 2017).

3.5.1.3. Curve extraction

The last stage in the LINE module is the curve extraction which involves extraction of curves from the binary image. According to Nugroho & Tjahjaningsih (2016), this stage is made up of three sub-steps which are; the application of a thinning algorithm to the binary edge image to obtain pixel-wide curves. Then, a sequence of pixels for each curve is extracted depending on the Curve Length Threshold (LTHR) parameter. The LTHR specifies the minimum length of a curve in the pixel distance, to be considered as valid lineaments and it ranges from 0 to 8192. Finally, the extracted pixel curve is converted to vector form by fitting a line segment to it.

The resulting polyline is then an approximation of the original pixel curve, whose maximum fitting error is specified by the Line Fitting Threshold (FTHR) parameter which ranges from 0 to 8192. Further to these parameters, the algorithm considers two more parameters; the Angular Distance Threshold (ATHR) parameter which defines an angle in degrees (0 to 90) between which lineaments can be connected as one single segment; and the last parameter, the Linking Distance Threshold (DTHR) which defines the distance in pixels(0 to 8192) between the two vectors for them to be connected (Adiri et al., 2016).

3.5.2. Optimal parameters for ASTER and WorldView-3 automatic lineaments extraction

The optimal parameters for the lineament extraction on the ASTER and WorldView-3 satellite images were chosen based on two different approaches. The first approach was the knowledge-based approach. In this approach, the known lineaments from the published geological map of the study area were used as a reference for the extraction process. The parameter values were then adjusted until the extracted lineaments matched the reference lineaments (field-based faults). Based on this, the rest of the extracted lineaments were considered for further processing. The data-driven approach was the second approach used. In this process, the parameters were adjusted based on the sensitivity of data’s spatial resolutions in order to extract reasonable lineaments. As such, the same optimal parameters for ASTER and WorldView-3 were generated. In this study, the following parameters: Filter Radius (RADI), Edge Gradient Threshold (GTHR), Curve Length Threshold (LTHR), Line Fitting Threshold (FTHR), Angular Distance Threshold (ATHR) and Linking Distance Threshold (DTHR) for ASTER and WorldView-3 data are indicated in Table 3-2 below. The automatic lineaments extracted from ASTER and WorldView-3 matching the published faults are shown in Appendix II.

Parameter	Description	Value used-ASTER@15m	Value used-WV3@15m
RADI	Filter Radius	15	15
GTHR	Edge Gradient Threshold	75	75
LTHR	Curve Length Threshold	40	40
FTHR	Line Fitting Threshold	3	3
ATHR	Angular Difference Threshold	15	15
DTHR	Linking Distance Threshold	45	45

Table 3-2: Optimal parameters for the automatic lineament extraction for ASTER and WorldView-3 data

3.6. ASTER and WorldView-3 data automatic lineaments comparison and analysis

The lineaments extracted from ASTER and WorldView-3 were compared before integrating them into one structural map. To achieve the comparison, the lineament analysis from the datasets was done using two approaches: a visual and geospatial analysis. The visual comparison analysis involved the production of lineament maps automatically extracted from the datasets to observe their spatial distribution and structural pattern. The geospatial approach involved comparing the lineaments in terms of orientation pattern, length, and frequency.

3.6.1. Lineament pattern and spatial distribution analysis

The comparison of the spatial distribution of the extracted lineaments from ASTER and WorldView-3 was done by producing lineament maps from each dataset in ArcGIS Desktop 10.5 to observe their spatial consistency. The lineaments were analyzed based on the pattern of the lineaments in both datasets, spatial extent of the mapped lineaments and prominent directions that is visually observable on the lineament maps. The analysis also focused on areas where the datasets extracted similar lineament patterns, and where there were significantly noticeable differences in the lineament maps.

3.6.2. Orientation pattern analysis

The orientation pattern comparison of the extracted lineaments was done by plotting length-based Rose diagrams of the ASTER and WorldView-3 extracted lineaments separately. The lineaments were exported as AutoCAD vectors in a data interchange 2013 (DXF) file format in ArcGIS Desktop 10.5 and imported into Rockworks software version 17. In the Rockworks 17 software (www.rockware.com), the bearing of the extracted lineaments was calculated using the lineaments properties technique. The lineaments were plotted based on the length option known as 'the length as a percent of the total lineation length'. Thus, the petal radii and annotation of the Rose diagram were based on length.

3.6.3. Length and frequency analysis

The lineaments length from both datasets were analyzed and compared to observe the length variations and their corresponding frequencies. This information is arguably important since it provides confidence as to which dataset between ASTER and WorldView-3 is reliable in extracting the geological lineaments considering the differences in their spectral specifications. The lineament lengths were calculated in ArcGIS Desktop 10.5 using the calculate geometry option and the frequency histograms were produced in IBM SPSS software (<https://www.ibm.com/analytics/spss-statistics-software>).

3.7. Aeromagnetic data automatic lineaments structural mapping

This section explains the methodology applied to automatically delineate lineament structures from the magnetic derivative data. The lineaments were extracted from the collocation of three magnetic derivatives described below whose input was reduced to pole magnetic data shown in Figure 2-5(b).

3.7.1. Derivatives

Derivatives of potential field data, for example, magnetic data are useful in delineating edges of lineaments/faults and contact boundaries since they enhance the lateral and horizontal variations of magnetic signals (Cooper & Cowan, 2006; Ma & Li, 2012; Akinlalu et al., 2018). The derivatives have an effect of sharpening anomalies caused by abrupt variation in the near-surface bodies or more gradual signal (Chisenga et al., 2018). According to Ranganai & Ebinger (2008), derivatives enhances short wavelength components caused by deep-seated features, thus allowing for more accurate detection of lineaments/faults and contact edges.

Several individual potential field data such as vertical and horizontal derivatives have often been used in lineaments mapping, but they have a disadvantage of not displaying the large and small amplitude edges simultaneously (Ma & Li, 2012). Pilkington & Keating (2004), proposed that to increase confidence in lineaments mapping, and to produce reliable results, collocation edge detection approach may be used instead of individual derivatives. As such, in this research, three magnetic data derivatives: Total horizontal derivative of the tilt angle (TDHR), Normalized total horizontal derivative map (TDXN) and Normalized standard deviation of the reduce to pole data (NSTD) were used to delineate lineaments/faults/contacts using an automatic python implemented algorithm by Niccoli (2015). The lineaments that were identified at the same spatial location of at least two or three of these edge detectors were mapped as true lineaments.

3.7.1.1. Total horizontal derivative of the tilt angle (TDHR)

Verduzco et al, (2004), proposed the TDHR as an enhanced filter computed as the square root of the sum of square derivatives of the tilt angle in the x and y directions. The tilt angle is used as an input in the calculation of this detector. Basically, the tilt angle as presented by Miller & Singh (1994), is an amplitude normalized vertical derivative that uses both vertical and horizontal derivatives. As such, it enhances both shallow and deep-seated lineaments/contacts.

Even though the tilt angle is a robust edge detector, it requires further enhancement in the horizontal direction to reduce blurring of deep-seated sources (Cooper & Cowan, 2006). The total horizontal derivative of tilt angle is given by:

$$TDHR = \sqrt{\left(\frac{\partial TDR}{\partial x}\right)^2 + \left(\frac{\partial TDR}{\partial y}\right)^2}, \quad (1)$$

where

$$TDR = \tan^{-1}\left(\frac{TZ}{THDR}\right) \quad (2)$$

and TZ is the vertical derivative and THDR is the total horizontal derivative of the reduced to pole data.

3.7.1.2. Normalized total horizontal derivative (TDXN)

Another derivative used in this research to delineate lineaments was the normalized total horizontal derivative (Ma & Li, 2012). It is a ratio of the horizontal derivative to maxima of the nearby horizontal derivatives. This derivative does not require the calculation of its vertical derivative, thereby making it more computationally stable. The maxima of the TDXN are located on the edge of the causative sources (Ma & Li, 2012). The TDXN is expressed as:

$$TDXN = \frac{TDX(i, j)}{\max[TDX(i - m: i + m, j - n: j + m)]} \quad (3)$$

Where $TDXN(i, j)$ represents the output value of (i, j) and;

$$TDX = \sqrt{\left(\frac{\partial f}{\partial x}\right)^2 + \left(\frac{\partial f}{\partial y}\right)^2} \quad (4)$$

represents the total horizontal derivatives; m, n is the size of the window (i.e. sample size)

3.7.1.3. Normalized standard deviation (NSTD)

The final derivative used to extract lineaments from magnetic data was the normalized standard deviation as introduced by Cooper & Cowan (2008). This filter is based on the normalized statistics of the input data, which is reduced to pole data in this case. The standard deviation measures the local variability of the input data in relation to its background. Areas with lineaments/faults or contacts have high variability than the rest and are then highlighted. This result in enhancing both large and small amplitude edges simultaneously (Cooper & Cowan, 2008). The normalized standard deviation is represented by:

$$NSTD = \frac{\sigma\left(\frac{\partial f}{\partial z}\right)}{\sigma\left(\frac{\partial f}{\partial x}\right) + \sigma\left(\frac{\partial f}{\partial y}\right) + \sigma\left(\frac{\partial f}{\partial z}\right)} \quad (5)$$

After calculating the above derivatives, they were collocated together, and the lineaments/faults were then automatically delineated using the python implemented algorithm modified after Niccoli (2015).

3.8. Analysis and Interpretation of ASTER and WorldView-3 automatic extracted lineaments

For a tectonic interpretation of an area, the main lineament structures such as faults and dykes are important. Therefore, analysis and interpretation were performed on the automatically extracted lineaments from ASTER and WorldView-3 in order to filter the non-geological lineament structures in the Haib area. This interpretation is called inferred because no field verification was done on these main linear structures. Therefore, that poses as a limitation in the full interpretation of these structures. The following criteria were used and the corresponding maps for each step are shown in appendix III.

- **Corresponding lineaments with faults on the pre-existing geological map** – If the lineament best matched with the published faults on the geological map by Blignault (1972), it was considered a fault for interpretation. Lineaments from ASTER and WorldView-3 were overlaid together with the published faults and the matching lineaments were interpreted as true faults.
- **Evidence of lineaments displacements** – The automatically extracted lineaments from ASTER and WorldView-3 data that showed displacements indicated evidence of faulting in the area were interpreted as true lineaments and were considered.
- **Collocated lineaments with the magnetic delineated lineaments** – The lineaments from ASTER and WorldView-3 data were compared with magnetic extracted lineaments which are not affected by surface distortions. The magnetic lineaments were used as a benchmark. As such, the lineaments that matched the magnetic data were considered true lineaments and interpreted as so. All lineaments that passed through the top of the magnetic anomalies were removed from the interpretation.
- **Consistent lineament pattern** – The ASTER and WorldView-3 lineament patterns were analyzed and the lineaments that showed similar consistent patterns were considered for interpretation than the random-oriented lineaments.

3.9. Lineaments kinematics and sense of motion of ASTER, WorldView-3 and Magnetic data

All lineaments delineated from ASTER, WorldView-3 and Magnetic data were compared in terms of their kinematics and sense of motion. The lineaments kinematics and sense of motions were derived from each dataset mainly based on the kinematic indicator of displaced lineament features. Furthermore, the orientation angles from the Rose diagram of each dataset was used in the kinematic implication diagrams. And then the lineaments kinematics and sense of motion were used to identify the relative lineament/fault chronology based on cross-cutting relationships of the offset lineaments from each dataset.

3.10. Lineaments integration from ASTER, WorldView-3 and magnetic data

The lineaments detected in this research from ASTER, WorldView-3 and Magnetic data were integrated to create a composite and reliable lineament structural network map of the study area. It is suggested that, based on the abilities of the data used in this research, the optical remote sensing data (ASTER and WorldView-3) and aeromagnetic data provided different contributions towards lineaments mapping. In view of this, combining lineaments and structural information from these datasets provided a plausible set of geological lineament structures for tectonic and geodynamic interpretation of the study area.

This section outlines the criteria used in this research to integrate the lineaments mapped from ASTER, WorldView-3, and aeromagnetic data. The integration steps applied were developed by Yeomans et al, (2018) in integrating Object-Based Image Analysis for semi-automated geological lineaments detection in Southwest England using airborne geophysical data and LiDAR data, but have been modified to suit the datasets used in this research.

The following three steps were used for lineaments integration:

- **Collocation of lineaments from at least two or all datasets:** This step considered where the maxima/delineated lineament that existed on the same spatial location from at least two of the datasets. In other words, the collocation step maps a lineament at a location where lineaments from two or all the datasets were mapped within the same proximity (a closer distance of one lineament to another). A choice between any of the lineaments was taken and the lineament was maintained at the same spatial location.
- **Lineaments correlation with topographical expressions:** This step involved comparing the extracted lineaments from all the datasets with the geomorphological manifestations of the SRTM-DEM multidirectional hill shade (Appendix VI) and the shaded SRTM-DEMs based on the optical data solar illumination acquisition angles (Appendix VII). The lineament set that correlated with this topographical expression was considered for integration.
- **Maxima/delineated lineament connectivity:** The last step considered the lineament set that is continuous and well connected as a linear structure. The intermittent lineament sets were not included in the integration.

During this integration process, if a magnetic lineament satisfied the above criteria, it was considered for integration. This choice was made because of the two likely reasons: Firstly, the magnetic data is not affected by misidentification of other linear features like roads, fences, and drainage as it is the case with optical data. Secondly, the lineaments derived from magnetic data delineate structures at a depth in the crust as opposed to the optical data (Chisenga et al., 2018; Cooper & Cowan, 2008; Ma & Li, 2012; Niccoli, 2015).

3.11. ASTER band ratios

The ASTER band ratios (knowledge-based approach) using absorption feature modeling (Asadzadeh, Roberto, & Filho, 2016) were performed to help validate the interpretation of the final integrated structural lineaments. The ASTER data was chosen and used in the band rationing because it was a layer stacked VNIR-SWIR data ranging from 0.5560-2.400 micrometers covering the study area. But the combined WorldView-3 VNIR-SWIR data had a gap between the two images scenes (as was provided by DigitalGlobe Foundation) and did not cover the whole study area completely. Thus, the ASTER VNIR-SWIR data was the most logical choice for band rationing in this case. The band ratios are based on discrete characteristics of the absorption features of the minerals present (Mustard & Sunshine, 1999; van der Meer, 2004). This approach is commonly used in mineral alteration mapping since it is not sensitive to illumination and topographical effects and suppresses the variations in the reflectance albedo (Cudahy, 2012; Langford, 2015).

Three band ratios of the mineral group contents based on Cudahy (2012) band ratio algorithms were used in this research to highlight the mineral occurrences. These mineral group content included the Al-OH, Mg-OH/Carbonate, and Ferric oxide mineral groups, which were chosen for the area based on the mineral alteration maps of the study area mapped by Teck Cominco Namibia Ltd (2009) and Adegboyega (2016) using Hyperspectral (HyMap) data.

The Cudahy (2012) band ratio algorithms were initially tested and developed for regional mapping for in Australia and the stretching thresholds were based on ASTER's performance over Australia. These same thresholds were applied in this research for the three ASTER algorithms shown in table 3-3 below. The individual mineral group contents were then combined in a Red/Green/Blue combination after applying the thresholds to produce the mineral content map of the area with Al-OH/Mg-OH-Carbonate and FeO respectively to aid the tectonic interpretation of the lineaments in the study area.

Mineral Group (Content)	Algorithm	Stretch Value		Enhancement style
		Min	Max	
Al-OH	$(B5+B7)/B6$	1.95	2.4	Linear
Mg-OH/Carbonate	$(B6+B9)/(B7+B8)$	1.01	1.200	Linear
FeO	$B4/B3$	1.1	2.1	Linear

Table 3-3: Cudahy (2012) defined algorithm for ASTER data for Al-OH, Mg-OH/Carbonate and FeO mineral content groups

4. RESULTS

4.1. Principal component analysis

The ASTER and WorldView-3 Principal Components (PCs) results were analyzed in order to make a choice of which principal component to use for each dataset in the automatic lineament extraction. Based on Liu et al (2018), the analysis of the first three components from each datasets in comparison with the field-based faults on the published geological map of the Haib area (Blignault, 1972) (Figure 2-4), showed that ASTER PC2's structures (Figure 4-1b) corresponded with the published faults than PC1 and PC3 whilst for WorldView-3 PC1's structures (Figure 4-1c) corresponded with the published faults than PC2 and PC3. The ASTER PC2 and WorldView-3 PC1 were clear and not blurry. Therefore, they were used to automatically extract the lineaments. Figure 4-1 below shows the principal component image results of ASTER PC1(a), ASTER PC2(b), WorldView-3 PC1(c) and WorldView-3 PC2(d). The PC3 images for both datasets were very blurry and unclear.

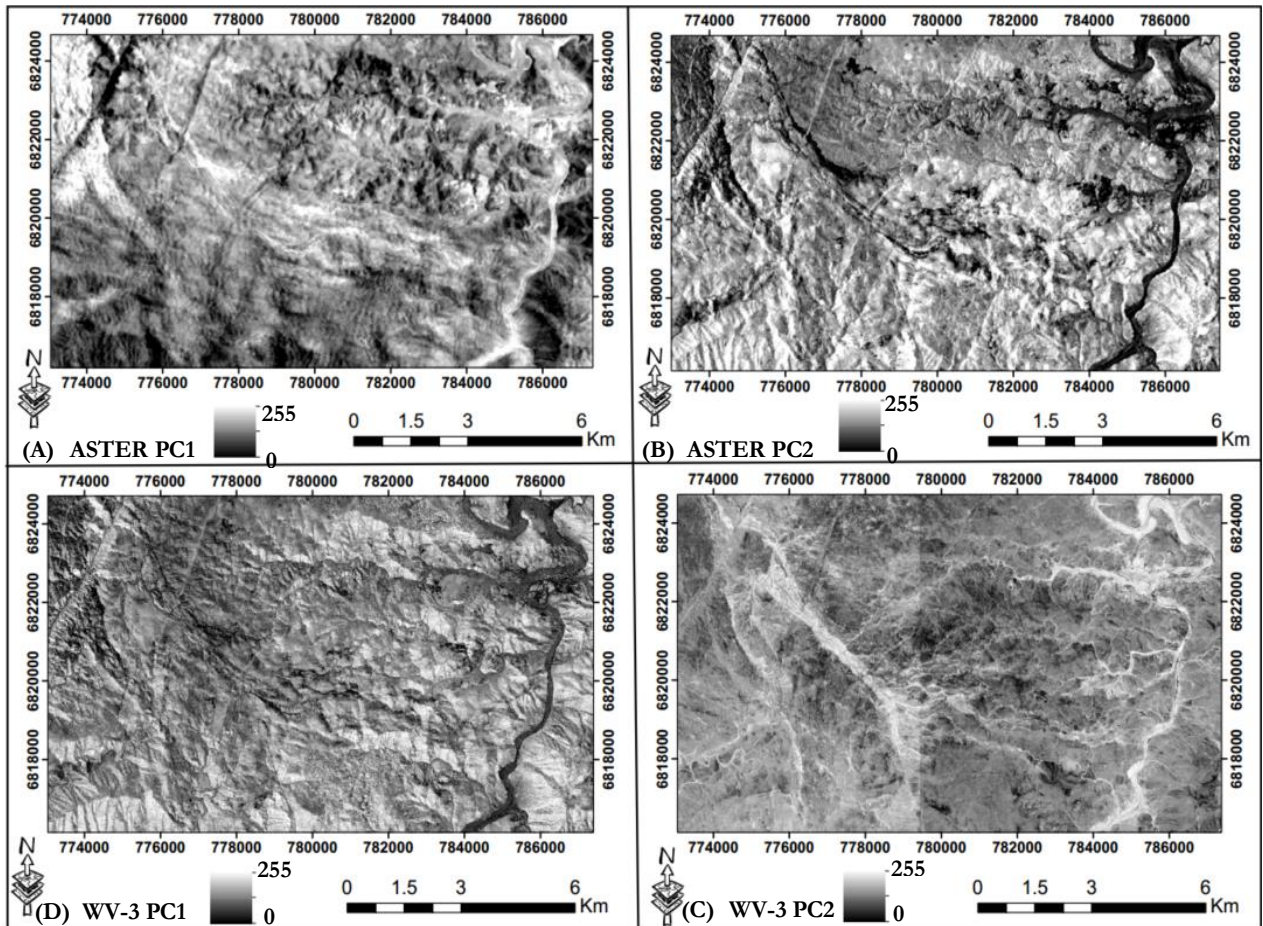


Figure 4-1: ASTER PC1, unclear and blurry(a), ASTER PC2, from where the lineaments were automatically extracted(b), World View-3 PC1, from where the lineaments were automatically extracted(c) and WorldView-3's PC2, unclear and blurry, with the middle line showing the effect of image mosaicking(d)

4.2. ASTER and WorldView-3 data automatic lineaments structural mapping

This section presents the results of the automatically extracted lineaments from ASTER and WorldView-3 principal component orthogonal bands, using the PCI Geomatica LINE Module algorithm. The input optimal parameters for the algorithm are shown in Table 3-2 in subsection 3.5.2. The lineaments are shown in Figures 4-2 and 4-3 below.

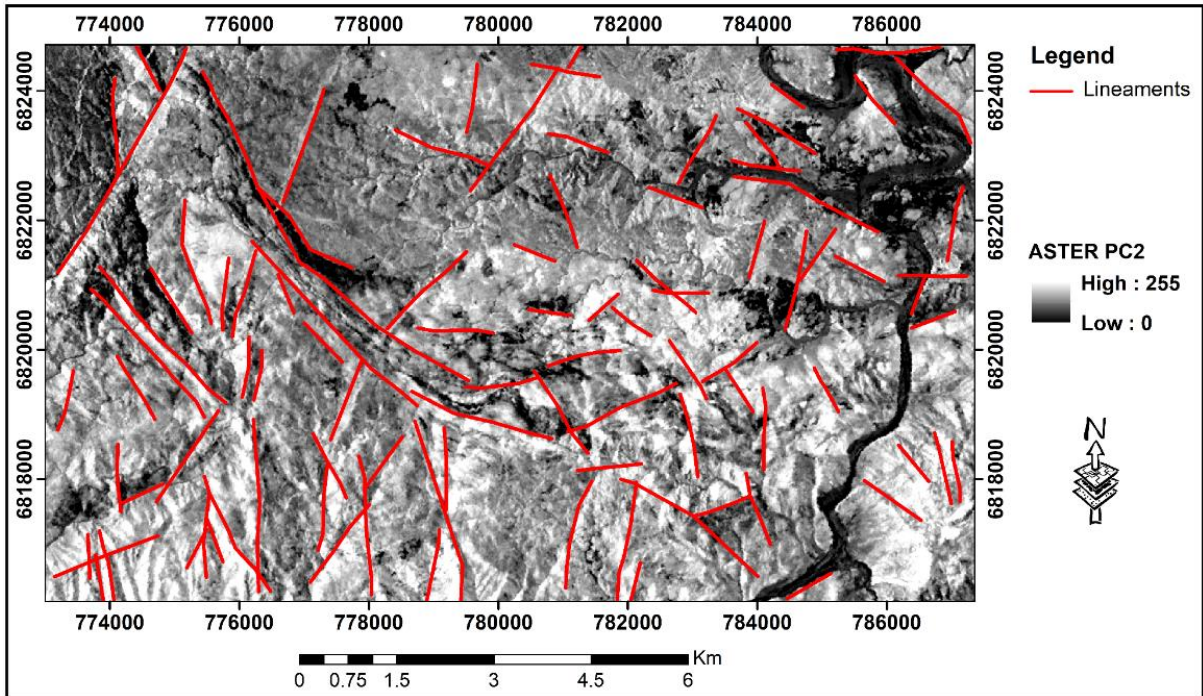


Figure 4-2: ASTER automatic extracted lineaments overlaid on ASTER PC 2 image

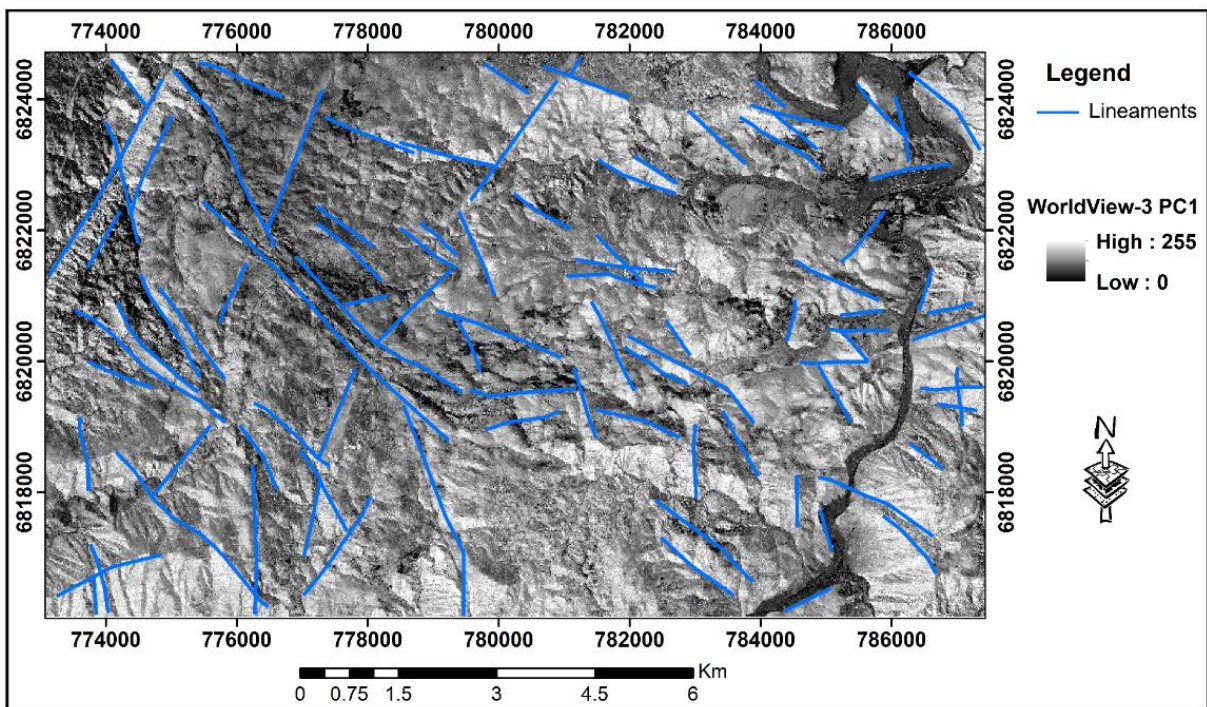


Figure 4-3: WorldView-3 automatic extracted lineaments overlaid on WorldView-3 PC 1 image

4.3. ASTER and WorldView-3 data automatic lineaments comparison and analysis

The results of the automatic lineaments structural mapping in the study area from ASTER and WorldView-3 datasets produced two lineament maps as shown in section 4.2 above. The datasets were compared on how they extracted the lineaments in the study area by analyzing their lineament pattern and spatial distribution, orientation pattern, length, and frequency distribution. The results of these analyses are shown in this section.

4.3.1. Lineaments pattern and spatial distribution analysis

The ASTER and WorldView-3 lineament maps show similar lineament pattern and distribution in most of the major lineaments in the area. For example, the published faults as shown in Appendix I (also shown by the yellow solid circles (just to highlight a few) in Figure 4-4), are similar in both lineaments' maps and the central lineaments showing a curve-like structure is present in both maps with a similar pattern and distribution. Most lineaments in both maps are concentrated on the western part of the area with a dominant pattern in the NW-SE direction which corresponds to the general regional structural trend in the Richtersveld Sub-province within the Namaqua-Natal Metamorphic Belt (Anhaeusser, 1990; Corner, 2000) and another trending pattern in the NE-SW direction. However, some differences are observed in these lineaments. For instance, the WorldView-3 data extracted more lineaments on the northwestern corner of the area compared to the ASTER data. And lineaments shown in green solid circles (just to highlight a few) are present on WorldView-3 but are not present in ASTER as shown in Figure 4-4. The spatial difference in meters of the lineaments extracted from ASTER and WorldView-3 data ranges between 70 to 100 meters. Despite the similar pattern, the datasets do not extract the lineaments consistently and not exactly on the same spatial location.

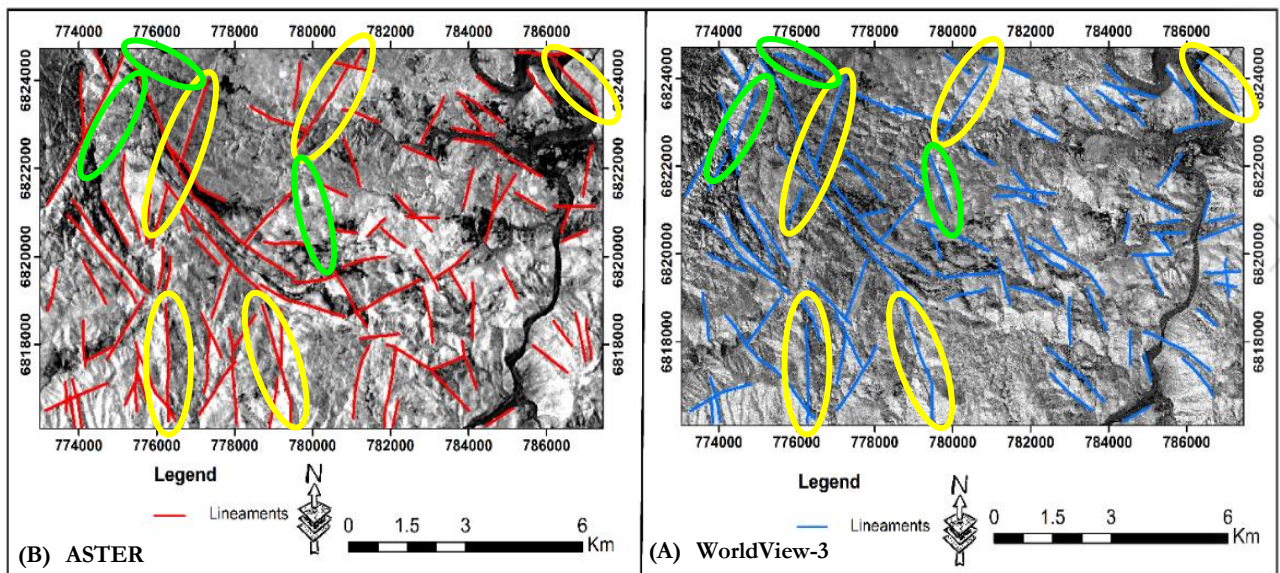


Figure 4-4: Lineament maps extracted from ASTER data overlaid on ASTER PC2 image(a) and WorldView-3 data overlaid on WorldView-3 PC1 (b) showing the distribution patterns of the extracted lineaments, with a few examples of similarly extracted lineaments in yellow solid circles and different lineaments in green dotted circles.

4.3.2. Orientation pattern analysis

The orientation pattern analysis comparison results from the length-based Rose diagrams of the automatically extracted lineaments from ASTER and WorldView-3 do not show the same perfect orientation patterns. However, the extracted lineaments show similar general dominant lineament orientation pattern in the NW-SE direction and another minor direction in the NE-SW direction, but at different angles in the datasets. The NE-SW direction is clearer in the WorldView-3 data (Figure 4-5b) compared to the ASTER data which is more to the NNE-SSW (Figure 4-5a). These differences may affect the individual dataset interpretation of the structural orientation in the area, though roughly the regional interpretation is the same. The ASTER NW-SE dominant orientation pattern is more pronounced at 330-340 degrees which is a different dominant angle in the WorldView-3 dataset which is more pronounced at 290-320 degrees. The observed second orientation pattern is also different in both datasets. The ASTER is more in the NNE-SSE between 0-50 degrees while WorldView-3 in the NE-SW between 20-35 degrees. However, the two general orientations patterns NW-SE and NE-SW imply that the area has been affected by two different tectonic forces that have resulted in these structural orientations. These tectonic forces correspond to structures formed by Orange River Orogeny (NW-SE tectonic force transport direction) and Namaqua Orogeny (NE-SW tectonic force transport direction) as also observed by Barr & Reid (1992). This is clear evidence of neotectonic events in the study area. One structural episode overprints the other in the area. The detailed geochronology of these events and the possible causes of the differences in the dominant orientation angles of the lineaments are discussed in chapter 5. Figure 4-5 shows the Rose diagrams from ASTER and WorldView-3 datasets.

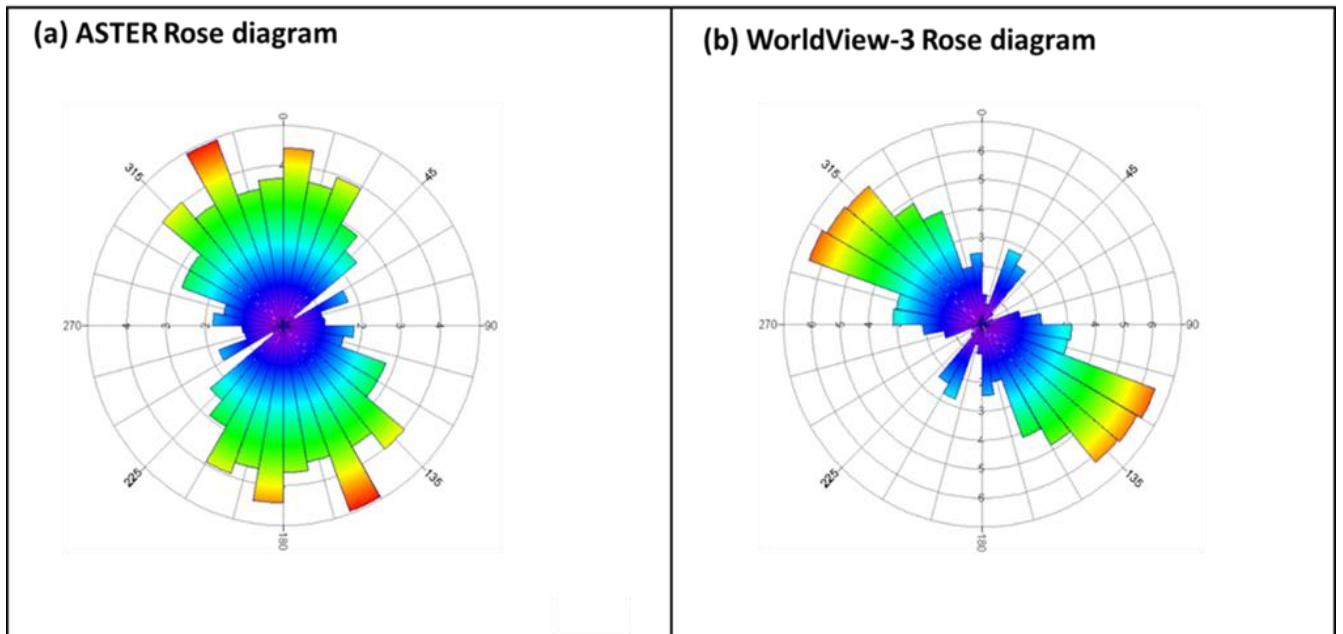


Figure 4-5: Rose diagrams extracted from ASTER data (a) and WorldView-3 data (b) Note the general orientations in the NW-SE dominant direction and the minor NE-SW direction, more pronounced in the ASTER in NNE-SSW direction

4.3.3. Length and frequency analysis

The length and frequency analysis comparison results of the lineaments from ASTER and WorldView-3 as shown by the histograms in Figure 4-6a (ASTER) and Figure 4-6b (WorldView-3) show similar right skewed frequency distribution pattern. Both ASTER and WorldView-3 multispectral data extracted more lineaments that are between 700-1000 meters in length.

The total length of all lineaments in both datasets were approximately 152 kilometers, however, WorldView-3 data compared to ASTER data extracted slightly more lineaments. In total, ASTER data extracted 128 lineaments, with the shortest and longest lineaments lengths of approximately 0.3 kilometers and 3.31 kilometers respectively. On the other hand, the WorldView-3 data extracted a total of 135 lineaments, with the shortest and longest lineaments of approximately 0.6 kilometers and 3.5 kilometers respectively. The length and frequency histogram of the extracted lineaments from ASTER and WorldView-3 data are shown in the figure 4-6 below.

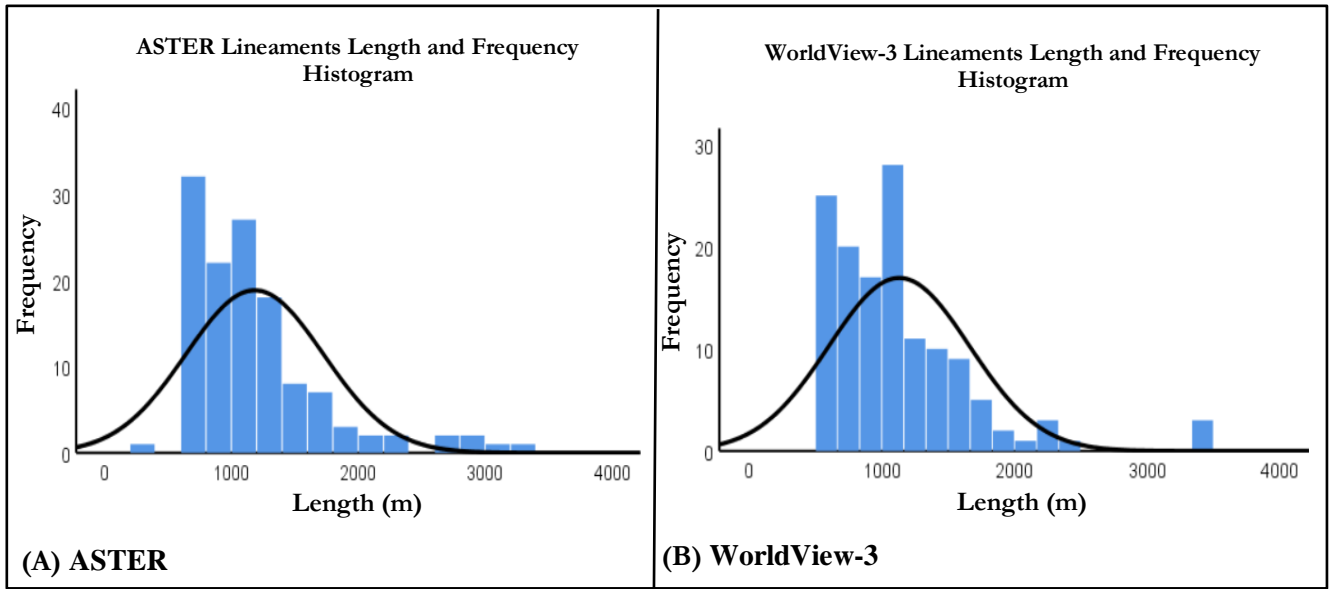


Figure 4-6: Lineaments length and frequency histograms extracted from ASTER (a) and WorldView-3 (b) datasets showing a similar right skewed frequency distribution

Based on the comparison and analysis of the lineaments extracted from ASTER and WorldVoiew-3 data, there are similarities in the NE-SW and NW-SE spatial distribution pattern and general orientation in the results obtained. On the other hand, the differences are significantly observed in the datasets, especially in the Rose diagrams' orientation angles, number and length of the extracted lineaments: ASTER extracted an average length of 1.18 km with minimum and maximum length of 0.3 km and 3.31km respectively and WorldView-3 extracted an average length of 1.13 km with minimum and maximum length of 0.6 km and 3.5 km respectively. This indicates that the datasets contained variations such as lineaments orientation angles and misidentification. Hence, the datasets did not extract the lineaments consistently. A discussion of the possible causes of this variation is presented in chapter 5.

4.4. Aeromagnetic data automatic lineaments structural mapping

This section presents results of the lineaments mapped from magnetic data. The lineaments structural mapping from magnetic data were automatically extracted from the collocation of three calculated derivatives: Normalised standard deviation (NSTD), Total horizontal derivative of the tilt angle (TDHR) and the Normalised horizontal derivative (TDXN) using a python implemented algorithm as discussed in section 3.7. The results of these calculated derivatives and the reduced to pole input data are shown in Figure 4-7 below. Collocation approach of these magnetic derivative images provides increased confidence and plausible set of mapped lineaments. This is because lineaments are automatically delineated as collocated solutions from all these enhanced filters, making this approach a robust technique in lineament mapping from potential field data (Pilkington & Keating, 2004). The extracted magnetic lineaments are shown in Figure 4-8. These lineaments represent both contacts of geological bodies and faults. The general trends of the delineated lineaments are NW-SE and NE-SW directions. These two trending patterns are similar to the patterns shown by the lineaments from ASTER, WorldView-3 datasets and the published geological map of the study area.

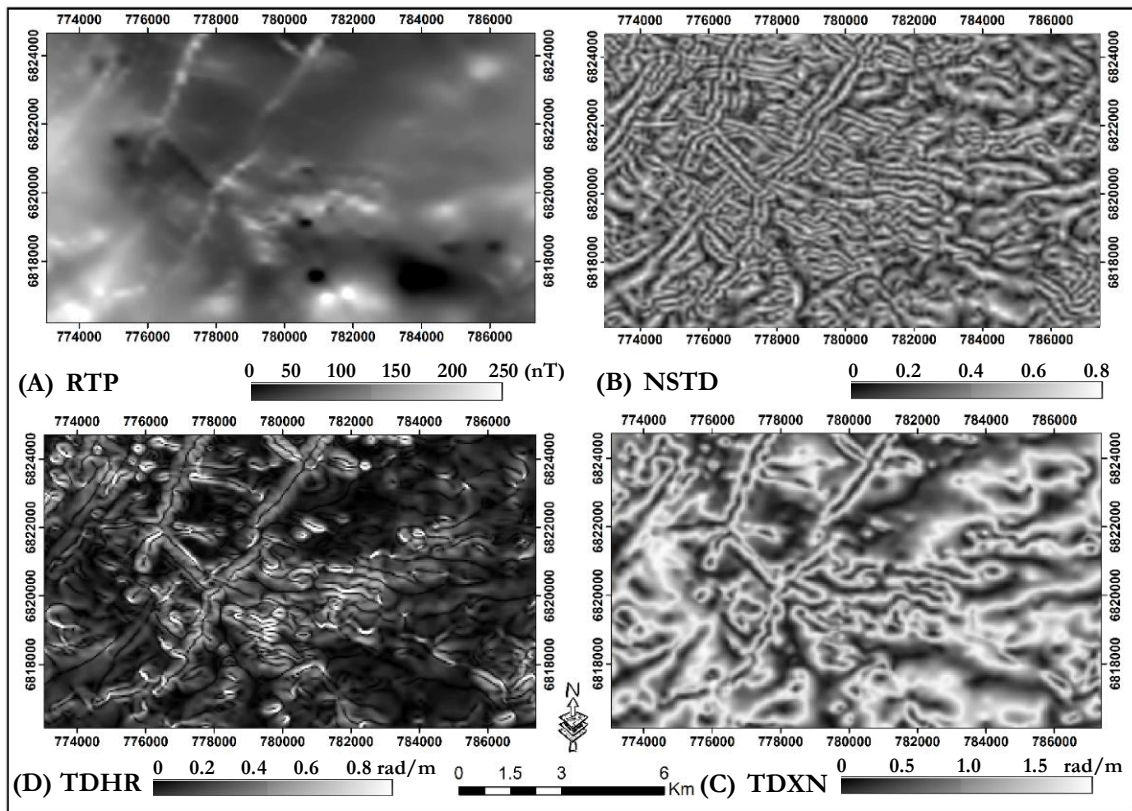


Figure 4-7: Reduced to pole magnetic input data (a), Normalised standard deviation (NSTD) derivative of the input data (b), Total horizontal derivative of the tilt angle (TDHR) (c) and the normalized horizontal derivative (TDXN) (d). These derivatives (b, c, and d) were collocated to delineate lineaments

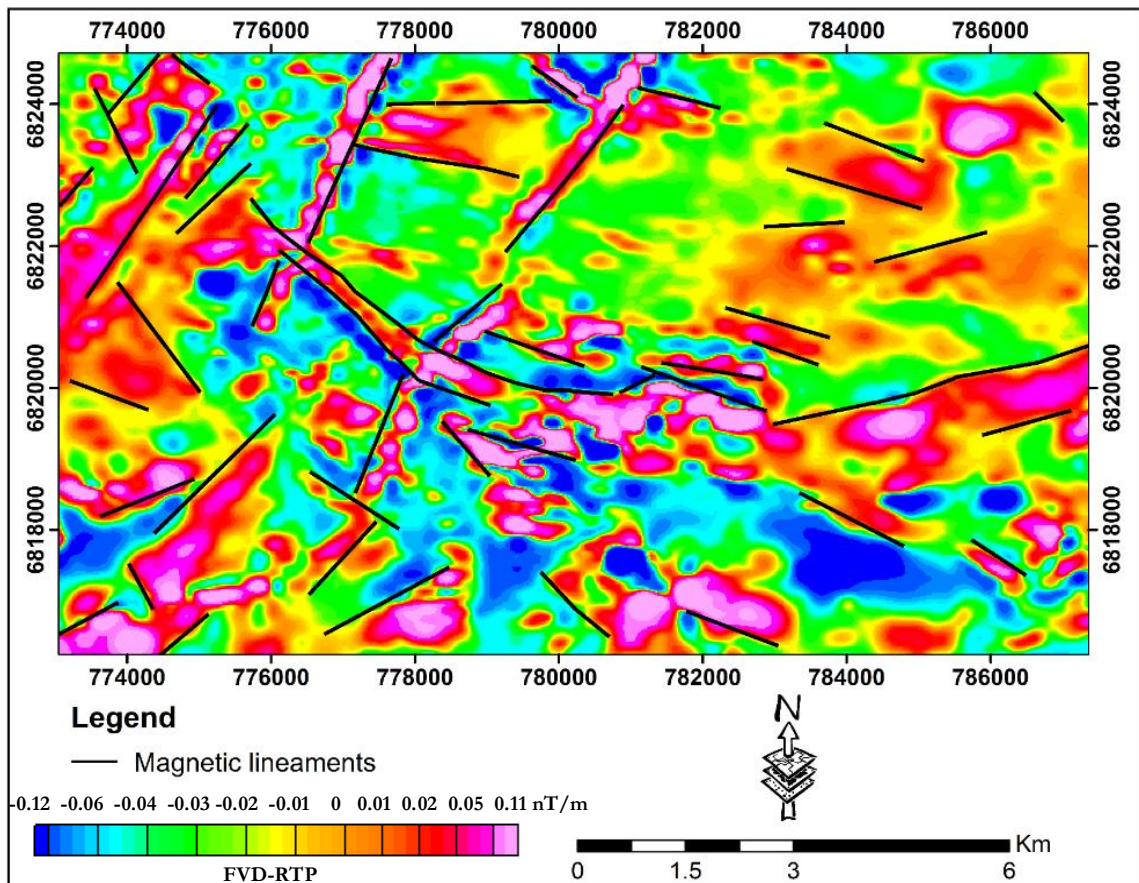


Figure 4-8: Automatic extracted magnetic lineament structures overlaid on First Vertical Derivative (FVD) of the Reduced to Pole (RTP)

As shown in Figure 4-8, the two trending patterns NW-SE and NE-SW from the magnetic lineaments' spatial pattern and distribution are also observable on its corresponding Rose diagram as shown in Figure 4-9 below. These patterns' general orientations are similar to the ASTER and WorldView-3 lineaments but are sharper in magnetic data compared to the two optical datasets. As such the difference are observed in the orientation angles of the lineaments rose diagrams. Orientation analysis comparing the Rose diagram of magnetic data (Figure 4-9), ASTER and WorldView-3 (Figure 4-5) shows that the ASTER's NW-SE dominant orientation angle is at 335 degrees and WorldView-3's NW-SE dominant orientation angle is at 295 degrees but in magnetic data, this dominant angle is at 285 degrees. Thus, magnetics and WorldView-3 data lineaments are similar in this regard compared to ASTER data lineaments. Compared to the second orientation pattern (NE-SW), ASTER's orientation is more pronounced between 0-50 degrees, WorldView-3's between 20-35 degrees and the magnetic data result between 30-50 degrees. These variations imply that the datasets extracted lineaments differently. Further analysis results of the kinematics and sense of motion of each dataset are shown in section 4.5 and the discussion of how this affects the geodynamic interpretation on each dataset is presented in chapter 6. The Rose diagram of the lineaments extracted from magnetic data is shown in Figure 4-9 below showing two sharp orientations of the lineament structures in the study area representing two distinct tectonic episodes that have affected the Haib area: The Orange River Orogeny and Namaqua Orogeny.

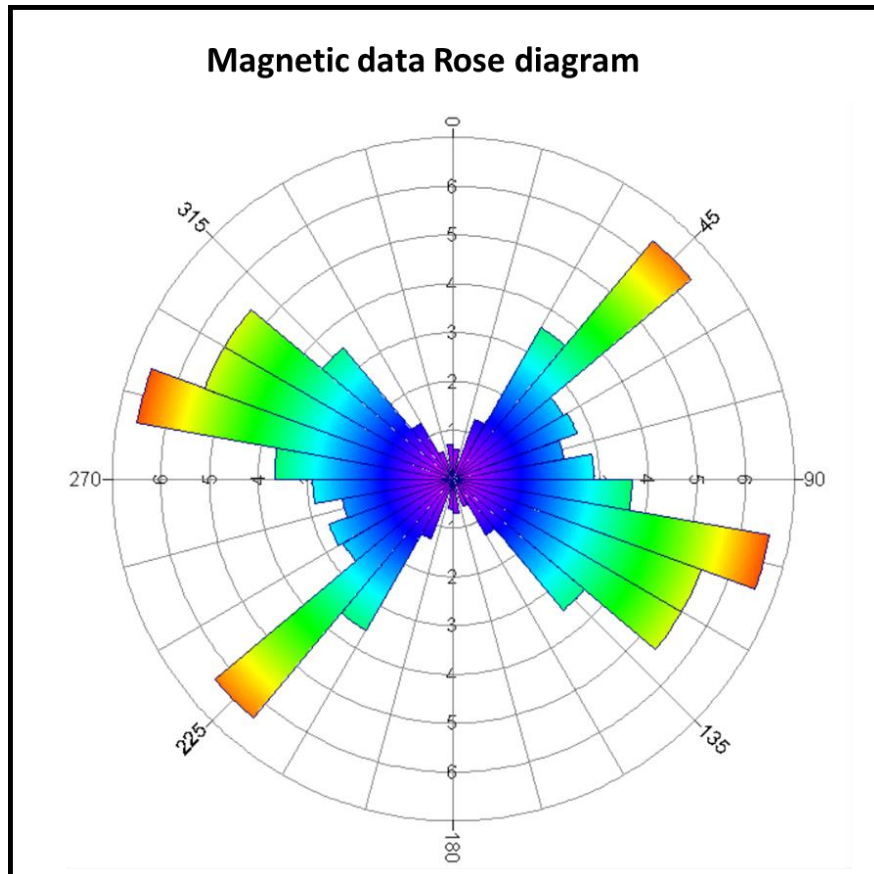


Figure 4-9: Rose diagram from magnetic extracted lineaments showing dominant NW-SE direction and NE-SW minor direction

4.5. Analysis and interpretation of ASTER and WorldView-3 automatic extracted lineaments

This section presents the results of the interpreted lineaments from ASTER and WorldView-3's automatic lineaments shown in Figures 4-2 and 4-3 respectively. The automatic lineament approach may identify any linear features in the study area and non-geological features. However, for tectonic interpretation, only the main geological lineaments such as fault lines are significant (Csillag & Stogicza, 1987). The criteria for analysis and interpretation of the automatically extracted lineaments from ASTER and WorldView-3 into main linear structures were discussed in section 3.8 and the interpreted final lineaments results are shown in figure 4-10 (ASTER interpretation) and figure 4-11 (WorldView-3 interpretation). Analysis of the interpreted lineament structures derived from both ASTER and WorldView-3 automatic lineaments shows that the study area has been affected by two tectonic episodes. The lineament structures are oriented in two different directions. The first being the NW-SE dominant direction and the second direction being the NE-SW. These directions of structures were also observed in the magnetic data. The interpreted results correspond with the published faults on the geological map of the study area (see Appendix V). The most interesting structure from interpretation is the main central curved linear structure that is also present in the magnetic data. The fault analysis indicates that the NE-SW structures in both datasets are displaced by the NW-SE structures. This implies that the NE-SW structures are older than the NW-SE structures. The zoom-in versions indicating analysis of the lineament displacements from ASTER and WorldView-3 datasets are shown in appendix III.

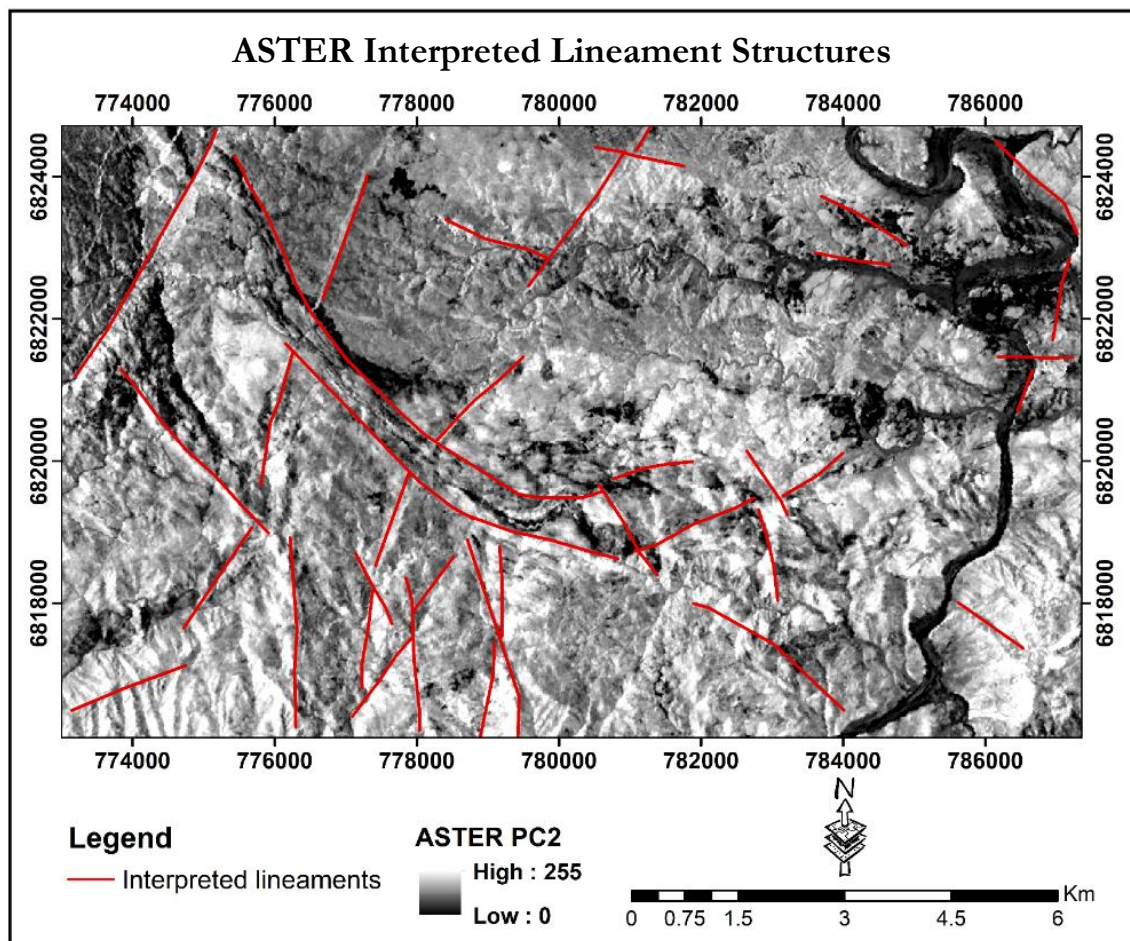


Figure 4-10: ASTER interpreted lineaments showing main linear features in the study area

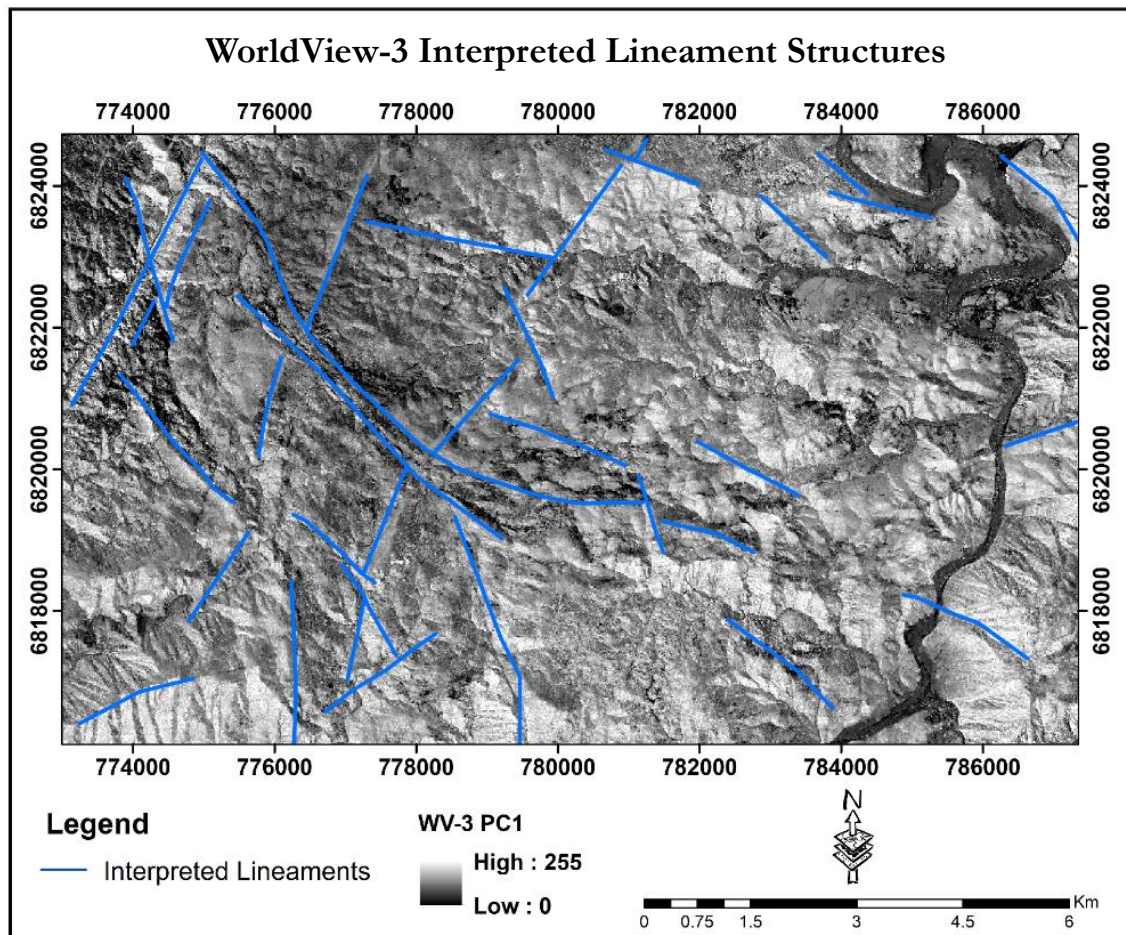


Figure 4-11: WorldView-3 interpreted lineaments showing main linear features in the study area

4.6. Lineaments kinematics and sense of motion of ASTER, WorldView-3 and Magnetic data

This section presents the results of the lineaments kinematics and sense of motion from each dataset and the comparison with each other. The lineaments' sense of motion derived from each dataset was based on the displacement of the lineaments. Very clear displacements were identified as offsets in the mapped linear structures from each dataset and the sense of motion was derived as shown Figure 4-12 (ASTER), Figure 4-13 (WorldView-3) and Figure 4-14 (Magnetics) below. The ASTER data indicates that the sense of motion in the study area is dominantly strike-slip, both dextral and sinistral systems (See zoom versions in Figure 4-12). The sense of motion as indicated with the yellow arrows show the movement of force resulting in the strike-slip faulting. This direction in the sense of motion is consistent on the central main fault moving southeast but changes on the southwest faults and seem to be moving in the north-western direction. This pattern is similar in all the datasets and was also mapped by Colliston and Schoch (2000) on a regional scale.

The WorldView-3 lineaments' sense of motion indicated in yellow arrows as in ASTER data, shows similar results in the area with dominant strike-slip systems: dextral and sinistral (confirmed by the zoom-in versions) as shown in Figure 4-13. As in ASTER data, the WorldView-3 lineaments sense of motion is consistent and corresponds with the regional trend (Eberle et al., 1995). This pattern is also observed in the sense of motion (yellow arrows) of the magnetic lineaments as shown in Figure 4-14. The faulting system is also identified as strike-slip and corresponds to the regional trend as mapped by Colliston & Schoch (2000).

From all the datasets, the fault kinematics and sense of motion analysis show that the NE-SW structures are older since they are offset by the NW-SE structures. The NE-SW correspond to the Orange River Orange Orogeny (2.0 Ga) which was overprinted by the NW-SE younger structures that correspond to the Namaqua Orogeny (1.1 Ga) (Barr & Reid, 1992; Eglington, 2006; Macey et al., 2017).

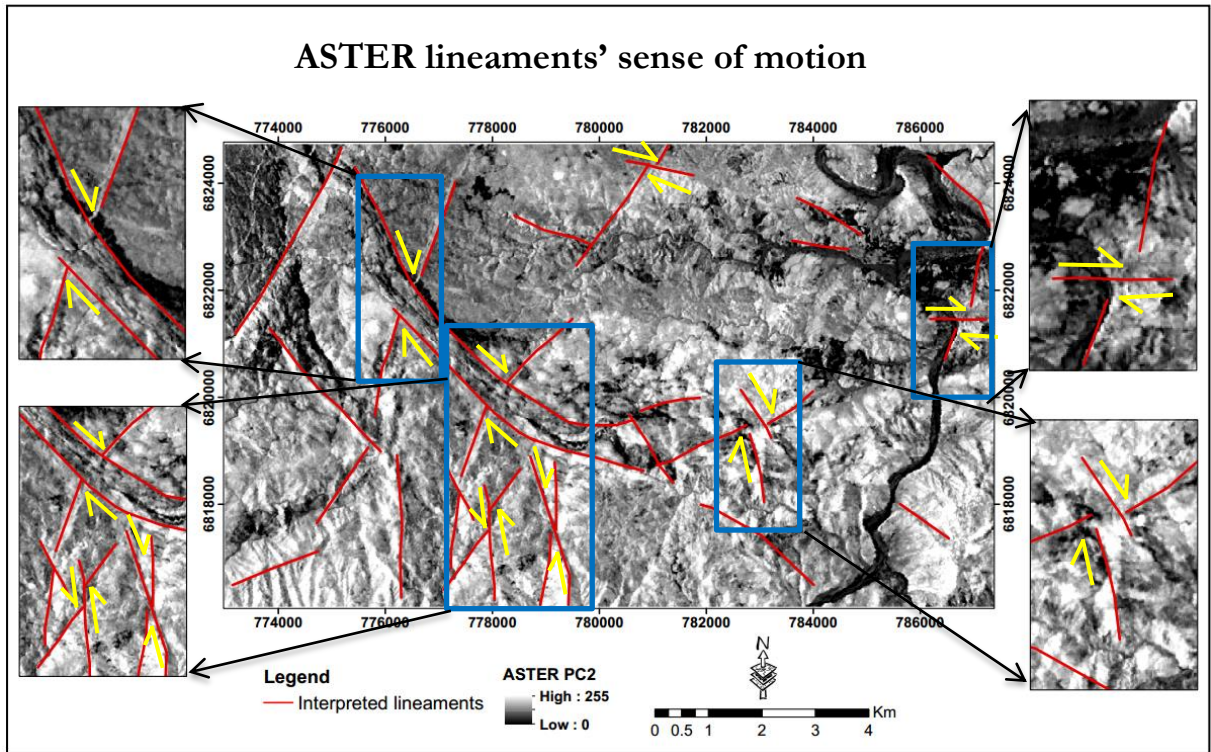


Figure 4-12: The ASTER lineament kinematics and sense of motion showing strike-slip faulting. The yellow arrows show the movement of the lineaments. (Inserts show evidence of strike-slip motion of the lineaments)

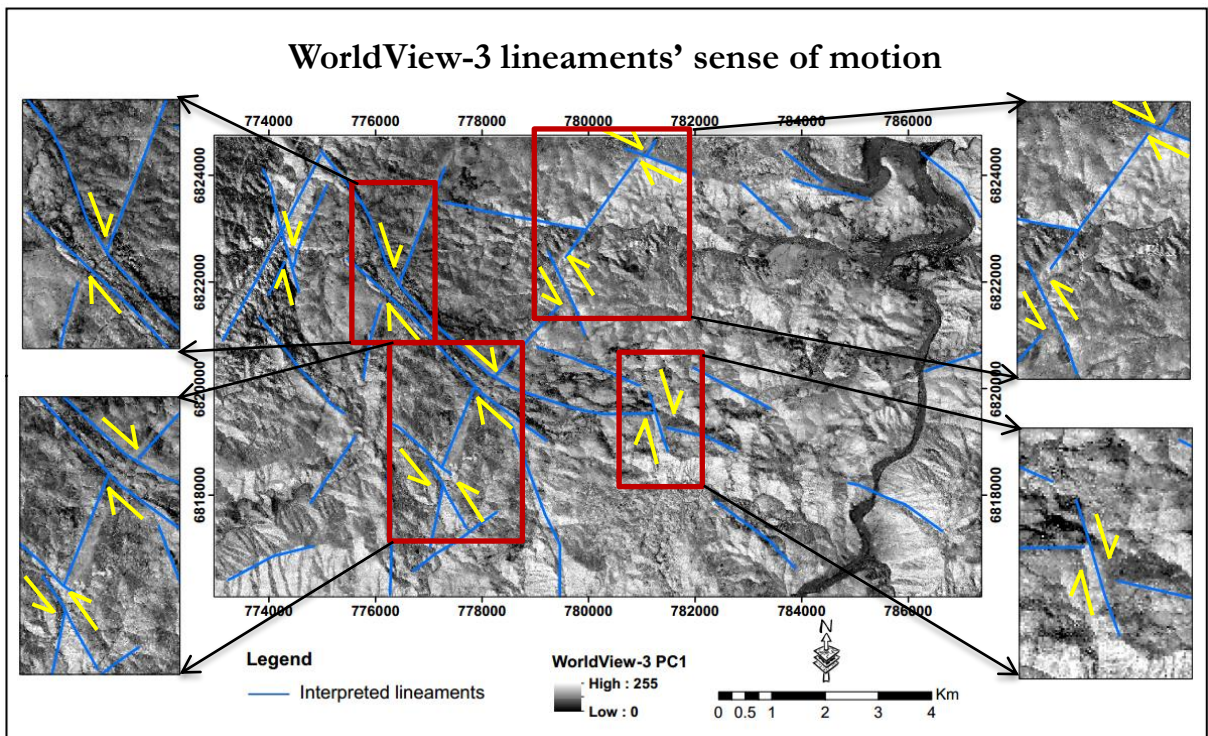


Figure 4-13: The WorldView-3 lineament kinematics and sense of motion showing strike-slip faulting. The yellow arrows show the movement of the lineaments. (Inserts show evidence of strike-slip motion of the lineaments)

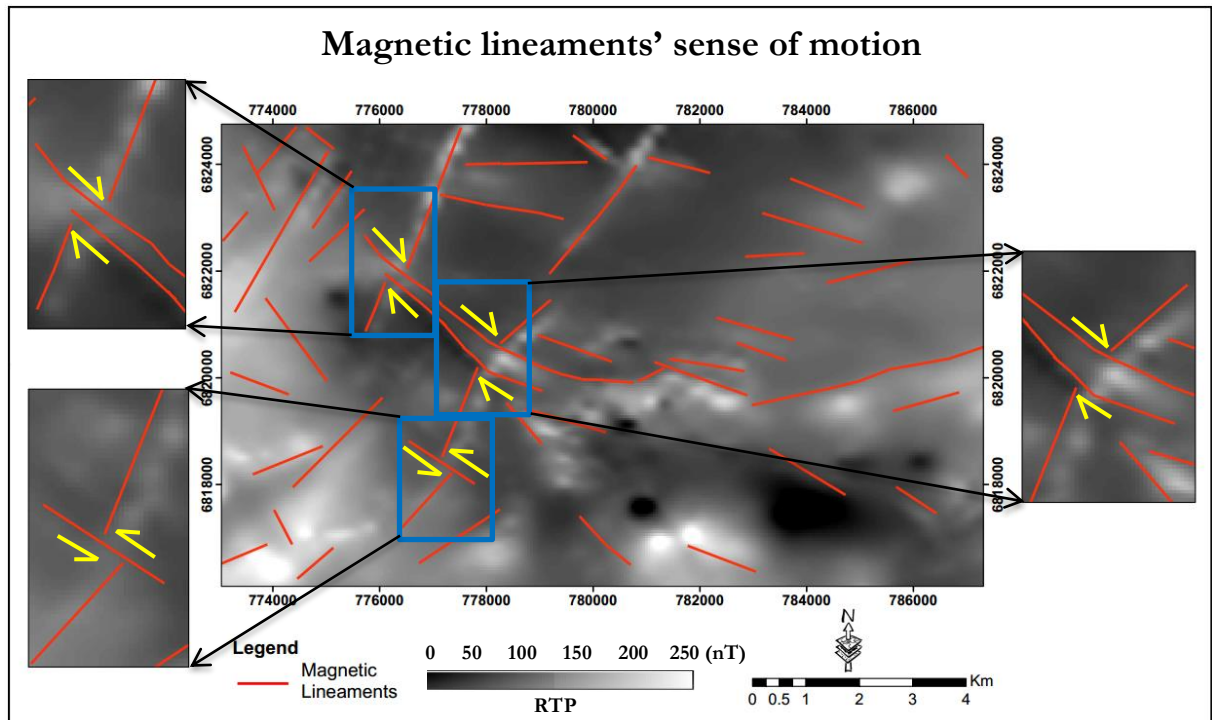


Figure 4-14: The Magnetics lineament overlaid on the Reduced to pole (RTP) grid showing strike-slip sense of motion. The yellow arrows show the movement of the lineaments (Inserts indicate evidence of strike-slip motion of the lineaments)

Even though all the three datasets showed similar lineament sense of motion as presented above, the Rose diagrams of each dataset showed different orientation angles in the dominant NW-SE direction and the minor NE-SW direction indicating that they extracted the force kinematics differently. The ASTER lineament kinematics shows that the maximum principal force σ_1 , which is the shear fracture, is at a higher angle compared to WorldView-3 and Magnetics forcing the extensional forces, the minimum principal force σ_3 at a perpendicular angle to the maximum principal force. The ASTER maximum principal force angle is between $335^\circ - 360^\circ$ based on its Rose diagram (Figure 4-5a), WorldView-3's is lower than ASTER at an angle between $300^\circ - 335^\circ$ (Rose diagram Figure 4-5b) and Magnetics is between $280^\circ - 315^\circ$ derived from its Rose diagram (Figure 4-9). Due to these different minimum principal force angles, the lineaments kinematic diagram of ASTER data shows moderately oblique fracturing (Figure 4-15a) whereas WorldView-3 (Figure 4-15b) and Magnetic data (Figure 4-15c) lineament kinematic diagrams show strongly oblique fracturing. The WorldView-3 and Magnetic lineaments kinematic diagrams are relatively similar (though not exactly) to each other as compared to the ASTER data. For both WorldView-3 and Magnetic datasets, the maximum principal force σ_1 values are at lower angles ($300^\circ - 335^\circ$ and $280^\circ - 315^\circ$ respectively) compared to the ASTER data and the minimum principal force σ_3 , which is the extensional fracture, are similar. The lineaments kinematics diagrams indicate different angles of the causative forces of the principal stress axes in all the datasets based on the Rose diagram interpretation. The lineaments kinematic diagrams for ASTER, WorldView-3 and Magnetic data are shown in Figure 4-15.

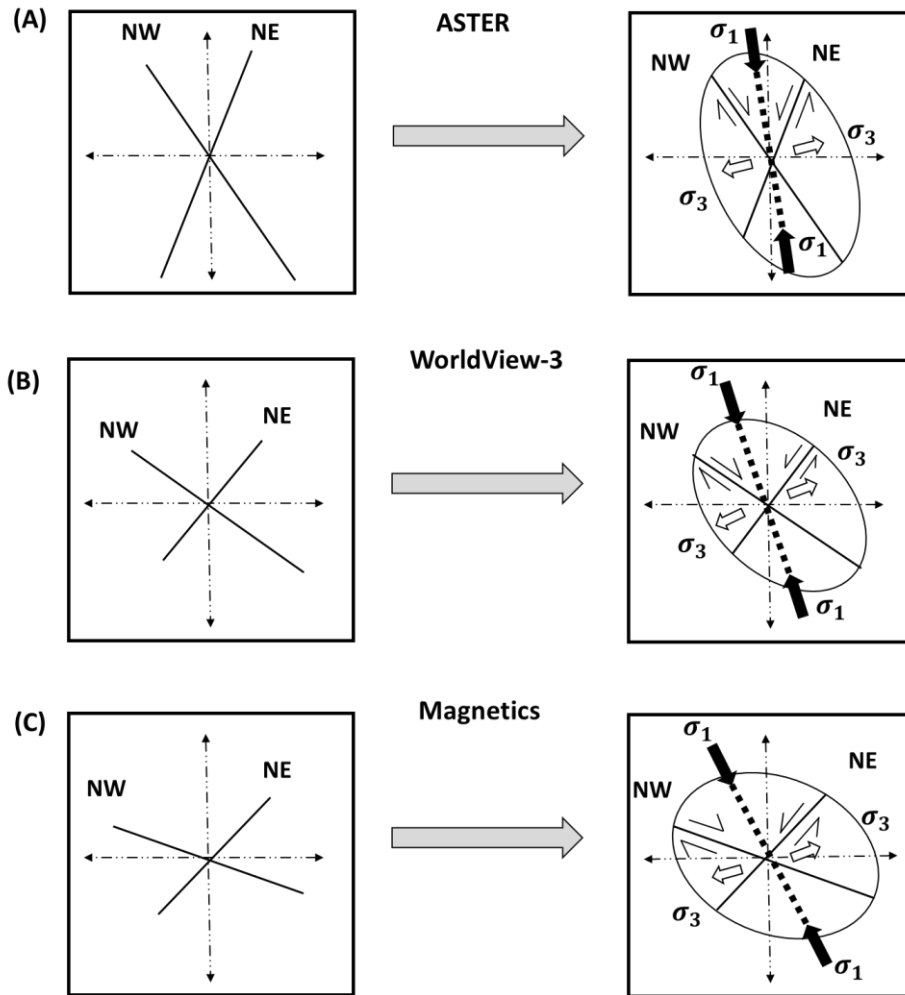


Figure 4-15: Shows the kinematics of lineaments in ASTER data (a), WorldView-3 data(b) and Magnetic data(c) (Note that the NW and NE trend lines represent the NW-SE and NE-SW lineaments in each dataset based on their corresponding Rose diagram orientation angles)

4.7. Lineaments integration from ASTER, WorldView-3 and Magnetic data

The results for the integration of ASTER, WorldView-3 and magnetic extracted lineaments are presented in this section. The criteria for integrating the three sets of lineaments were outlined in section 3.10. In the integration process, the collocated lineaments from at least two of the datasets (in green circles) are shown in Appendix VI. This lineament collocation provides confidence that the mapped lineament from at least any of the two datasets is a true lineament and is considered for integration (Pilkington & Keating, 2004; Cooper & Cowan, 2006; Yeomans et al., 2018). And the lineaments correlation with the topographical expression of the ASTER and WorldView-3 lineaments are shown in appendix VII. The resulting lineament map from the integration of the datasets and its corresponding Rose diagram is shown in Figure 4-16 below. This integrated lineament map indicates two main tectonic episodes in the NW-SE dominant direction and the minor NE-SW direction. These structural patterns are similar to individual datasets. Furthermore, the Rose diagram shows two main orientation directions in the NW-SE and NE-SW more pronounced at 285 degrees and 45 degrees respectively. This orientation pattern is similar to the magnetic and WorldView-3 lineaments. The NE-SW and NW-SE main structural lineament orientations correspond to the tectonic transport directions of the Orange River (2.0 Ga) and Namaqua Orogenic events (1.1 Ga) (Reid et al., 1991; Barr & Reid, 1992; Colliston & Schoch, 2000; Macey et al., 2017) as observed from the lineament analysis of the individual datasets.

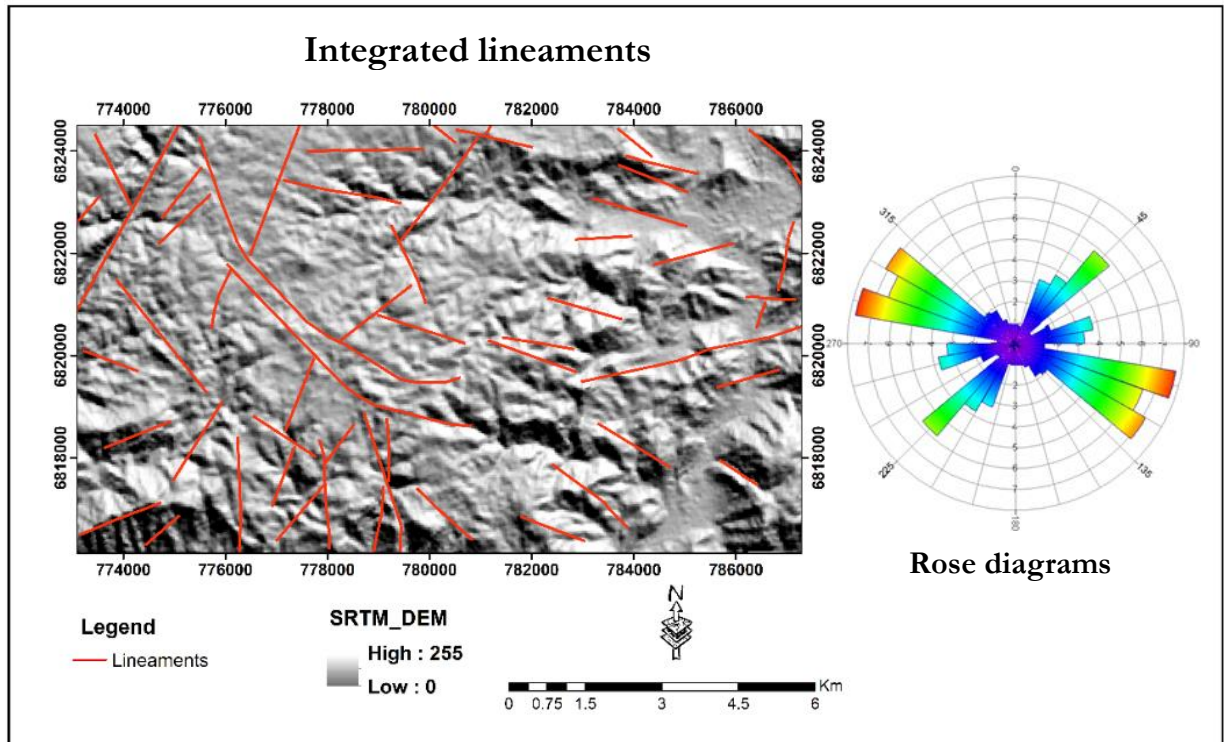


Figure 4-16: Integrated lineaments from ASTER, WorldView-3 and Magnetics with NW-SE and NE-SW spatial patterns draped over a hill-shaded SRTM DEM and the Rose diagram showing dominant NW-SE and NE-SW orientations more pronounced at 285 and 45 degrees respectively.

4.7.1. Comparing and combining integrated lineaments and published structural map of Haib area

The integrated lineament structural map from ASTER, WorldView-3 and Magnetic data (Figure 4-16) were compared with the published structural map by Blignault (1972) in Figure 2-3 to show the differences and the improvement that this research has made on the lineament structures in the study area. Then the final up-dated structural map of the study area was produced by combining the ASTER, WorldView-3, magnetic and geological data of the area resulting in an improved structural map of the area for tectonic and geodynamic interpretation in Chapter 5. The published structural map by Blignault (1972) at the scale of 1: 100, 000 excluded most of the lineaments in the area. This previous map did not show any sense of motion and kinematics of the lineaments which is critical for the tectonic and geodynamic interpretation. Therefore, this study's interpreted structural map included most of the lineament in the area from which the kinematic and sense of motions were derived for tectonic interpretation. It confirmed the already mapped faults by Blignault (1972). The new structural map (Figure 4-17c) shows improved lineament structures of the local Haib area compared to the previously published structures striking in the NW-SE and NE-SW directions and provide relative chronological ages of the lineaments based on the offset evidence and sense of motion.

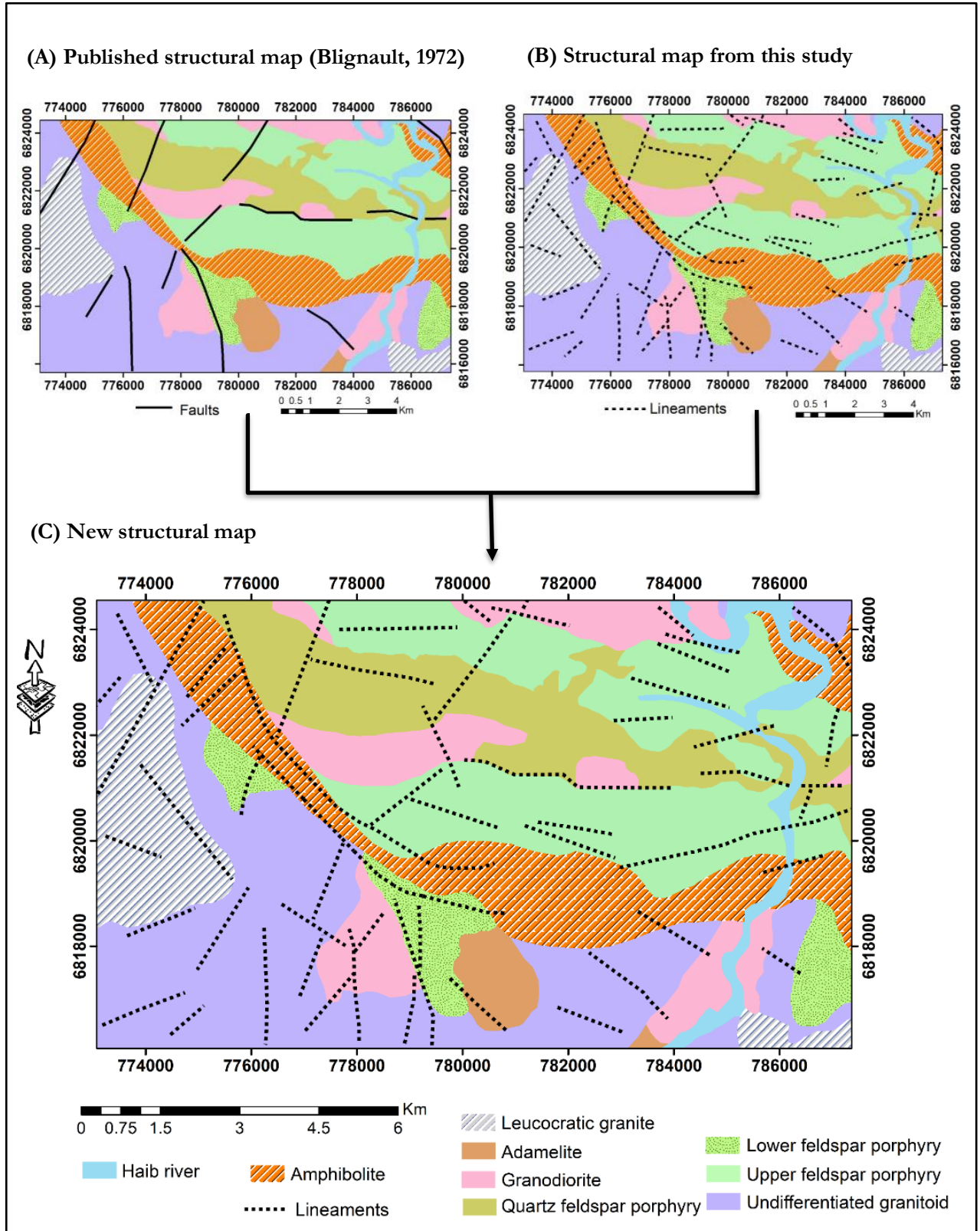


Figure 4-17: The combination of old (published) and new lineaments to produce the new structural map of Haib area; (A) Faults from the published structural map by Blignault, (1972) (B) Lineament delineated from this study (C) The new structural map of Haib area based on the analysis as presented in this study and published map (Blignault, 1972)

4.7.2. New structural map lineaments kinematics and sense of motion

The general lineaments kinematics and sense of motion of the new structural map of Haib area are presented in this section. Figure 4-18 shows the lineaments kinematics and sense of motion derived from the new lineament structures of the Haib area. As shown in Figure 4-15a, the lineaments kinematics indicate the maximum principal force σ_1 , (shear fracture) in the NW-SE direction resulting in the extensional forces, the minimum principal force σ_3 at a perpendicular angle to the maximum principal force moving in the NE-SW direction. The two lineaments strike-slip lineaments shown in the lineaments kinematic diagram Figure 4-18a are based on the accurate angles of the Rose diagram of the integrated lineaments (Figure 4-16) and indicate that Haib area has indeed been affected by two tectonic episodes in the NW-SE and NE-SW tectonic transport directions. This lineament kinematic diagram is more similar to the magnetics and WorldView-3 data compared to ASTER data as shown in Figure 4-15. Furthermore, the red arrows in Figure 4-18b shows that the newly delineated lineaments' sense of motion in the area is dominantly the strike-slip faulting (both the dextral and sinistral systems), confirming the analysis from the individual datasets in section 4.6. Analysis of these lineaments shows that the NE-SW lineament structures are displaced by the other set of lineaments in the NW-SE direction. According to Tarbuck et al. (2017), between any two or more faults or lineaments, the one that cross-cut (displace) the other is younger. In the Haib area, the NW-SE lineaments cross-cut the NE-SW lineaments. Therefore, the relative chronology shows that the NE-SW lineaments are older than the NW-SE trending lineaments corresponding to Orange River and Namaqua tectonic events respectively (Colliston & Schoch, 2000; Cornell et al., 2006; Macey et al., 2017; Thomas & Cornell, 1994).

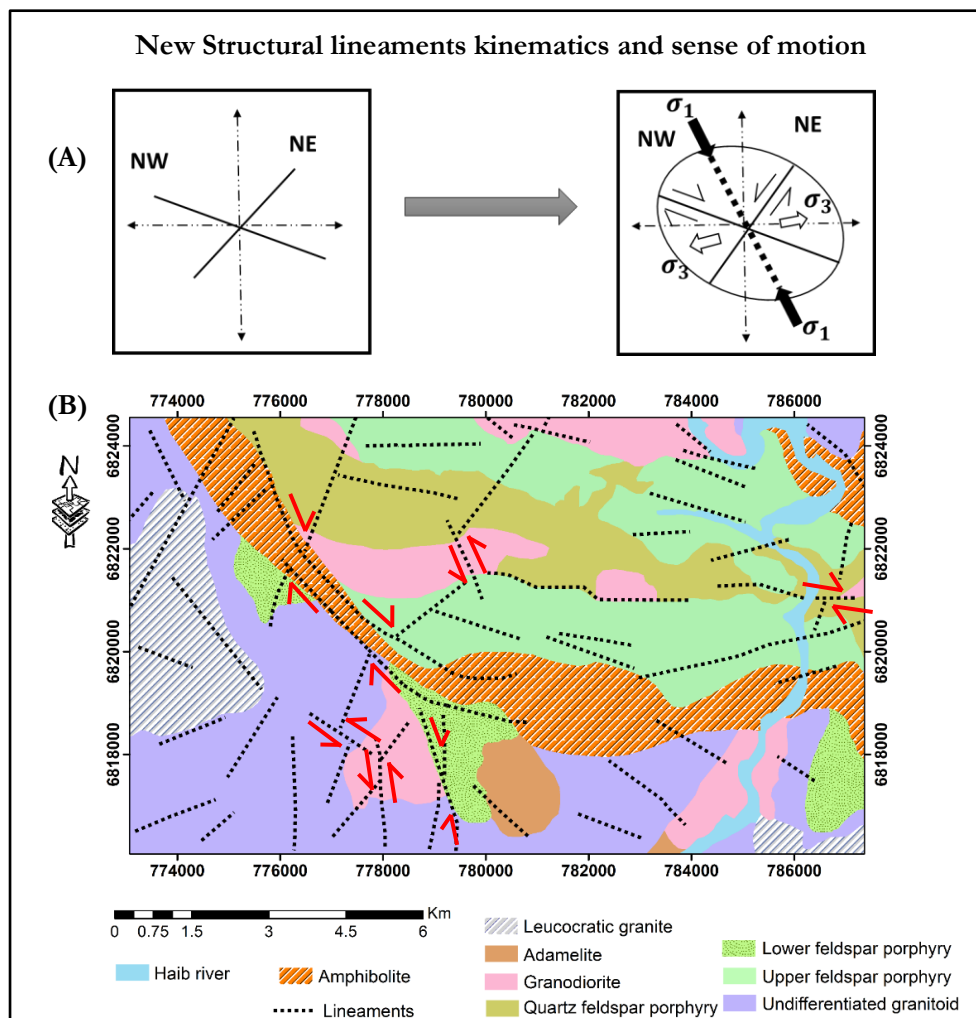


Figure 4-18: Haib study area lineaments kinematics diagram (A) and sense of motion (B) derived from integrated lineaments from ASTER, WorldView-3, Magnetic data, and previously published structural map

4.8. ASTER Band ratios

The ASTER band ratios were performed to help in the interpretation and validation of the final integrated lineaments on the new structural map of the Haib area (Figure 4-18 above). According to Chernicoff et al (2002), mineralization in a porphyry deposit is primarily controlled by lineament structures including veins, vein sets, stockworks, fractures, faults, and breccia pipes. Mapping the mineral occurrence reveal the structural patterns and help to validate and interpret tectonic lineaments (Porwal et al., 2006; Sandrin, 2006). Hence, this research mapped the Al-OH, Mg-OH and FeO mineral content groups to aid the tectonic interpretation of the Haib area. The results of these mineral group band ratios and the combined map of the same band ratios in Red, Green and Blue channels respectively are shown in Figure 4-17. The Cudahy (2012) algorithm stretch values for each of the band ratios worked perfectly in the Haib area, probably since it is a semi-arid area like Australia where the algorithm was initially designed for. The Al-OH is the main mineral group content present in the area ranging from moderate to high values on the scale bar, seconded by Mg-OH/Carbonate and then Ferric oxide content is the least in the area. As seen in the band ratios, the delineated lineaments are clearly seen as linear features and confirm the lineaments analysis done in the previous sections. However, NW-SE line running through the FeO mineral content map (Figure 4-19c) is the effect of the mosaicking of the two ASTER scenes. The mapped linear structures are also visually captured in the individual band ratios. The new structural lineaments shown in Figure 4-17d coincide mostly with the mineral group contents particularly Al-OH and Mg-OH/ Carbonate in the northeast, western parts and the centrally curved lineaments of the study area which corresponds with the mapped new structures. The combined Red/Green/Blue of Al-OH/Mg-OH/FeO respectively in Figure 4-19d shows the spatial and structural relationships of the mineralization with the new lineament structures.

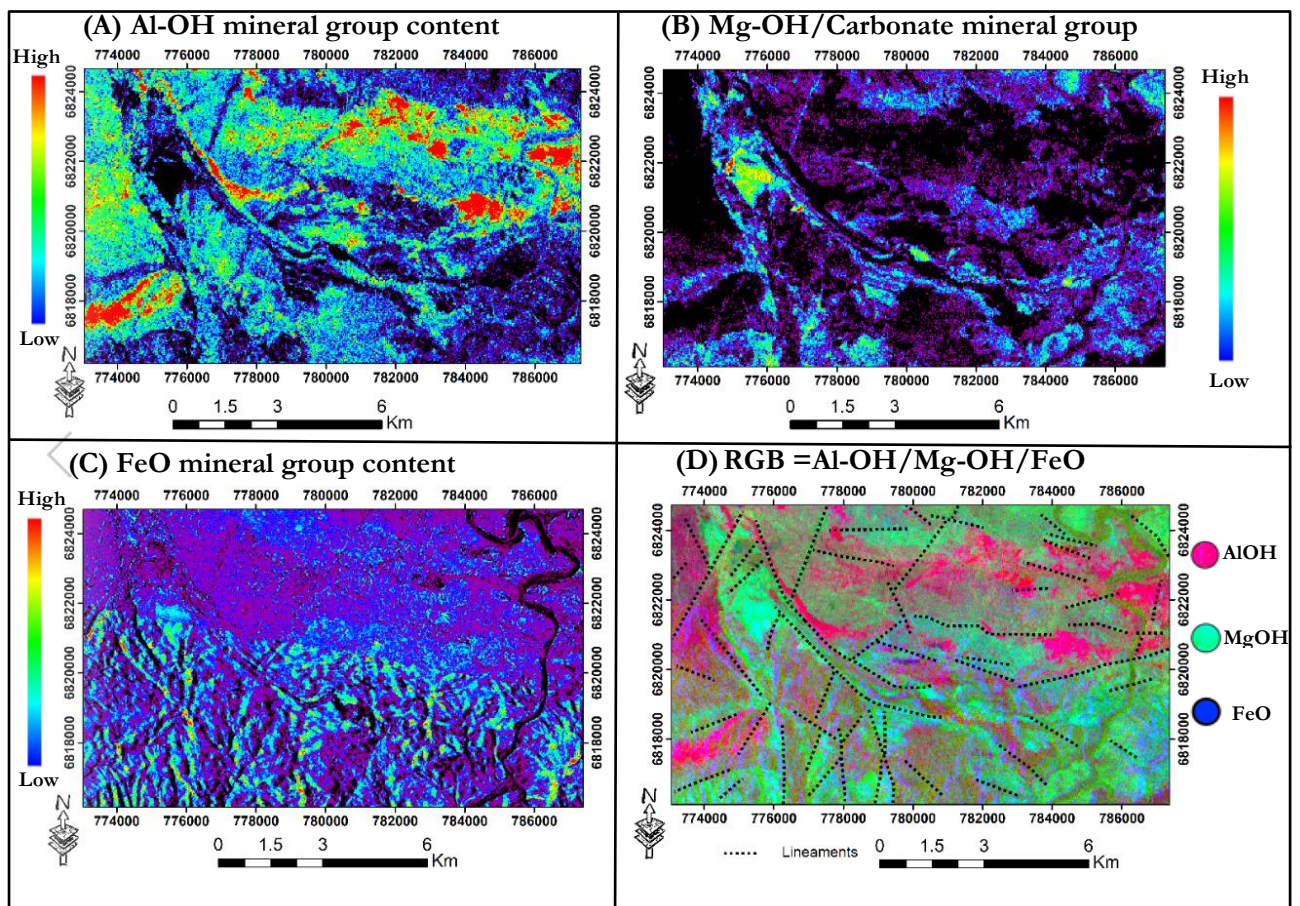


Figure 4-19: ASTER Cudahy (2012) band ratio-based algorithm (a) Al-OH mineral group content (b) Mg-OH/Carbonate mineral group content (c) Ferric oxide mineral content (d) RGB combination of Al-OH, Mg-OH/Carbonate, Ferric oxide with the lineaments showing the structural relationship

5. TECTONIC EVOLUTION AND GEODYNAMIC INTERPRETATION

5.1. Introduction

This chapter presents and describes the tectonic evolution and geodynamic interpretation of Haib area in the Paleoproterozoic Richtersveld Subprovince within the Namaqua sector of the Namaqua – Natal Province, southern Namibia as shown in Figure 2-3. The tectonic evolution and geodynamic activities of the Haib area were derived based on the combined structural information from ASTER, WorldView-3, and aeromagnetic data together with lithological and geochronological data from previous research on southern Africa's evolution in general. A proposed tectonic evolution model has been presented to improve the understanding of the tectonic and geodynamic processes in the area. In addition, tectonic models interpreted from three selected topographic-based profiles across some lineament structures delineated in this research were used to propose the past geodynamic processes in the area.

5.2. Tectonic evolution

Tectonically, the Namaqua – Natal Province makes up a significant segment of the global network of 'Grenville-aged' belts (Jacobs et al., 2008a). These belts were formed during a major period of continental collision and accretion during the time of assembly of the Rodinia supercontinent (Cornell et al., 2006; Thomas & Cornell, 1994; Thomas et al., 1993). The study area has undergone complex tectonic development due to geodynamic and tectonic activities that have led to the crustal development of southern Africa (Begg et al., 2009; Schijndel, 2013). The southern Africa continent's tectonic evolution has had multiple continental-continental collisions, amalgamation, rifting and crustal extensions during its development to the present tectonic state (Anhaeusser, 1990; Begg et al., 2009; Colliston & Schoch, 2000; Davies & Coward, 1982; Thomas & Cornell, 1994; Thomas et al., 1993). These processes have affected and contributed to the tectonic evolution and geodynamics of the study area from the early Proterozoic era to the present (Cornell et al., 2006; Macey et al., 2017).

The evolution of the Haib area started with magmatism/volcanism and plutonic activities which occurred in an island arc setting in the early Proterozoic age (Barr & Reid, 1992; Colliston & Schoch, 2000). This magmatic episode took place approximately 2.0 Ga according to radiometric dating by Barr & Reid (1992) and led to the emplacement of the Orange River Group which comprises the undifferentiated granitoid, lower feldspar porphyry and upper feldspar porphyry intrusive units in the study area (Figure 2-4). This Orange River Group was then affected by the Paleoproterozoic tectonism within the major Eburnean event (Macey et al., 2017). It is during this event when the San Francisco Craton in South America and the Congo Craton in West-Central Africa collided into one crustal block (Thomas et al., 1993). This major tectonic event affected the Richtersveld Subprovince and the Haib area in particular in Southern Namibia, and it is locally known as the Orange River Orogeny (Cornell et al., 2006; Macey et al., 2017; Thomas et al., 1993). As shown in Figure 5-1(a) below, the Orange River Orogeny was characterized by compression NW-SE tectonic force direction forming strike-slip faulting in the NE-SW direction perpendicular to the tectonic force orientation and folding. This Paleoproterozoic tectonic episode deformed and metamorphosed the Orange River Group in the Haib area to a low-grade greenschist metamorphic facies condition between 2.0 – 1.7 billion years ago (Anhaeusser, 1990; Colliston & Schoch, 2000; Connelly et al., 2018; Eglington, 2006; Reid et al., 1991).

Furthermore, the continued compression of the Orange River Orogeny led to magmatism and plutonic intrusions between 1.9 – 1.7 billion years ago, which resulted into the formation of the Vioolsdrift and Richtersveld Intrusive Suites in the area (Blignault, 1977; Sithole, 2013). This intrusive episode resulted in the emplacement of the Haib hydrothermal copper porphyry mineralization (Connelly et al., 2018). According to radiometric dating by Barr & Reid (1992) and Ngcofe et al., (2013) in separate studies, the Haib copper mineralization is between 1.7 – 1.6 billion years old. After these events in the Haib area, began the Mesoproterozoic tectonism which started with plutonism during rifting, ocean spreading and subduction phases in an event called the Mesoproterozoic Namaquan Wilson Cycle which took place between 1.6 – 1.2 billion year ago (Cornell et al., 2006). This event was characterized by crustal extension and intrusions. Lastly, the evolution of the Haib area closed with the Mesoproterozoic collision of the Namaqualand and the Archean Zimbabwe-Kaapvaal Craton into the Kalahari Craton which was part of the major Kibaran event as shown in Figure 5-1(b). This tectonic event was a compression episode known as the Namaqua Orogeny (1.4 – 1.1 billion years ago) (Anhaeusser, 1990; Colliston & Schoch, 2000; Connelly et al., 2018; Eglinton, 2006; Macey et al., 2017; Reid et al., 1991; Jacobs et al., 2008). The Namaqua Orogeny was characterized by compression NE-SW tectonic force, resulting in strike-slip shearing and faulting in the NW-SE orientation direction, folding and thrusting (Macey et al., 2017). Furthermore, the continued Namaqua deformational event led to medium to high-grade metamorphism and overprinted the Orange River Orogeny structures as evidenced by the cross-cutting relationship (Figure 4-15) observed in this research and all igneous assemblages (Begg et al., 2009; Schijndel, 2013; Anhaeusser, 1990; Barr & Reid, 1992; Cornell et al., 2006). According to Sithole (2013), “the Namaqua Orogeny event resulted in an extensional component in the Richtersveld Subprovince and dextral pulling apart and rifting during oblique shearing in the Koras and Sinclair groups” in Figure 5-1(b). The Namaquan Wilson Cycle and the Namaqua Orogenic events occurred next to each other and overlapped in space and time, as such their structural impacts are relatively close in space and time (Thomas et al., 1994). Appendix VIII shows a summarized table of the events in the Haib area.

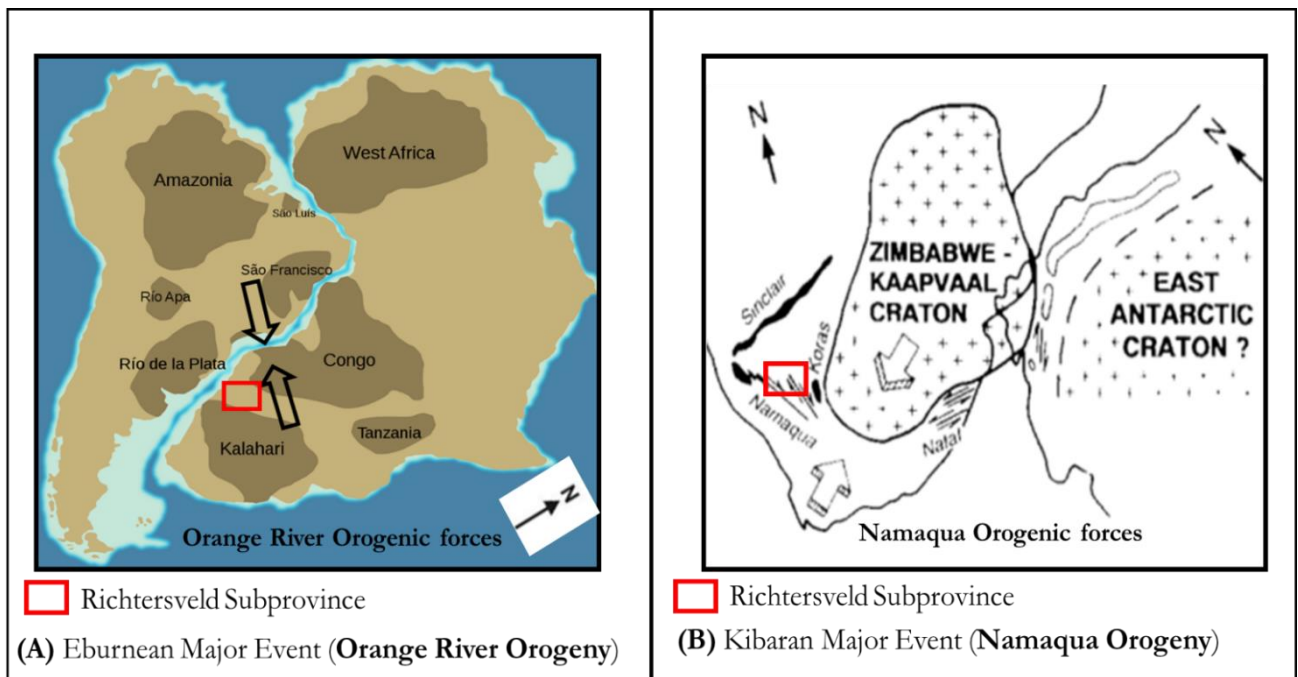


Figure 5-1: Major tectonic events in the study area (A) Collision of San Francisco and Congo Cratons forming NE-SW ductile strike-slip faulting of the Orange River Orogeny (2.0 – 1.7Ga) (B) Collision of the Namaqualand and Zimbabwe-Kaapvaal Craton forming NW-SE ductile strike-slip faulting of the Namaqua Orogeny (1.4-1.1Ga) after Thomas et al., (1993) and Cornell et al.,(2006)

5.3. Tectonic evolution and geodynamic model interpretation

The proposed tectonic model and geodynamic interpretation of the Haib area is based on the structural information from the new structural map (delineated from this study) from ASTER, WorldView-3 and aeromagnetic data (Figure 4-19b) together with topographical variations, ASTER band ratios (Figure 4-20) and geological (lithological and geochronological) data from literature to help in the understanding of the geodynamic processes of the study area.

The Richtersveld Subprovince gained more stability and there were no other major tectonic events after the Mesoproterozoic tectonism compared to other terranes within the Namaqua – Natal Province (Macey et al., 2017). But the subprovince has undergone tectonic complex processes including compression, extensions and possible rifting multiple times between early Paleoproterozoic to late Mesoproterozoic geologic times and possible reactivation thereafter (Begg et al., 2009; Eglington, 2006; Indongo, 2017; Macey et al., 2017).

Based on literature, the compression forces A, B, C and D (Figure 5-2) resulted in the formation and placement of the current position of the Richtersveld Subprovince within the Namaqua – Natal Province between (2.0 – 1.1Ga) (Begg et al., 2009; Cornell et al., 2006; Eberle et al., 1995; Indongo, 2017; Macey et al., 2017; Thomas & Cornell, 1994). These are the major drivers in the tectonic evolution and geodynamics of the Haib area. The forces A and B are the compressional forces of the collision and amalgamation of the San Francisco and Congo Cratons respectively during the Eburnean event (Figure 5-1a) that resulted in the Orange River Orogeny. And the forces C and D are compressional forces due to the collision and amalgamation of the Zimbabwe-Kaapvaal and the Namaqualand Cratons during in the Kibaran event (Figure 5-1b) that resulted in the Namaqua Orogeny. All these forces originated from outside the Haib study area, resulting in strike-slip faulting (Thomas et al., 1993). Furthermore, the small red arrows (Figure 5-2) indicate the extensional component directional movement from the Namaquan Wilson Cycle which overlaps with the Namaqua Orogeny (Anhaeusser, 1990; Colliston & Schoch, 2000; Cornell et al., 2006; Schijndel, 2013). These forces were responsible for the strike-slip faulting, intrusions, folding and possible extension of the crust. The directions of these forces are consistent with the results obtained in this study and the literature.

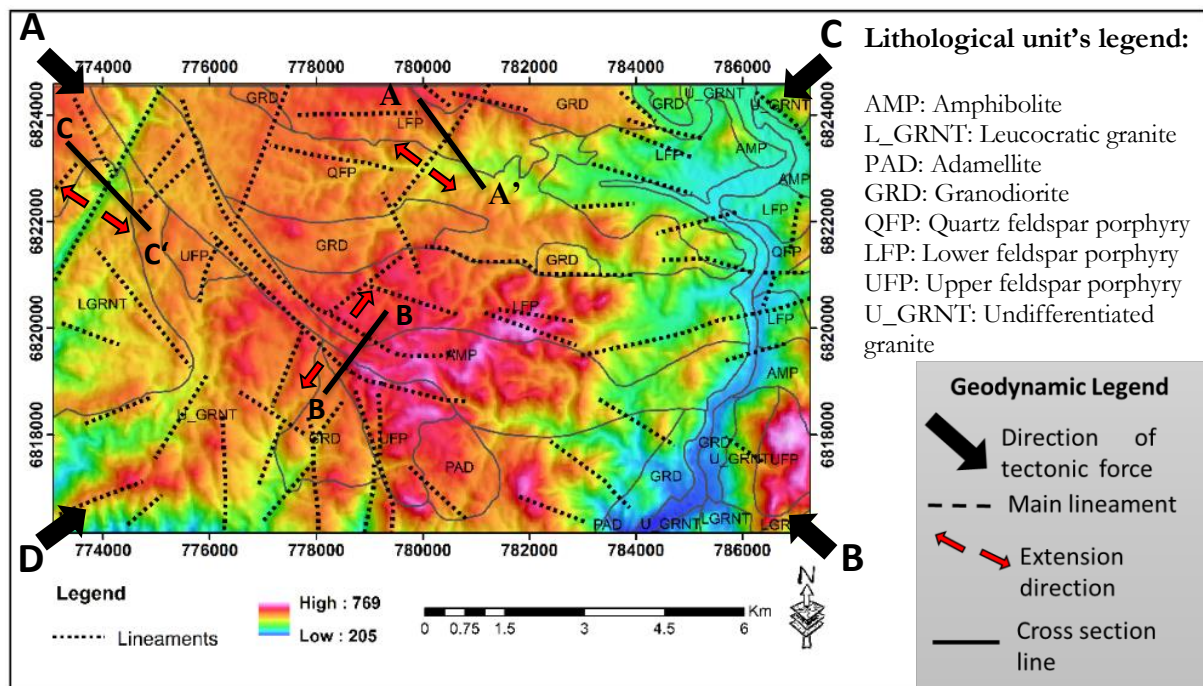
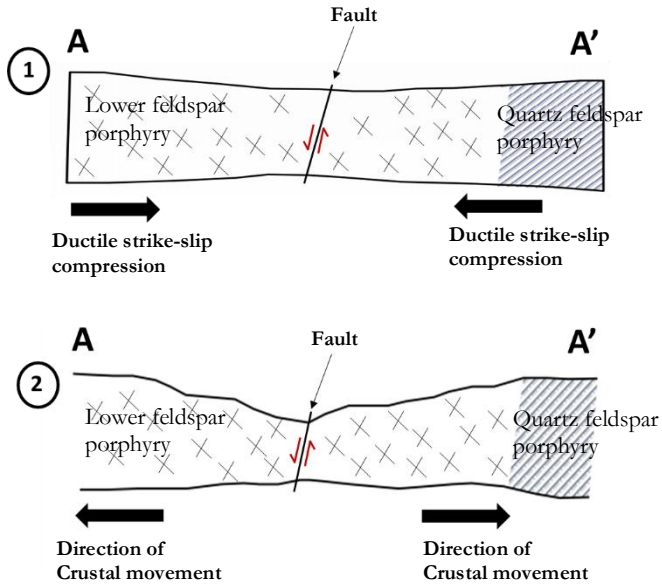


Figure 5-2: Geodynamic interpretation of the Haib area, with the topographical expression (cross-section lines A, B, and C) and the delineated lineaments from this study over the lithological formations. The compressional forces A, B, C and D in the NW-SE and NE-SW are representing the Orange River and Namaqua tectonic force directions respectively. The smaller red arrows represent extensional forces from the Namaqua Wilson Cycle.

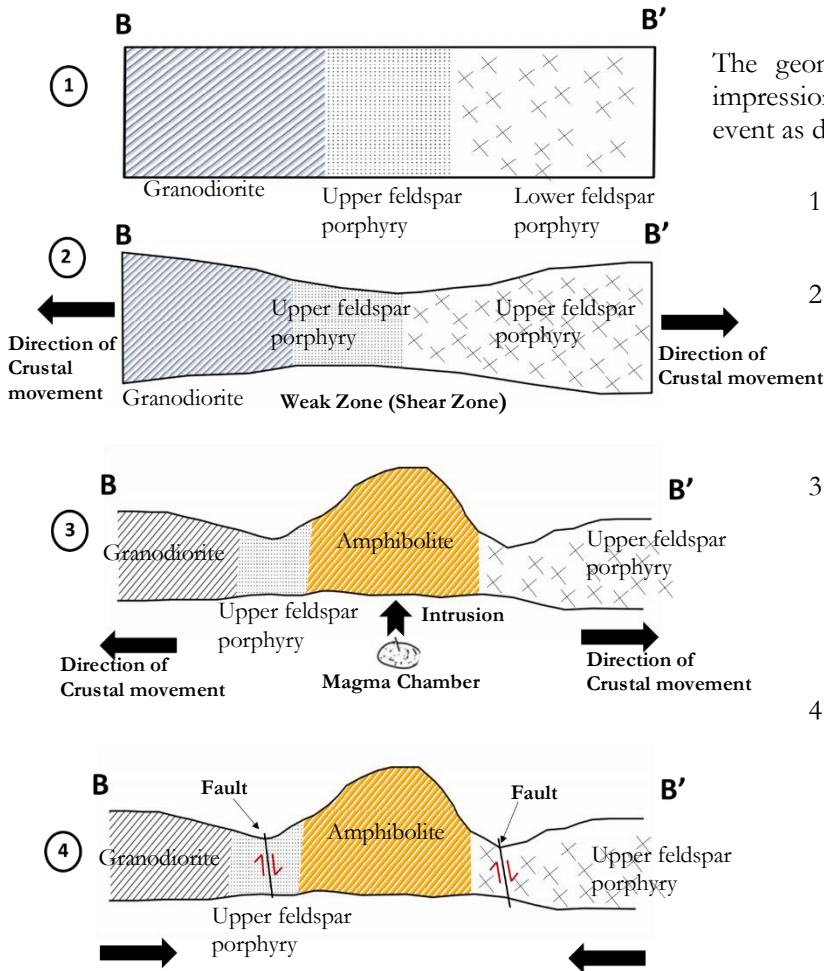
The 2D tectonic schematic models of the three selected topographic-based profiles A, B and C (Figure 5-3 to 5-5) were chosen from Figure 5-2 to explain the evolution of the tectonic movements of the lithological blocks during the Orange River Orogeny, Namaquan Wilson Cycle and Namaqua Orogeny as presented in section 5.2.



The geomorphological landform cross-sectional and tectonic impression from **A** to **A'** was affected by more than one tectonic event as discussed below:

1. The 2.0 billion years old Lower feldspar porphyry and the 1.9 billion years old Quartz feldspar porphyry were compressed and deformed during the Orange River Orogeny (2.0 – 1.7Ga) creating strike-slip faulting. The Orange River Orogeny as shown in Figure 5-1, resulted in ductile compressional faulting causing strike-slip crustal block movements.
2. Subsequently the Namaquan Wilson Cycle (1.6 – 1.2Ga) with spreading and extensional phases appeared to have pulled apart the crust, moving the Lower feldspar porphyry and Quartz feldspar porphyry away from each other through the already existing weaker zone (strike-slip fault reactivation).

Figure 5-3: A cross-section of the topographical (geomorphological) impression and tectonic model across Lower feldspar porphyry and Upper feldspar porphyry units.



The geomorphological landform cross-sectional and tectonic impression from **B** to **B'** was affected by more than one tectonic event as discussed below:

1. The pre-deformational stable phase in the Mesoproterozoic age.
2. Crustal pulling apart created a weaker zone (Shear zone) along the boundary between the 2.0 billion years old Upper and Lower feldspar porphyry units during the Namaquan Wilson Cycle extension and spreading phases.
3. The prolonged Namaqua Wilson Cycle extension created more weak spots through which the 1.7-1.6 billion years old Amphibolite intrusion came up in between the lithological boundary of the Lower and Upper feldspar porphyry units. The extensional phase initiated the intrusion.
4. Subsequently, in the Namaqua Orogenic compressional episode (1.4 – 1.1 Ga), the forces reactivated the weak spots from the previous events in 2 and 3 in a different direction creating ductile deformation which resulted in the strike-slip sense of motion and faulting along the weak boundaries of the Amphibolite intrusion and the two feldspar porphyry units. The strike-slip faulting, as shown in Figure 5-4, stage number 4 was as a result of the Namaqua Orogenic episode.

Figure 5-4: A cross-section of the topographical (geomorphological) impression and tectonic model across the Granitoid, Upper feldspar porphyry, Amphibolite, and Lower feldspar porphyry.

The geomorphological landform cross-sectional and tectonic impression from **C** to **C'** was affected by more than one tectonic event as discussed below:

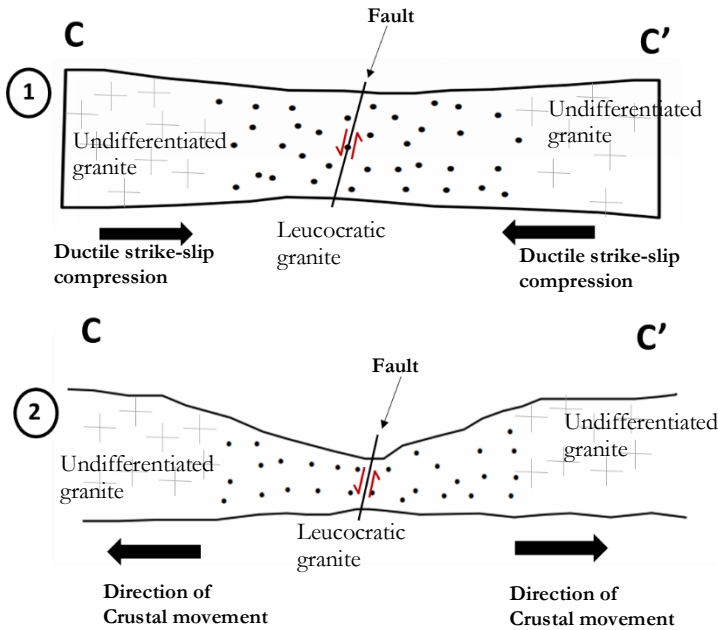


Figure 5-5: A cross-section of the topographical (geomorphological landform) impression and tectonic model across the Undifferentiated granite through the Leucocratic granite to another unit of the Undifferentiated granite.

1. The 1.9 billion years old Leucocratic granite and the 2.0 billion years undifferentiated granite were compressed in the Orange River Orogenic episode as part of the major Eburnean event resulting in the ductile deformational strike-slip faulting in the Leucocratic granite.
2. The event in 1 above was followed by the extensional pulling apart of the 2.0 billion years old undifferentiated granite and the 1.9 billion years old Leucocratic granite during the Namaquan Wilson Cycle (1.6 – 1.2Ga) which created a depression. This event reactivated the strike-slip faulting in the Leucocratic granite

These two-dimensional (2D) tectonic schematic models suggest that the Haib area has been affected by tectonic compression (during Orange River and Namaqua Orogenic episodes), magmatic intrusion activities, crustal extension block movements related to the Namaquan Wilson Cycle and possible rifting (Cornell et al., 2006). These proposed models attempt at improving our understanding of the tectonism of the area from the Early Paleoproterozoic geologic time, approximately 1.1 to 2.0 billion years ago. The study area has undergone multiple compression and extension episodes since its formation thereby forming a tectonically complex crustal block (Corner, 2000; Thomas & Cornell, 1994). These multiple crustal movements have resulted in weaker zones in the area forming fractures and faults in which intrusions have come through, and this seems to be consistent throughout the study area. This interpretation corresponds to the research findings by Sithole (2013), Macey et al (2017) and Eglinton (2006) in the Richtersveld Subprovince. This possible interpretation and literature have been used to propose a tectonic evolution model of the local Haib area presented in section 5.3.1 below.

5.3.1. Characterizing observable structures with the tectonic events and proposed tectonic evolution model

This section characterizes the delineated and observed structures in Figure 4-15 (New structural map of Haib) mainly the lineaments into the tectonic events that affected the area between 2.0 Ga to 1.1 Ga. Based on this classification and the results obtained from this research, a proposed tectonic evolution model sketch has been presented to illustrate one possible tectonic evolution interpretation of the Haib area from the early Paleoproterozoic era through the Mesoproterozoic geologic time in the area. The 2D tectonic models described above indicate the tectonic forces in the area at different geological times in the area. These forces correspond with the description in the literature and have been used to show tectonic force directions on the proposed tectonic model. However, the starting geology in the pre-Paleoproterozoic era is not fully known in the area and has not been addressed in this research. As outlined in section 5.2, the Haib area has been mainly tectonically deformed by the Orange River Orogeny (2.0 – 1.7Ga) and Namaqua Orogeny (1.4 – 1.1Ga). But the latter seemed to have overlapped with the Namaquan Wilson Cycle (1.6 – 1.2Ga) whose impact in the area according to Cornell et al., (2006) and the results obtained in this study were the extensional component in the Richtersveld Subprovince. The NE-SW strike-slip faulting corresponds to the Orange River Orogeny whose tectonic direction was in the NW-SE orientation. This event was overprinted by the extension and strike-slip faulting from the Namaquan Wilson Cycle and Namaqua Orogeny. The extensional component in the area could be deduced from the topographic-based profiles A, B and C shown in Figure 5-2. However, these topographic lows could also be related to erosional effects along a weak spot and not necessarily extensional indicators. A summary of the observed structures and their mechanisms is given in table 5-1 and the Haib proposed tectonic evolution model sketch is presented in Figure 5-6.

Observable Structure	Characteristics/Mechanism	Event
NE-SW lineaments	<ul style="list-style-type: none"> • Strike-slip • Offset • Formed by NW-SE tectonic force • Low grade metamorphism 	Orange River Orogeny (2.0-1.7Ga)
Crustal pulling apart	<ul style="list-style-type: none"> • Extension (based on topographical profiles) • Intrusion 	Namaquan Wilson Cycle (1.6-1.2Ga)
NW-SE Lineaments	<ul style="list-style-type: none"> • Strike-slip • Cross-cutting Orange River structures • Formed by NE-SW tectonic force • High grade metamorphism • Continued Extension • folding 	Namaqua Orogeny (1.4-1.1Ga)

Table 5-1: Characterisation of the observed structures in Haib area and their corresponding mechanisms and tectonic events based on the structural results from this study, Cornell et al., 2006, Sithole 2013, Macey 2017 and Thomas et al., 1993.

Figure 5-6 shows one possible proposed tectonic model interpretation of the Haib area based on Barr & Reid (1972) and the structural results obtained in this study. Figure 5-6(a) indicates emplacement of the orange river group units (Barr & Reid, 1972), whose starting geology is not fully addressed in this research. In Figure 5-6(b) the compressional stress during the Orange River Orogeny (see Figure 5-1: the study area was on the side) must have created fractures that were strike-slip in the sense of motion as observed from the results in this study (Table 5-1, Cornell et al., 2006; Sithole 2013) but not enough pressure to push the crustal blocks upwards. This continued differential strike-slip formed within crustal blocks generated a weak zone in Figure 5-6(c) (the curved dotted line – along cross-section B above, Figure 5-4) that was followed by intrusions (Barr & Reid, 1972). The amphibolite intrusion seemed to have followed this weaker zone during such intrusions. This weaker zone was enhanced and opened-up during the Namaquan Wilson Cycle extension (red arrows in Figure 5-6(c)) allowing for more magmatic intrusions (Cornell et al., 2006). Subsequently, there was a reactivation of the weaker zones along the intrusion boundaries in the compressional Namaqua Orogenic event that formed the differential stress in the strike-slip faulting system (Macey 2017) in Figure 5-6(d). This model shows that the Haib area was affected by complex tectonic events where more than one tectonic episode is responsible for the faults/lineaments in the area. This proposed tectonic model's interpretation is similar to the theory developed by Mege et al., (2003) of the tectonic forces that act on the area from outside with a differential stress direction as it was the case in this area (Figure 5-1).

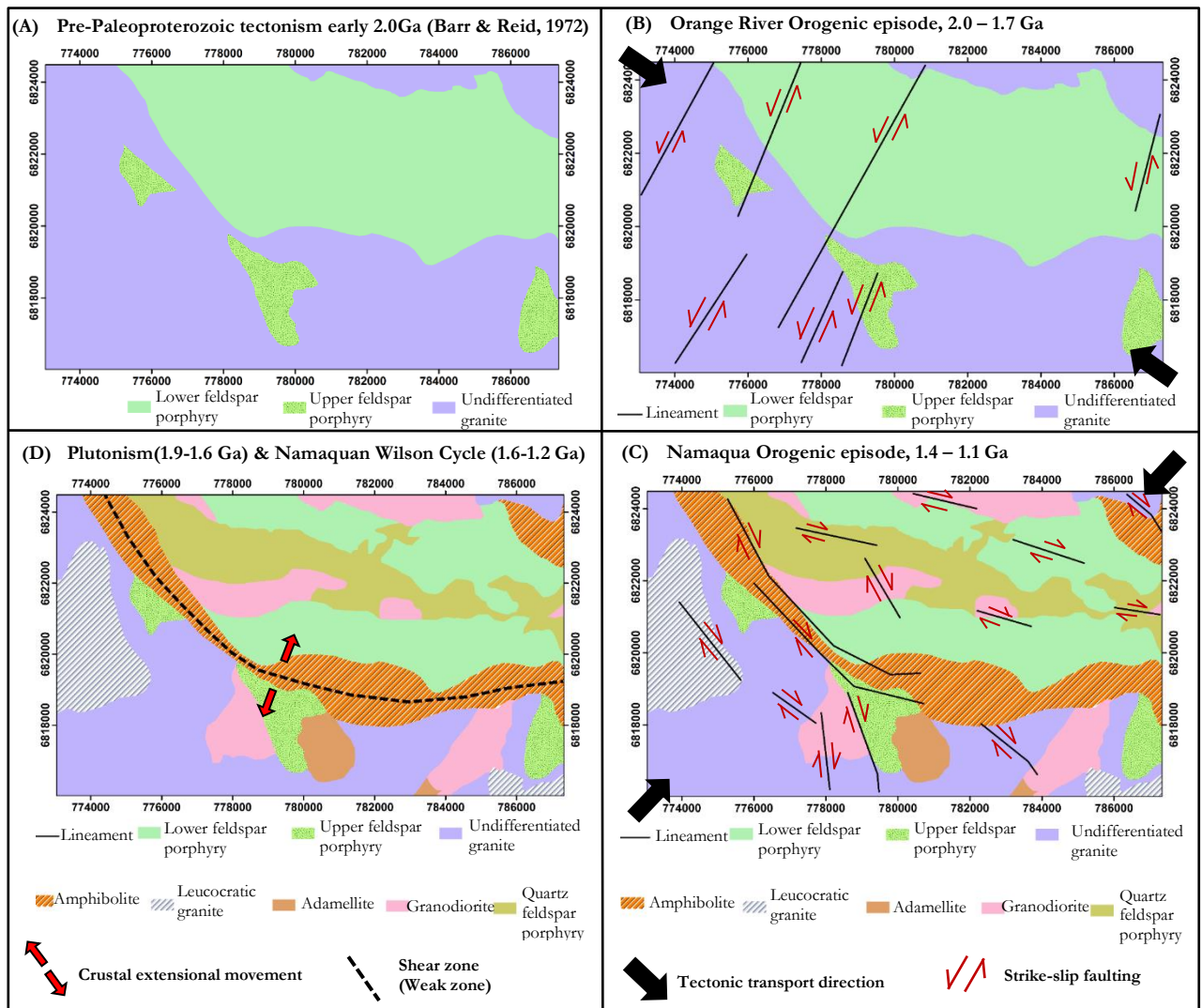


Figure 5-6: Proposed tectonic evolution model sketch of Haib area from 2.0 Ga to 1.1 Ga (a)Shows pre-Paleoproterozoic tectonic state with emplacement of the Orange River Group (b) Paleoproterozoic tectonism of the Orange River Orogeny with NW-SE compression force causing strike-slip faulting (c) Prolonged plutonism and deformation creates a weaker zone and extension in the Namaquan Wilson Cycle that resulted in the intrusion (amphibolite intrusion) and the Violsdrift and Richtersveld Intrusive Suites (d)The Mesoproterozoic compression of the Namaqua Orogeny with NE-SW tectonic force direction causing strike-slip faulting. (Note: the starting geology in (a) is not fully known and based on Barr & Reid 1992)

6. DISCUSSION

6.1. Introduction

This chapter presents a discussion of the results obtained in this research. A total of three components have been addressed in relation to the research objectives and research question presented in chapter one. These components are: (i) similarities and differences of the multispectral ASTER and WorldView-3 automatically extracted lineaments at a local scale in the area, (ii) structural comparison of the ASTER, WorldView-3 and magnetic lineaments kinematics, sense of motion and tectonic implications, and (iii) tectonic evolution and geodynamic modeling of the Haib area.

6.2. Similarities and differences of the ASTER and WorldView-3 extracted lineaments

The analysis of the ASTER and WorldView-3 extracted lineaments showed that the datasets extracted lineaments different despite the similarities in the structural pattern, length, and frequency of the extracted lineaments. The analysis was based on the visual plotting of the length and frequency distribution histograms and the geospatial analysis was based on Rose diagrams orientation, spatial pattern, and distribution of the lineaments.

Analysis and interpretation of lineaments' structural pattern show NW-SE and NE-SW lineament patterns in both datasets. Similarly, length and frequency from both ASTER and WorldView-3 have shown similarities in the highest frequency of the extracted lineaments, frequency distribution, and relatively the same length. This similar result could be due to the general orientation patterns of structural information in the datasets. However, the geospatial analysis performed on the basis of the Rose diagram orientations (Figure 4-5) showed significant differences in the orientation angles of the dominant NW-SE direction and the minor NE-SW direction despite that the datasets were treated equally in the processing and extraction of lineaments. These differences in the orientation angles are very critical for tectonic interpretation of the extracted lineaments. The variations are attributed to several reasons. Firstly, the difference in the lineament extracted could be due to variations in the image solar acquisition angles of ASTER and WorldView-3 imageries. It was noticed that the ASTER and WorldView-3 multispectral data used in this research had different azimuth and elevation solar illumination angles. The ASTER imagery was acquired at an azimuth angle of 81° and an elevation angle of 67° whilst the WorldView-3 imagery was acquired at an azimuth angle of 28° and an elevation angle of 49° . These solar image acquisition properties introduced variations in the image albedo. The difference in the image reflectance is a critical factor in the automatic lineament extraction using the LINE Module algorithm because the algorithm delineates the lineaments from a grey scale 8-bit image with dark and brighter image values. As explained in section 3.5.1 the canny detector in the LINE Module algorithm tests and converts the darker image pixels into zeros (non-edge pixels) and the brighter ones into ones (edges) which are then converted into line segments as lineaments (Green, 2002). The differences in the image albedo due to variations in the solar acquisition angles are evident in the ASTER and WorldView-3 principal component images shown in Figure 4-1. As such the lineaments were extracted differently. Secondly, the difference in the image acquisition seasons as outlined in section 2.5 introduced variations in the images which in turn affected the automatic lineaments extraction process. The ASTER images were acquired in December 2005 which is the rainy and wet season whilst the WorldView-3 images were acquired in April 2018 at the beginning of the winter and dry season in Namibia. These seasonal differences may have affected and influenced the image contents due to varying atmospheric and ground conditions during acquisition. As such, this affected the results of the automatic lineament extraction process. This second reason is directly related to the third reason which is the influence of the vegetational cover in the two images. Even though vegetational analysis showed that there was less vegetational cover in the area during acquisition of both images and that the study area is

generally a semi-arid region, its effect on the automatic lineament extraction cannot be ruled out since vegetation holds water and its alignment affects the lineament extraction process. And lastly, the spectral property differences of the ASTER and WorldView-3 data used in this research may have played a significant role in structural information contained in these two multispectral images. As stated in section 2.5, the ASTER data used in this research was made up of a layer stacked 9 bands Visible Near-Infrared – Shortwave Infrared (VNIR-SWIR) image with the spectral range 0.520 – 2.400 μm . On the other hand, the WorldView-3 imagery was an 8 band Visible Near-Infrared image with spectral range 0.425 – 0.950 μm . This difference offered ASTER imagery a greater spectral wavelength range than WorldView-3, thus the SWIR diagnostic sensitive bands were included within the ASTER principal component processed imagery which was not the case with WorldView-3 imagery. This difference mostly likely introduced differences in the lineament extraction process. The WorldView-3 SWIR images were not used in the research because there was a gap between them in the study area, as provided by DigitalGlobe and were not ideal for use in this case.

6.3. Comparison of ASTER, WorldView-3 and magnetic lineaments kinematics, sense of motion and tectonic implications

The lineaments analysis and interpretation from ASTER, WorldView-3, and magnetic data were done and compared in order to assess if the datasets derived the similar lineaments kinematics and sense of motion. As shown in Figure 4-15, the lineament kinematics indicated that in all the datasets the compression maximum principal force σ_1 (shear fracture) results in linear fracturing and caused an extensional component, the minimum principal force σ_3 at a perpendicular angle to the maximum principal force. This is also observed in the integrated lineament kinematics in Figure 4-18a. This was the case because in the datasets, the extracted lineaments in the NE-SW and NW-SE meant that causative tectonic forces of such lineaments were perpendicular to the lineaments and compressional. Furthermore, the sense of motion from each dataset as shown in Figure 4-12 (ASTER), Figure 4-13 (WorldView-3) and Figure 4-14 (Magnetics) derived similar results dominated by strike-slip faulting, both dextral and sinistral systems. The analysis showed that the NE-SW lineament structures are offset by the NW-SE lineaments structures. This means that the study area was affected by two main tectonic forces that are responsible for the lineament strike-slip deformation in the area. This observation and interpretation were similar to lineaments on the new structural map of the Haib area shown in Figure 4-18. However, comparing the kinematics diagram from all the datasets, the WorldView-3 data is very similar to the magnetics data. This means that WorldView-3 data lineaments represented the subsurface structures better than ASTER data. Magnetic data is robust in subsurface structural mapping since it is not affected by surface distortions (Saada, 2016; Tschirhart et al., 2017).

In summary, this research has revealed that the WorldView-3 multispectral data used in this research better-delineated subsurface lineaments/faults/contacts than the ASTER data and more comparable to magnetic data for this study area. The reason could be because the WorldView-3 imagery was acquired in the dry season and there was no much effect from the atmospheric and ground conditions, as such the automatic lineament extraction was better than in ASTER data. At the same time, WorldView-3 had more bands in the VNIR than ASTER. This may mean that more spectral bands in the WorldView-3 VNIR range were effective in lineament extraction than ASTER VNIR-SWIR combined range. Hence the lineaments kinematics diagram of WorldView-3 and magnetics provided similar tectonic information.

6.4. Tectonic evolution and geodynamics of Haib area

The proposed tectonic evolution and geodynamic model sketches shown in Figure 5-6 showed that the Haib area is characterized by two main structural lineament patterns in the NE-SW and NW-SE directions. It means that NE-SW lineament structures were formed due to the tectonic force direction in the NW-SE direction perpendicular to the lineament directions. Figure 5-6(b) shows that this tectonic force resulted in strike-slip faulting in the area. This means that the tectonic force was compression in nature but was not strong enough to cause the crustal blocks to ride on top of each other, instead, it formed strike-slip linear structures along the weaker zones. This is the case only when the acting forces are not directly on the area as shown in Figure 5-1(a). This is in agreement with the tectonic theory by Mege et al., (2003) of what compressional forces result into when acting from outside the area of interest. The NE-SW lineament structures as shown in Figure 5-2, are offset by the NW-SE lineament structures. This implies that the NE-SW lineaments are older than the NW-SE lineament structures and correspond to the Orange River Orogeny (2.0 – 1.7 Ga). This tectonic event occurred during the Eburnean major tectonic event (Thomas et al., 1993). The NW-SE tectonic force direction is represented by the black arrows A and B in Figure 5-2 and in Figure 5-6(b). On the other hand, the lineament structures that trend in the NW-SE direction means that they were formed by a tectonic force that was perpendicular to these lineaments. As such, they must have been formed by a tectonic force that trended in the NE-SW direction. This tectonic force is represented by the black arrows C and D (NE-SW) in Figure 5-2 and in the tectonic evolution model sketches in Figure 6-5(d). These forces correspond to what Macey et al., (2017) reports as the Namaqua Orogeny (1.4 – 1.1 Ga) during the major Kibaran tectonic event. This tectonic episode is also in agreement to Mege et al., (2003) tectonic theory and resulted in the strike-slip faulting shown in Figure 6-5(d). Based on the offset from the models, it means that NW-SE lineament structures overprinted the NE-SW structures. This interpretation corresponds to the regional separate studies by Barr & Reid (1992) for the Richtersveld Subprovince and Corner (2000) for the whole country of Namibia using magnetic and gravity data.

The 2D tectonic models (Figure 5-3 to Figure 5-5) which were based on the topographic profiles A, B and C in Figure 5-2, indicated some depressions that may be related to the Namaquan Wilson Cycle extension (1.6 – 1.2 Ga). However, these topographic lows may also be linked to the erosional and geomorphological effects in the area. Thus, further research on the possible extension is required. But in the tectonic models A and C, Figure 5-3 and Figure 5-5 respectively, show that the crustal blocks were deformed and compressed in a ductile strike-slip sense during the Orange River Event. This means that strike-slip faulting in the Lower feldspar porphyry in cross-section A and Leucocratic granite in cross-section C were as a result of the tectonic force movement in the NW-SE transport direction, the Orange river Orogeny. Subsequently, in both 2D tectonic models (A and C), the crustal seem to have been pulled apart in the Namaquan Wilson Cycle extension and spreading (1.6 – 1.2 Ga). Later on, the strike-slip faults/lineaments formed during the previous event were reactivated in the Namaqua Orogeny. Further, in the 2D tectonic profile for cross-section B (Figure 5-4), the crustal blocks appear to have been pulled apart in an extensional event which may be related to the Namaquan Wilson Cycle. This most likely created a shear zone (weak spot) shown in Figure 5-6(c) through which the amphibolite unit intruded. Subsequently, the weaker zones were reactivated during the Namaqua Orogeny (compression event) forming the NW-SE strike-slip lineament structures. Therefore, this means that the lineaments structures in the Haib area have been formed by more than one event in a complex tectonic setting. Appendix IX outlines the geochronological summary of the tectonic evolution and geodynamics of the Haib area

7. CONCLUSION AND RECOMMENDATION

7.1. Conclusion

This research presented a proposed tectonic and geodynamic model of the Haib area that led to the formation of its crust between 2.0 to 1.1 billion years ago in the Richtersveld Subprovince within the Namaqua – Natal Province, southern Namibia. The tectonic and geodynamic evidence was derived by integrating lineament structural information from ASTER, Worldview-3, magnetics, topographical and geological data (lithology and geochronology) from literature. The combination of these products and geological information from literature showed that the tectonic and geodynamic activities that led to the emplacement of the study area include magmatism/plutonism, compressional crustal movement, intrusion and Namaquan Wilson Cycle extension.

The research applied two approaches: Firstly, geological structural lineaments extracted automatically from multispectral ASTER and WorldView-3 and magnetic data were compared in terms of their kinematics and sense of motion. Secondly, lineaments from these datasets were integrated to produce a composite structural map of the area for a better understanding of the tectonics and geodynamics of the Haib area. New structural information was added on the previously published geological map of the Haib by Blignault, (1972) to improve our understanding of tectonic activities in the area.

The research has been able to answer the questions that were put forth in chapter one in the attempt to address the objectives and solve the research problem that led to the motivation of this work. The answers to these questions are presented below.

1. How comparable are WorldView-3 and ASTER datasets in extracting geological linear structural features in terms of spatial distribution pattern, orientation, length, and frequency?

- **Lineaments spatial distribution pattern** – The ASTER and WorldView-3 datasets extracted lineament maps that showed similar patterns and distribution in the study area. Both datasets showed that most lineaments were concentrated on the western part of the area with a dominant pattern in the NW-SE and minor pattern in the NE-SW directions. However, the datasets did not extract lineaments from the same exact spatial locations. In some areas, WorldView-3 extracted lineaments in areas where ASTER did not and vice versa. The spatial difference in meters of the lineaments extracted from ASTER and WorldView-3 data ranges between 70 to 100 meters.
- **Lineaments orientation pattern** – The lineaments orientation pattern on the Rose diagrams for ASTER and WorldView-3 data were not the same in the orientation angles. In the NW-SE dominant orientation, ASTER data was between 330° - 340° and WorldView-3 data was between 290° - 300° in the same direction. And the minor direction ASTER was more in the NNE-SSE at 0° - 30° , while WorldView-3 was well pronounced in the NE-SW at 20° - 35° .
- **Lineaments length and frequency** – Both ASTER and WorldView-3 datasets showed a similar frequency distribution pattern with more lineaments between 700-1000 meters for both datasets. However, WorldView-3 data extracted more and longer lineaments. The longest length in WorldView-3 data was 3.5 kilometers while in the ASTER data the longest length was 3.31 kilometers. Therefore, the datasets extracted the lineaments differently.

2. Does each of ASTER, WorldView-3, and aeromagnetic data derive lineaments sense of motion and relative age of the main deformational tectonic episodes?

All the datasets derived the strike-slip lineament sense of motion and supported the same relative ages of the two main deformational tectonic episodes. Individual lineament analysis of ASTER, WorldView-3, and aeromagnetic data indicated that the area was affected by two tectonic events that caused strike-slip faulting (both sinistral and dextral systems). The analysis further showed that the NE-SW lineaments were caused by the older event which was the Orange River Orogeny whose tectonic force direction was in the NW-SE and the NW-SE lineaments were caused by a younger event, the Namaqua Orogeny that overprinted the earlier event.

3. What improvement does the integration of ASTER, WorldView-3, and Aeromagnetic data have on our understanding of the structures and tectonics of the Haib area? Are there new structures identified compared to the published structural map by Blignault (1972)?

The integrated approach delineated more lineament structures in the study area than the previously published structural map by Blignault (1972). This integrated lineament structural map provided an enhanced understanding of the structural and tectonic activities in the area. These results show that the study area has undergone multiple and complex neotectonics events, with the main deformational phases in the NW-SE and NE-SW directions.

4. Can the delineated lineament structures in the study area be linked with the tectonic events that have affected the area?

This research work delineated two main lineaments pattern structures: The NE-SW and NW-SE lineament structural patterns. Both patterns were characterized by strike-slip faulting, folding and thrusting. The NE-SW orientation pattern was associated with the older tectonic event, the Orange River Orogeny between 2.0 to 1.7 billion years ago, which was part of the major Eburnean event (Collision and amalgamation of the San Francisco and Congo Cratons). The NW-SE dominant lineament orientation pattern was associated with the younger event, the Namaqua Orogeny between 1.4 to 1.1 billion years ago, which was part of the major Kibaran event that involved collision and amalgamation of the Namaqualand and Zimbabwe-Kaapvaal Cratons.

5. Is it possible to derive the tectonic evolution and geodynamic model of the study area in relation to the tectonic events?

The tectonic compressional events (Orange River and Namaqua Orogeny) and the Namaquan Wilson Cycle extensions led to the crustal movement in the area. These extensional and compressional strike-slip crustal movements which were related to the plutonic intrusions and possible rifting made it possible to derive a proposed tectonic evolution and geodynamic processes of the Haib area in relation to these events.

7.2. Recommendation

The author suggests the following recommendations in order to improve the results and tectonic framework interpretation in the Haib area for further research studies.

- 1) The automatic lineament extraction LINE Module algorithm in PCI Geomatica which uses Canny Edge detector has mostly been used on Digital Elevation Models and Radar data. But this research has further shown that the algorithm can effectively be applied to multispectral ASTER and WorldView-3 data. However, the algorithm uses extraction parameters that depend on the spatial and spectral resolution of the input data. Therefore, a sensitivity analysis of optimal multispectral data specifications (spatial resolution in particular) is needed to determine its effect in geological lineament extraction.
- 2) An assessment of the seasonal effects of multispectral satellite (ASTER and WorldView-3) data on geological lineaments automatic extraction needs to be further investigated to assess variability in structural information that can be extracted between seasons. This was not possible in this research because of the lack of seasonal data for both datasets.
- 3) Fieldwork as a follow up on the geological structural lineaments delineated in this study. Since there was no fieldwork in this research, it was not possible to validate and classify the type of lineaments that were automatically extracted from the datasets. Thus, ground truthing of these lineaments is recommended. In addition, the mapped ASTER Band ratio products in this research were not validated by Analytical Spectral Device (ASD) FieldSpec spectroradiometer measurements, as such field checks are highly recommended for further research.
- 4) Determination of the age of the lithologies in the study area using up-to-date isotopic dating techniques to constrain the much longer tectonic evolution time-span and ages of the lithological units and use it for further tectonic evolution interpretation.
- 5) Need for 3D geological structural modeling to determine the structural depth extent in relation to the lithological units in the area
- 6) Analyzing the drill core data in the Haib area to determine the geology and mineralogy at various depth in relation to the 3D geological modeling recommended in 6) above.

LIST OF REFERENCES

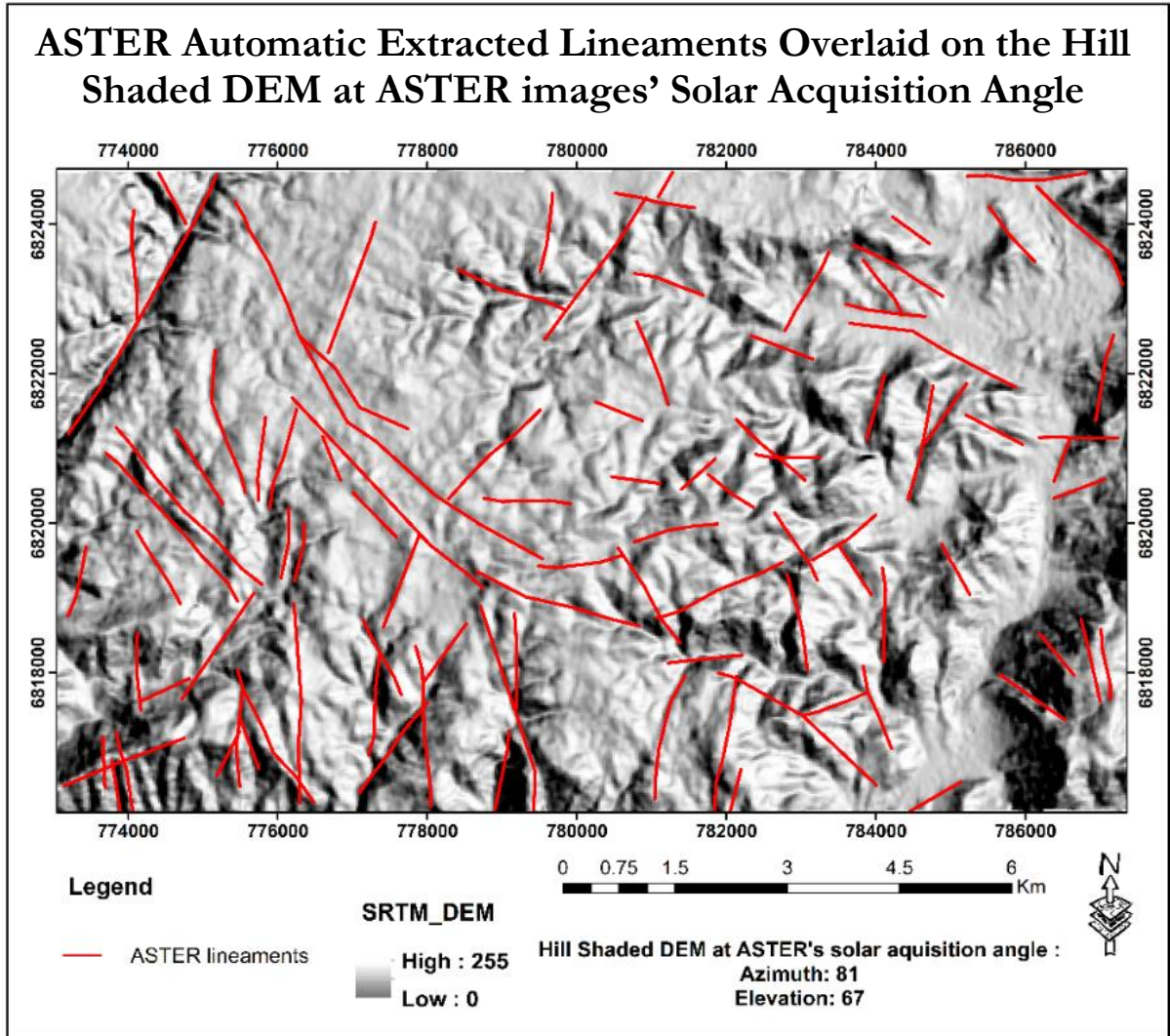
- Adegboyega, P. (2016). Characterisation of the Haib porphyry copper deposit, southern Namibia, using hyperspectral and radiometric datasets. MSc Thesis, Faculty of Geo-Information Science and Earth Observation (ITC), University of Twente. Retrieved from <https://webapps.itc.utwente.nl/library/2016/msc/aes/adeparioye.pdf>
- Adiri, Z., El Harti, A., Jellouli, A., Lhissou, R., Maacha, L., Azmi, M., ... Bachaoui, E. M. (2017). Comparison of Landsat-8, ASTER, and Sentinel 1 satellite remote sensing data in automatic lineaments extraction: A case study of Sidi Flah-Bouskour inlier, Moroccan Anti Atlas. *Advances in Space Research*, 60(11), 2355–2367. <https://doi.org/10.1016/j.asr.2017.09.006>
- Adiri, Z., El Harti, A., Jellouli, A., Maacha, L., & Bachaoui, E. M. (2016). Lithological mapping using Landsat 8 OLI and Terra ASTER multispectral data in the Bas Drâa inlier, Moroccan Anti Atlas. *Journal of Applied Remote Sensing*, 10(2), 025013. <https://doi.org/10.1117/1.JRS.10>
- Akinlalu, A. A., Adelusi, A. O., Olayanju, G. M., Adiat, K. A. N., Omosuyi, G. O., Anifowose, A. Y. B., & Akeredolu, B. E. (2018). Aeromagnetic mapping of basement structures and mineralisation characterisation of Ilesa Schist Belt, Southwestern Nigeria. *Journal of African Earth Sciences*, 138, 383–391. <https://doi.org/10.1016/j.jafrearsci.2017.11.033>
- Almasi, A., Jafarirad, A., Kheyrollahi, H., Rahimi, M., & Afzal, P. (2014). Evaluation of structural and geological factors in orogenic gold type mineralisation in the Kervian area, north-west Iran, using airborne geophysical data. *Exploration Geophysics*, 45(4), 261. <https://doi.org/10.1071/EG13053>
- Anhaeusser, C. R. (1990). Precambrian crustal evolution and metallogeny of southern Africa. *Developments in Precambrian Geology*, 8(C), 123–156. [https://doi.org/10.1016/S0166-2635\(08\)70165-8](https://doi.org/10.1016/S0166-2635(08)70165-8)
- Argialas, D., Mavrantza, O., & Stefouli, M. (2003). Automatic mapping of tectonic lineaments (faults) using methods and techniques of photointerpretation/digital remote sensing and expert Systems. *THALES Project*, (1174). Retrieved from http://www.ntua.gr/eiseve/Vasikh_Ereyna/Thalis/Thalis_projects_English_summaries/Argialas.pdf
- Asadzadeh, S., Roberto, C., & Filho, D. S. (2016). A review on spectral processing methods for geological remote sensing. *International Journal of Applied Earth Observations and Geoinformation*, 47, 69–90. <https://doi.org/10.1016/j.jag.2015.12.004>
- Bahiru, E. A., & Woldai, T. (2016). Integrated geological mapping approach and gold mineralization in Buhweju area, Uganda. *Ore Geology Reviews*, 72, 777–793. <https://doi.org/10.1016/j.oregeorev.2015.09.010>
- Barr, J. M., & Reid, D. L. (1992). Hydrothermal alteration at the Haib porphyry copper deposit, Namibia: Stable isotope and fluid inclusion patterns. *Communs Geol. Surv. Namibia*, 8, 23–35.
- Begg, G. C., Natapov, L. M., Reilly, S. Y. O., Neill, C. J. O., & Bowden, P. (2009). The lithospheric architecture of Africa : Seismic tomography, mantle petrology, and tectonic evolution. *Geosphere*, 5(1), 23–50. <https://doi.org/10.1130/GES00179.1>
- Blignault, H. J. (1972). Geological Map of Haib area. *Geological Survey of Namibia*. Windhoek.
- Blignault, H. J. (1977). Structural-metamorphic imprint on part of the Namaqua mobile belt in South West Africa. The University of Cape Town.
- Chaabouni, R., Bouaziz, S., Peresson, H., & Wolfgang, J. (2012). Lineament analysis of South Jenein Area (Southern Tunisia) using remote sensing data and geographic information system. *The Egyptian Journal of Remote Sensing and Space Science*, 15(2), 197–206. <https://doi.org/10.1016/j.ejrs.2012.11.001>
- Chao, M. A., Zeng-zhang, G. U. O., Xiao-ke, Z., & Rui-mei, H. A. N. (2011). Annual integral changes of time serial NDVI in mining subsidence area. *Transactions of Nonferrous Metals Society of China*, 21, 583–588. [https://doi.org/10.1016/S1003-6326\(12\)61644-6](https://doi.org/10.1016/S1003-6326(12)61644-6)
- Chernicoff, C. J., Richards, J. P., & Zappettini, E. O. (2002). Crustal lineament control on magmatism and mineralization in northwestern Argentina: Geological, geophysical, and remote sensing evidence. *Ore Geology Reviews*, 21, 127–155.
- Chisenga, C. (2015). Understanding the earth structure underneath Botswana: The tectonic model and its relationship to the basement and crustal thickness. MSc Thesis, Faculty of Geo-Information Science and Earth Observation (ITC), University of Twente. <https://doi.org/10.13140/RG.2.2.35406.46404>

- Chisenga, C., Dulanya, Z., & Jianguo, Y. (2018). The structural re-interpretation of the Lower Shire Basin in the Southern Malawi rift using gravity data. *Journal of African Earth Sciences*, 149(September), 280–290. <https://doi.org/10.1016/j.jafrearsci.2018.08.013>
- Colliston, W. P., & Schoch, A. E. (2000). Mid-Proterozoic tectonic evolution along the Orange River on the border between South Africa and Namibia. *Communs Geol. Surv. Namibia*, 12, 57–66. <https://doi.org/10.1079/PAVSNR201510031>
- Connelly, D., Walker, P. & Richards, D. (2018). Haib copper project 2018 preliminary economic assessment. *Mineral Engineering Technical Services (METS) A division of the Midas Engineering Group*. Vancouver; Canada. Retrieved from www.deepsouthresources.com/wp-content/uploads/Haib_Copper_Project_2018_Preliminary_Economic_Assessment.pdf
- Cooper, G. R. J., & Cowan, D. R. (2006). Enhancing potential field data using filters based on the local phase. *Comput. Geosci*, 32, 1585–1591. <https://doi.org/10.1016/j.cageo.2006.02.016>
- Cooper, G. R. J., & Cowan, D. R. (2008). Edge enhancement of potential-field data using normalized statistics. *GEOPHYSICS*, 73(3), H1–H4. <https://doi.org/10.1190/1.2837309>
- Cornell, D. H., Thomas, R. J., Moen, H. F. G., Reid, D. L., Moore, J. M., & Gibson, R. L. (2006). The Namaqua-Natal Province. *The Geology of South Africa. Geological Society of South Africa, Johannesburg/ Council for Geoscience, Pretoria*, 325–379.
- Corner, B. (2000). Crustal framework of Namibia derived from magnetic and gravity data. *Commun. Geol. Surv. Namib*, (12), 15–22. Retrieved from <http://www.nature.com/articles/467272a>
- Csillag, F., & Stogicza, A. (1987). Application of Satellite Imagery in Tectonic Interpretation. *Journal of Geodynamics*, 8, 205–219.
- Cudahy, T. (2012). Satellite ASTER Geoscience Product Notes Western Australia, 2(Version 1), 1–23.
- Davies, C. J., & Coward, M. P. (1982). The Structural Evolution of the Gariep Arc in Southern. *Precambrian Research* 17, 173–198.
- Eberle, D., Andritzky, G., & Wackerle, R. (1995). The new magnetic data set of Namibia: Its contributions to the understanding of crustal evolution and regional distribution of mineralization. *Commun. Geol. Surv. Namib*, 10, 143–152.
- Eglinton, B. M. (2006). Evolution of the Namaqua-Natal Belt, southern Africa – A geochronological and isotope geochemical review. *Journal of African Earth Sciences* 46, 93–111. <https://doi.org/10.1016/j.jafrearsci.2006.01.014>
- Eldosouky, A. M., Abdelkareem, M., & Elkhateeb, S. O. (2017). Integration of remote sensing and aeromagnetic data for mapping structural features and hydrothermal alteration zones in Wadi Allaqi area, South Eastern Desert of Egypt. *Journal of African Earth Sciences*, 130, 28–37. <https://doi.org/10.1016/j.jafrearsci.2017.03.006>
- Fransson, M. (2008). A geochemical investigation of metabasites from Kakamas and Bushmanland Terranes, Namaqua Province, South Africa. MSc thesis, Department of Earth Science, Geology, University of Gothenburg.
- Green, B. (2002). Canny Edge Detection Tutorial. Retrieved November 15, 2018, from <http://masters.donntu.org/2010/fknt/chudovskaja/library/article5.htm>
- Hashim, M., Ahmad, S., Johari, M. A. M., & Pour, A. B. (2013). Automatic lineament extraction in a heavily vegetated region using Landsat Enhanced Thematic Mapper (ETM+) imagery. *Advances in Space Research*, 51(5), 874–890. <https://doi.org/10.1016/j.asr.2012.10.004>
- Hung, L. Q., Batelaan, O., & De Smedt, F. (2005). Lineament extraction and analysis, comparison of LANDSAT ETM and ASTER imagery. Case study: Suoimuoi tropical karst catchment, Vietnam, 5983, 59830T. <https://doi.org/10.1117/12.627699>
- Indongo, L. J. (2017). The Lithological and Structural Characterisation of the Sperlingputs Shear Zone in Southern Namibia. (MSc Thesis), Stellenbosch University, 2017. Retrieved from <http://scholar.sun.ac.za/handle/10019.1/102936>
- Jacobs, J., Pisarevsky, S., Thomas, R. J., & Becker, T. (2008). The Kalahari Craton during the assembly and dispersal of Rodinia. *Precambrian Research*, 160, 142–158. <https://doi.org/10.1016/j.precamres.2007.04.022>
- Kruse, F. A. (2014). Comparison of ATREM, ACORN, and FLAASH atmospheric corrections using low-altitude AVIRIS data of Boulder, CO. *Geoimaging, Horizon*.

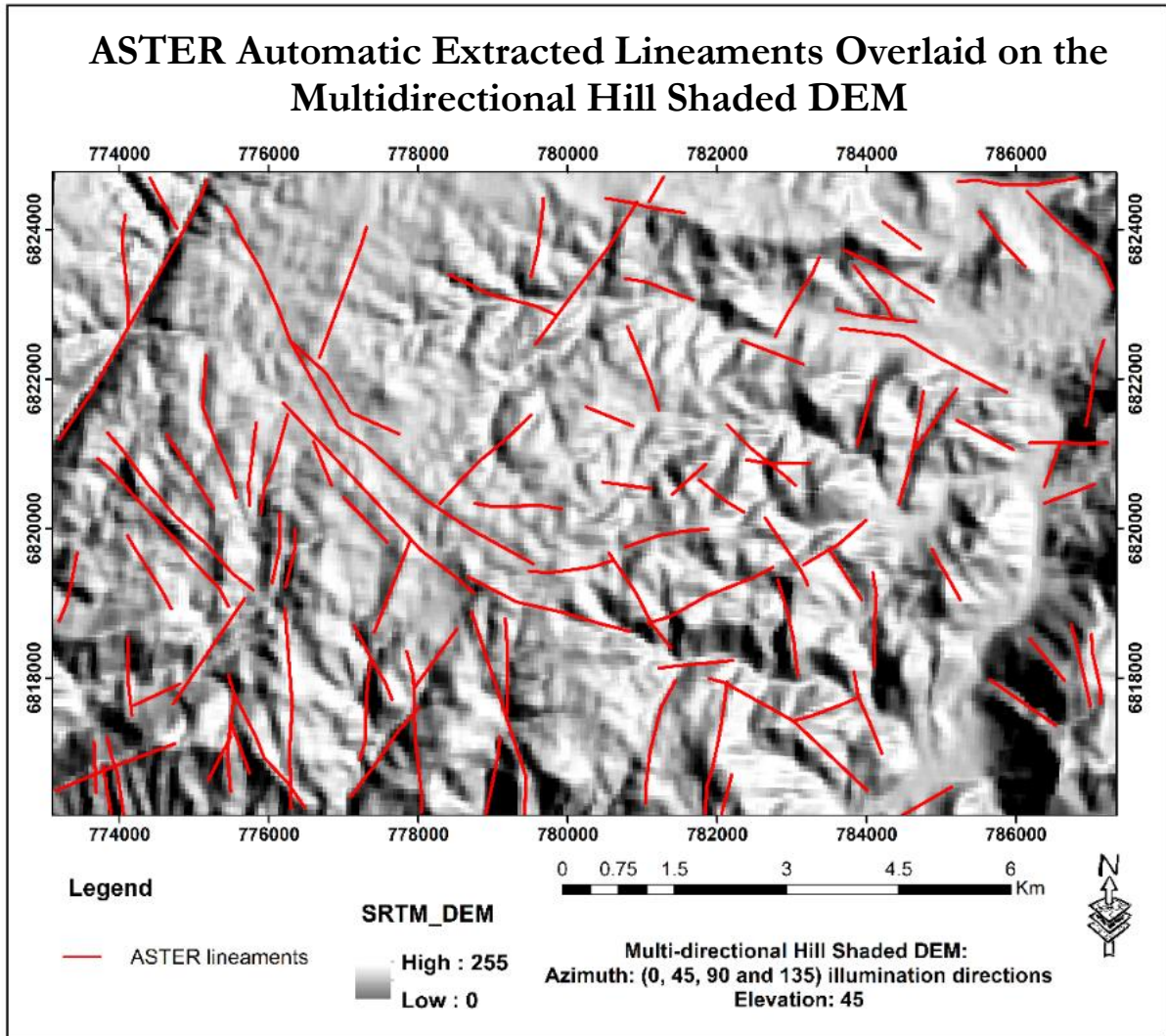
- Langford, R. L. (2015). Temporal merging of remote sensing data to enhance spectral regolith, lithological and alteration patterns for regional mineral exploration. *Ore Geology Reviews*, 68, 14–29. <https://doi.org/10.1016/j.oregeorev.2015.01.005>
- Li, N. (2010). Textural and Rule-based Lithological Classification of Remote Sensing Data, and Geological Mapping in Southwestern Prieska Sub-basin, Transvaal Supergroup, South Africa. (PhD Thesis), Faculty of Earth Sciences, The Ludwig Maximilian University of Munich, Germany. Retrieved from <https://pdfs.semanticscholar.org/9773/ff30ba6a0dc9598315a2ae12a42920b870fe.pdf>
- Liu, J., Chen, L., Li, W., Wang, G., & Xiao, X. (2018). Application of Multi-source Data on Structural Framework Study in the Western Beishan Orogenic Belt, Northwest China. *China Aero Geophysical Survey and Remote Sensing Center*, 7438–7441.
- Ma, G., & Li, L. (2012). Edge detection in potential fields with the normalized total horizontal derivative. *Computers and Geosciences*, 41, 83–87. <https://doi.org/10.1016/j.cageo.2011.08.016>
- Macey, P. H., Thomas, R. J., Minnaar, H. M., Gresse, P. G., Lambert, C. W., Groenewald, C. A., ... Tinguely, C. (2017). Origin and evolution of the ~1.9 Ga Richtersveld Magmatic Arc, SW Africa. *Precambrian Research*, 292, 417–451. <https://doi.org/10.1016/j.precamres.2017.01.013>
- Malik, A., I, G., UA, D., & H, H. (2018). Delineation and Correlation of Lineaments Using Landsat-7 ETM+, DEM, and Aeromagnetic Datasets: Basement Complex of Shanono, Northwestern Nigeria. *Journal of Geology & Geophysics*, 07(04). <https://doi.org/10.4172/2381-8719.1000445>
- Marghany, M., & Hashim, M. (2010). Lineament mapping using multispectral remote sensing satellite data. *Int. J. Phys. Sci.*, (5), 1501–1507.
- Mdala, H. (2015). Determining Structural variations between the Northern and Southern provinces of the Malawi Rift by using automatic lineament extraction methods. MSc Thesis, Faculty of Geo-Information Science and Earth Observation (ITC), University of Twente. Retrieved from <https://webapps.itc.utwente.nl/library/2015/msc/aes/mdala.pdf>
- Mege, D., Cook, A. C., Garel, E., Lagabrielle, Y., & Orbiter, V. (2003). Volcanic rifting at Martian grabens. *Journal of Geophysics Research*, 108(5), 1–33. <https://doi.org/10.1029/2002JE001852>
- Meshkani, S. A., Mehrabi, B., Yaghubpur, A., & Sadeghi, M. (2013). Recognition of the regional lineaments of Iran: Using geospatial data and their implications for exploration of metallic ore deposits. *Ore Geology Reviews*, 55(C), 48–63. <https://doi.org/10.1016/j.oregeorev.2013.04.007>
- Miller, H. G., & Singh, V. (1994). Potential field tilt—a new concept for location of potential field sources. *Journal of Applied Geophysics*, 32(2–3), 213–217. [https://doi.org/10.1016/0926-9851\(94\)90022-1](https://doi.org/10.1016/0926-9851(94)90022-1)
- Minnitt, R. C. (1986). Porphyry copper-molybdenum mineralization at Haib River, South West Africa/Namibia. *Geological Society of South Africa, Johannesburg*.
- Muhammad, M., & Awdal, A. (2012). Automatic mapping of lineaments using shaded relief images derived from digital elevation model (DEM) in Erbil-Kurdistan, northeast Iraq Automatic Mapping of Lineaments Using Shaded Relief Images Derived from Digital. *Advances in Natural and Applied Sciences*, 2(January), 138–146.
- Mustard, J. F., & Sunshine, J. M. (1999). 5 Spectral analysis for Earth Science: Investigations using remote sensing data. In *Remote Sensing for Earth Sciences*. (Vol. 3). John Wiley & Sons, Inc. Retrieved from http://www.geo.brown.edu/research/Milliken/GEOL1710_files/Mustard_ManualOfRemoteSensing_Ch5.pdf
- Ngcofe, L., Minnaar, H., & Halenyane, K. (2013). Multispectral and hyperspectral remote sensing: target area generation for porphyry copper exploration in the Namaqua metamorphic province, South Africa. *Geological Society of South Africa*, 116(June), 259–272. <https://doi.org/10.2113/gssajg.116.2>
- Niccoli, M. (2015). Mapping and validating lineaments. *The Leading Edge*, 34(8), 948–950. <https://doi.org/10.1190/tle34080948.1>
- Nugroho, U. C., & Tjahjaningsih, A. (2016). Lineament density information extraction using Dem. *International Journal of Remote Sensing and Earth Sciences*, 13(1), 67–74.
- Paganelli, F., Grunsky, E. C., Richards, J. P., & Pryde, R. (2003). Use of RADARSAT-1 principal component imagery for structural mapping: a case study in the Buffalo Head Hills area, northern central Alberta, Canada. *Canadian Journal of Remote Sensing*, 29(1), 111–140. <https://doi.org/10.5589/m02-084>
- Pilkington, M., & Keating, P. (2004). Contact mapping from gridded magnetic data - a comparison of techniques. *Exploration Geophysics*, 35(4), 306–311. <https://doi.org/10.1071/EG04306>

- Porwal, A., John, E., Carranza, M., & Hale, M. (2006). Tectonostratigraphy and base-metal mineralization controls, Aravalli province (western India): New interpretations from geophysical data analysis. *Ore Geology Reviews*, 29, 287–306. <https://doi.org/10.1016/j.oregeorev.2005.10.003>
- Ranganai, R. T., & Ebinger, C. J. (2008). Aeromagnetic and Landsat TM structural interpretation for identifying regional groundwater exploration targets, south-central Zimbabwe Craton. *Journal of Applied Geophysics*, 65(2), 73–83. <https://doi.org/10.1016/j.jappgeo.2008.05.009>
- Reid, D. L., Ransome, I. G. D., Onstott, T. C., & Adams, C. J. (1991). Time of emplacement and metamorphism of Late Precambrian mafic dykes associated with the Pan-African Gariiep orogeny, Southern Africa: implications for the age of the Nama Group. *Journal of African Earth Sciences (and the Middle East)*, 13(3–4), 531–541. [https://doi.org/10.1016/0899-5362\(91\)90116-G](https://doi.org/10.1016/0899-5362(91)90116-G)
- Saada, S. A. (2016). Edge detection and depth estimation of Galala El Bahariya Plateau, Eastern Desert-Egypt, from aeromagnetic data. *Geomechanics and Geophysics for Geo-Energy and Geo-Resources*, 2(1), 25–41. <https://doi.org/10.1007/s40948-015-0019-6>
- Sandrin, A. (2006). Geophysical and petrophysical study of an iron oxide copper-gold deposit in northern Sweden. *Ore Geology Reviews*, 29, 1–18. <https://doi.org/10.1016/j.oregeorev.2005.06.001>
- Schijndel, V. Van. (2013). Precambrian crustal evolution of the Rehoboth Province, Southern Africa. PhD Thesis, Faculty of Science, University of Gothenburg, Sweden.
- Sithole, N. (2013). A study into the main structural features of the Namaqua region and their relation to the intrusion of the Keimoes Suite. MSc Thesis, Department of Earth Sciences (University of the Western Cape). Retrieved from http://etd.uwc.ac.za/xmlui/bitstream/11394/3877/1/SITHOLE_MSC_2013.pdf
- Sukumar, M., & Nelson, C. (2017). Performance evaluation of lineament extraction methods in ASTER satellite images. *International Journal of Oceans and Oceanography*, 11(2), 249–263. Retrieved from <http://www.ripublication.com>
- Tarback, E. J., Lutgens, F. K., & Tasa, D. G. (2017). *Earth: An Introduction to Physical Geology* (12th Ed.). Pearson.
- Teck Cominco Namibia Ltd. (2009). Renewal Report: Exclusive Prospecting Licence 3140. Retrieved from https://www.deepsouthresources.com/wp-content/uploads/Haib_NI43-101_May-3-2016_FINAL.pdf
- Thomas, B., & Cornell, D. H. (1994). The Kibaran of southern Africa: Tectonic evolution and metallogeny The Kibaran of southern Africa: Tectonic evolution and metallogeny. *Ore Geology Reviews*, 1368(93), 131–160. [https://doi.org/10.1016/0169-1368\(94\)90025-6](https://doi.org/10.1016/0169-1368(94)90025-6)
- Thomas, R. J., von Veh, M. W., & McCourt, S. (1993). The tectonic evolution of southern Africa: an overview. *Journal of African Earth Sciences*, 16(1–2), 5–24. [https://doi.org/10.1016/0899-5362\(93\)90159-N](https://doi.org/10.1016/0899-5362(93)90159-N)
- Tschirhart, V., Jefferson, C. W., & Morris, W. A. (2017). Basement geology beneath the northeast Thelon Basin, Nunavut: insights from integrating new gravity, magnetic and geological data. *Geophysical Prospecting*, 65(2), 617–636. <https://doi.org/10.1111/1365-2478.12430>
- van der Meer, F. (2004). Analysis of spectral absorption features in hyperspectral imagery. *International Journal of Applied Earth Observation and Geoinformation*, 5, 55–68. <https://doi.org/10.1016/j.jag.2003.09.001>
- Verduzco, B., Fairhead, J. D., Green, C. M., & MacKenzie, C. (2004). New insights into magnetic derivatives for structural mapping. *The Leading Edge*, 23(2), 116–119. <https://doi.org/10.1190/1.1651454>
- Yeomans, C. M., Middleton, M., Shail, R. K., Grebby, S., & Lusty, P. A. J. (2018). Integrated Object-Based Image Analysis for semi-automated geological lineament detection in Southwest England. *Computers & Geosciences*, [In Review]. <https://doi.org/10.1016/j.cageo.2018.11.005>
- Zhumabek, Z., Assylkhan, B., Alexandr, F., Dinara, T., & Altynay, K. (2017). Automated lineament analysis to assess the geodynamic activity areas. *Procedia Computer Science*, 121, 699–706. <https://doi.org/10.1016/j.procs.2017.11.091>

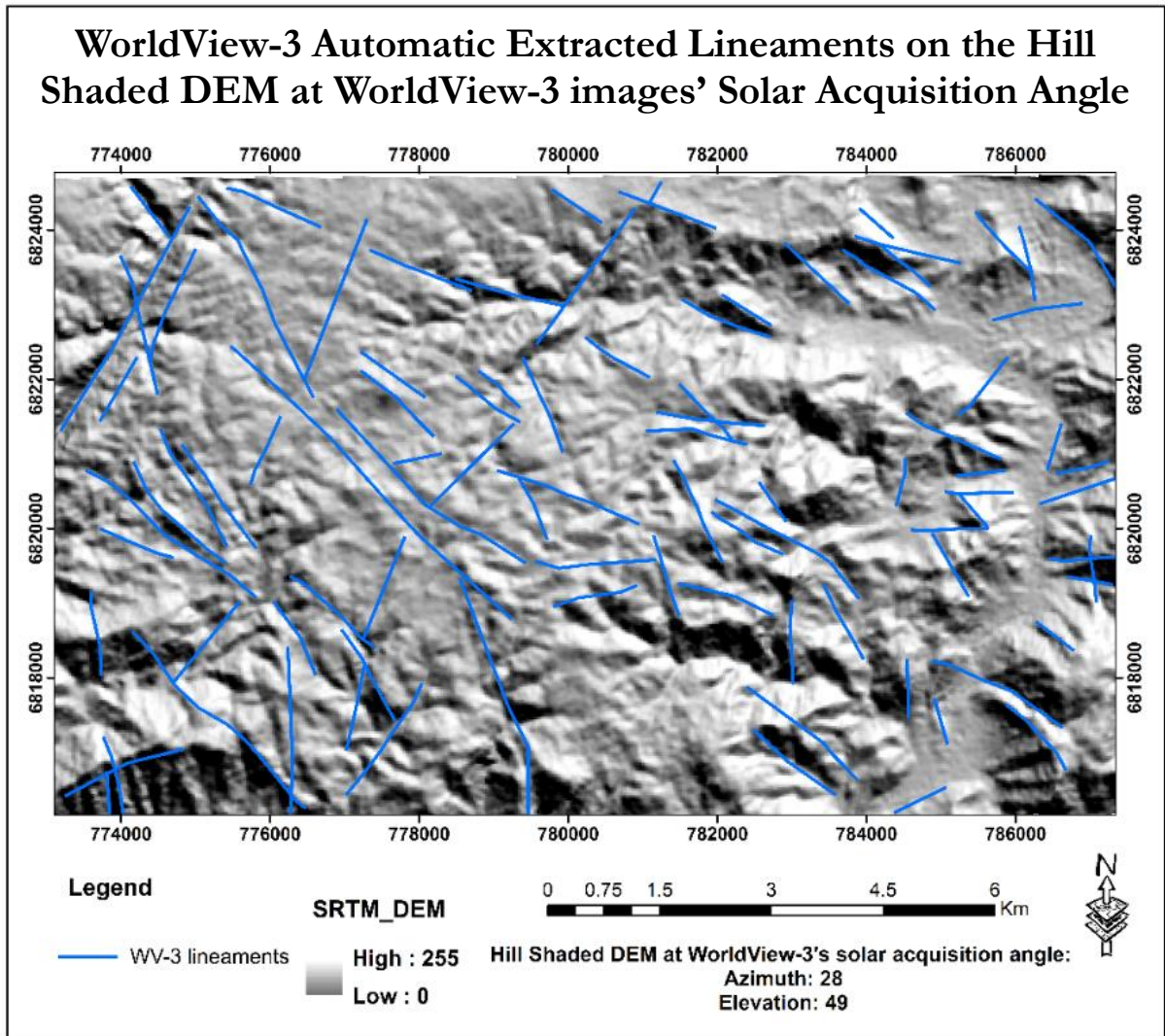
APPENDIX I: LINEAMENTS OVERLAID ON DEMS



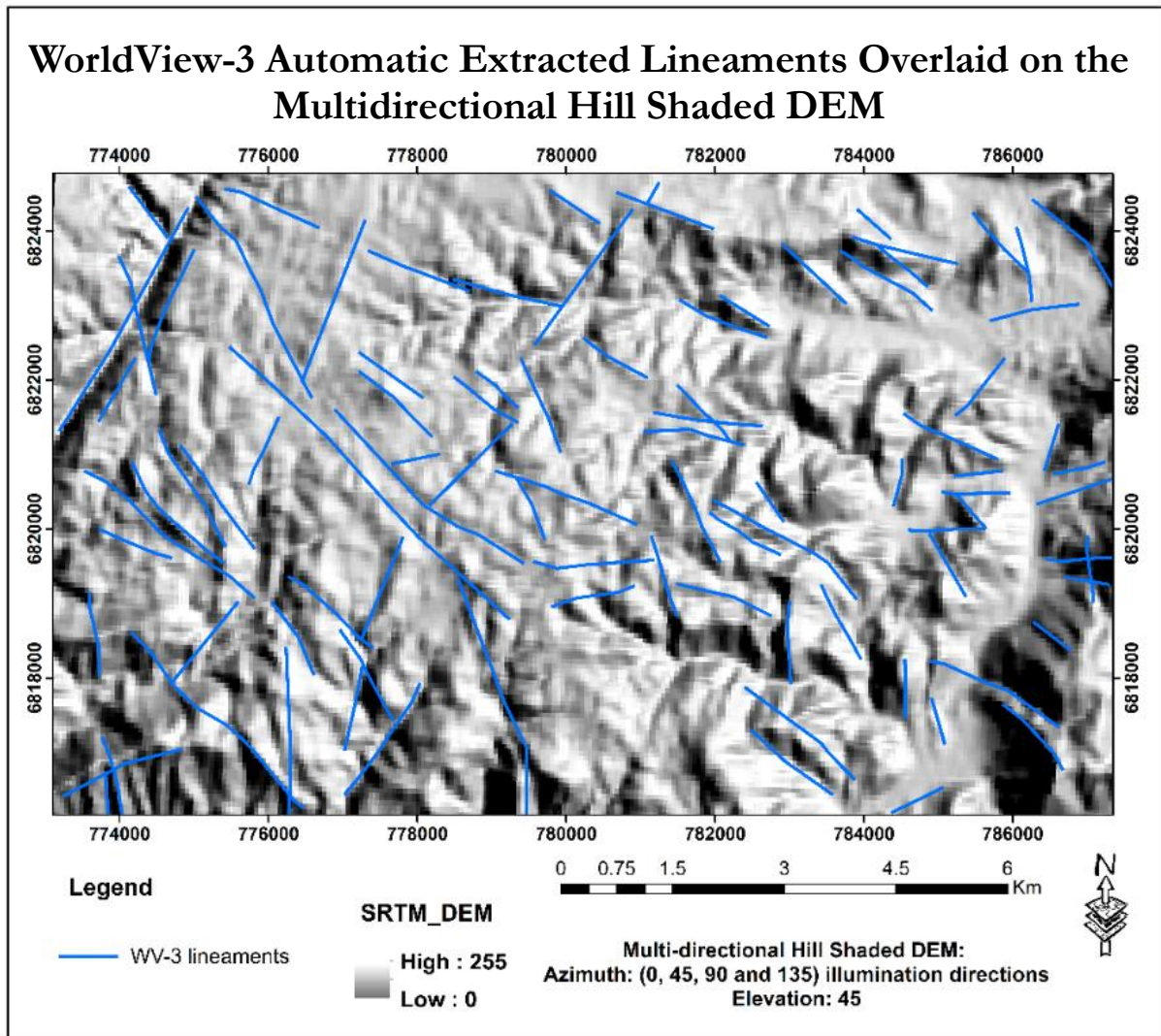
APPENDIX I: LINEAMENTS OVERLAID ON DEMS



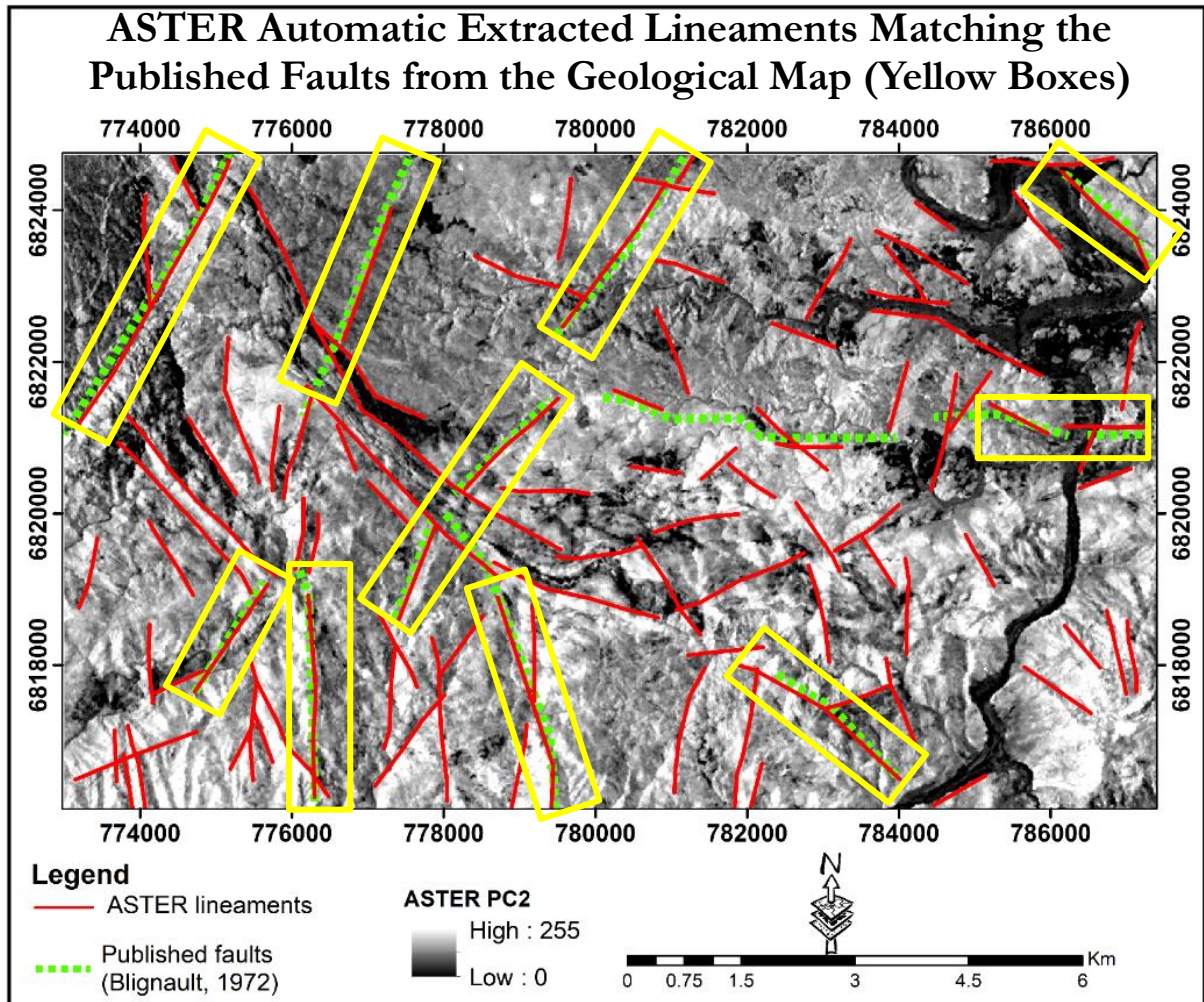
APPENDIX I: LINEAMENTS OVERLAID ON DEMS



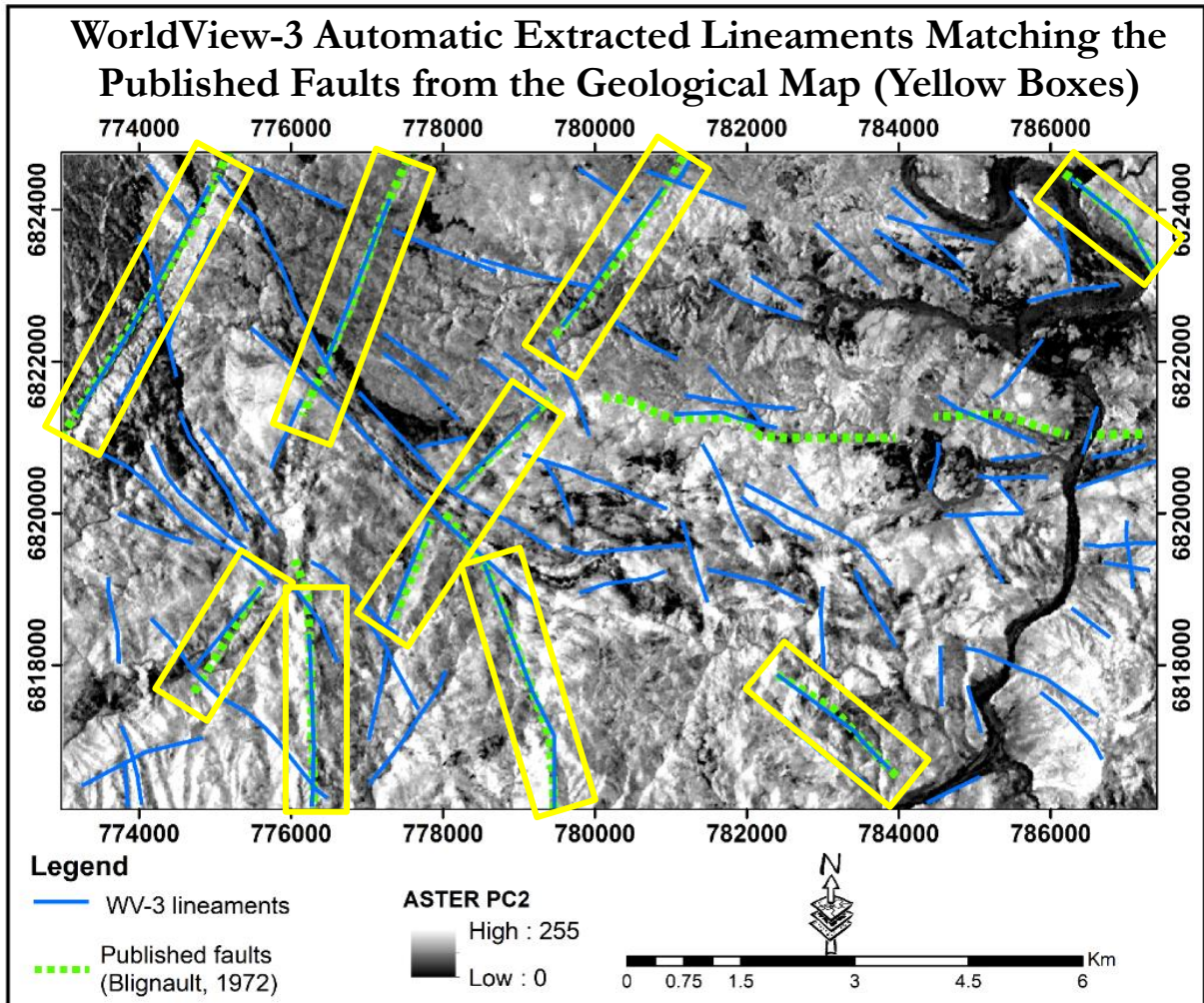
APPENDIX I: LINEAMENTS OVERLAID ON DEMS



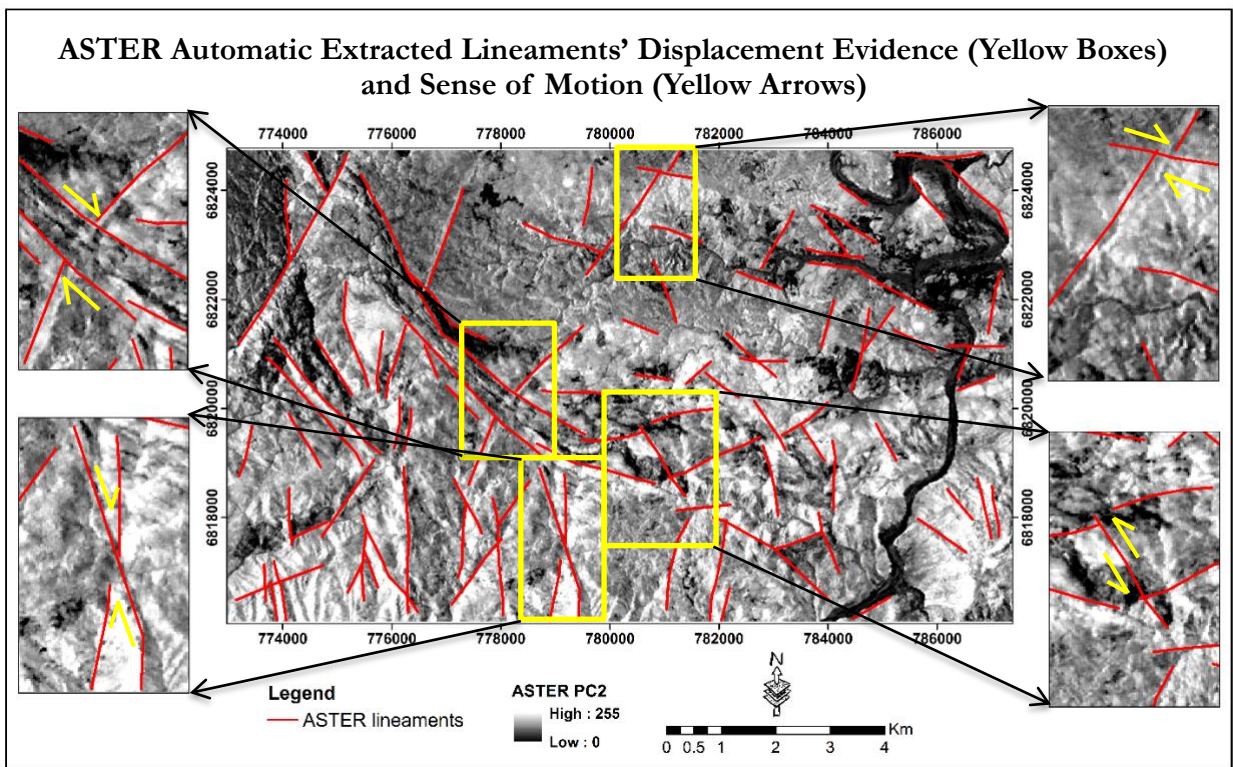
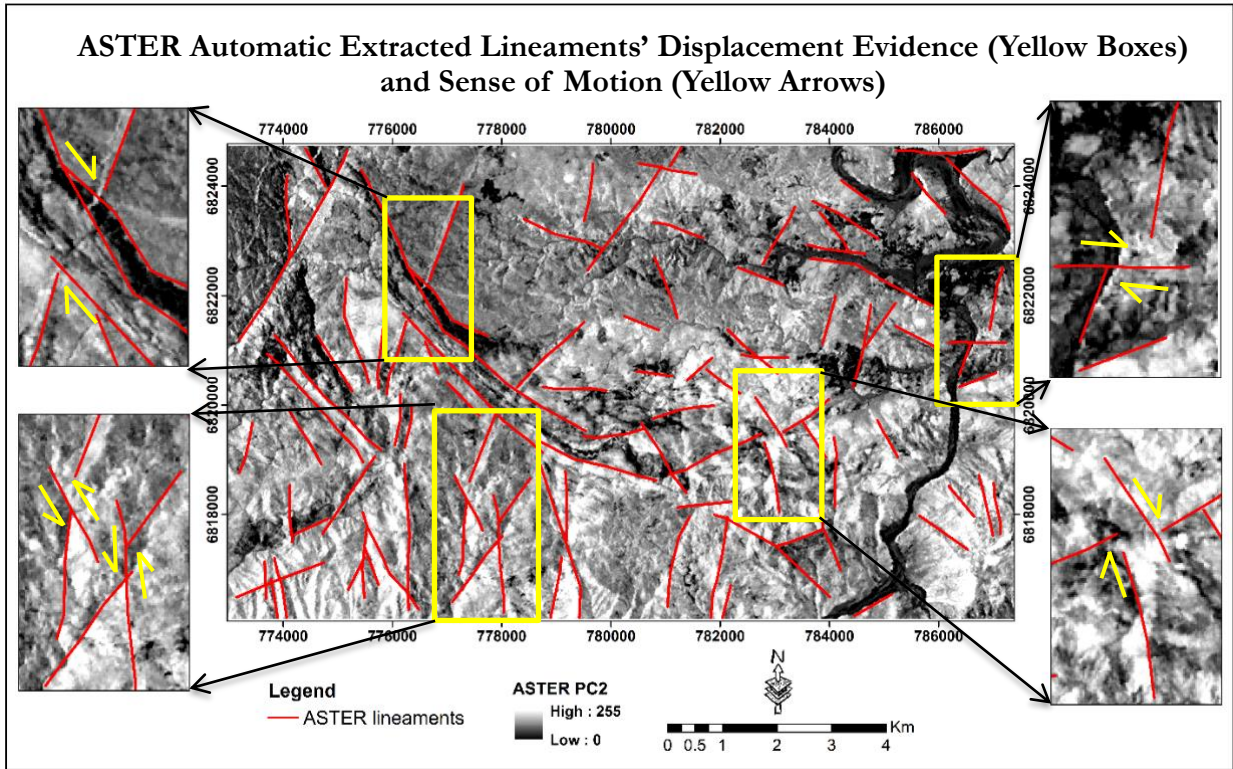
APPENDIX II: CORRESPONDING LINEAMENTS WITH THE PUBLISHED FAULTS ON THE GEOLOGICAL MAP



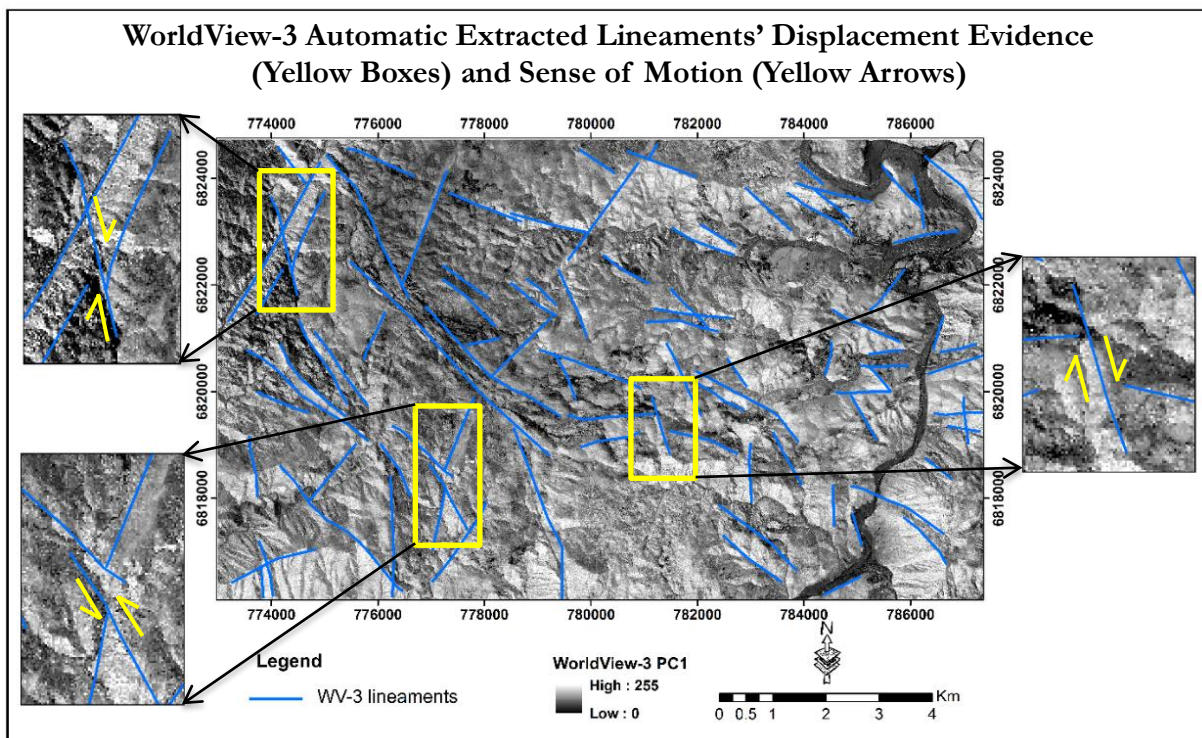
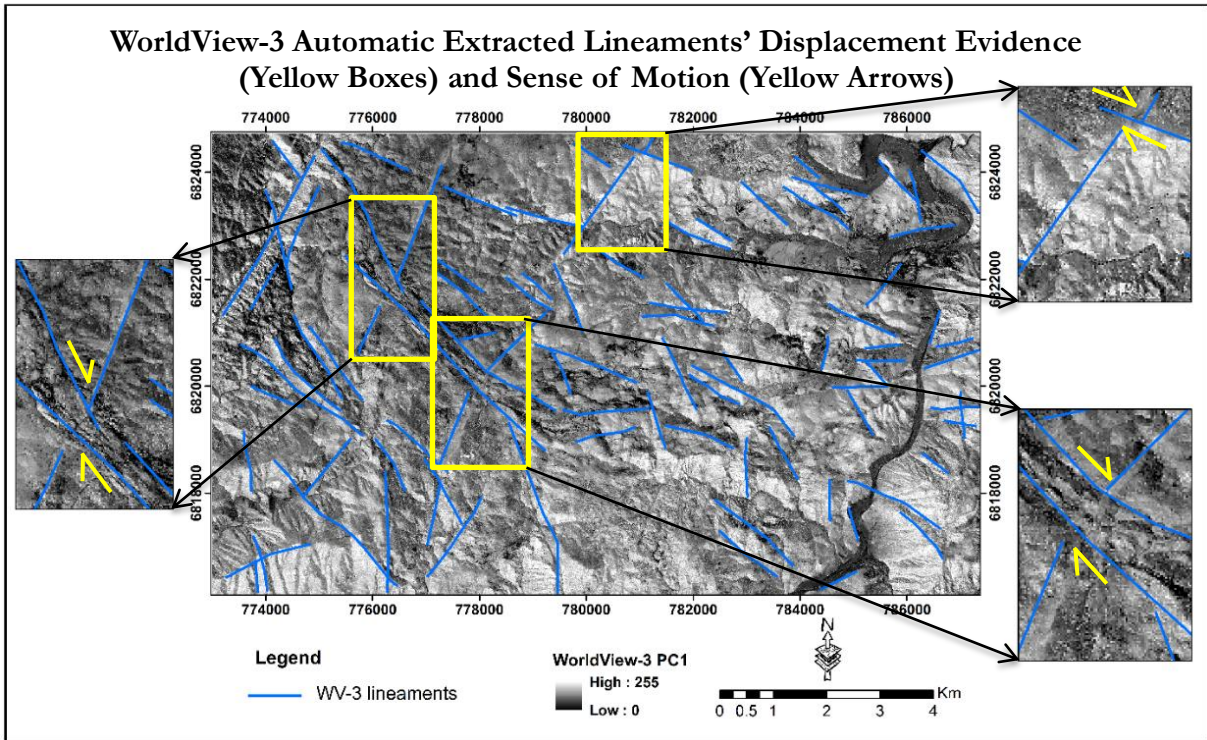
APPENDIX II: CORRESPONDING LINEAMENTS WITH THE PUBLISHED FAULTS ON THE GEOLOGICAL MAP



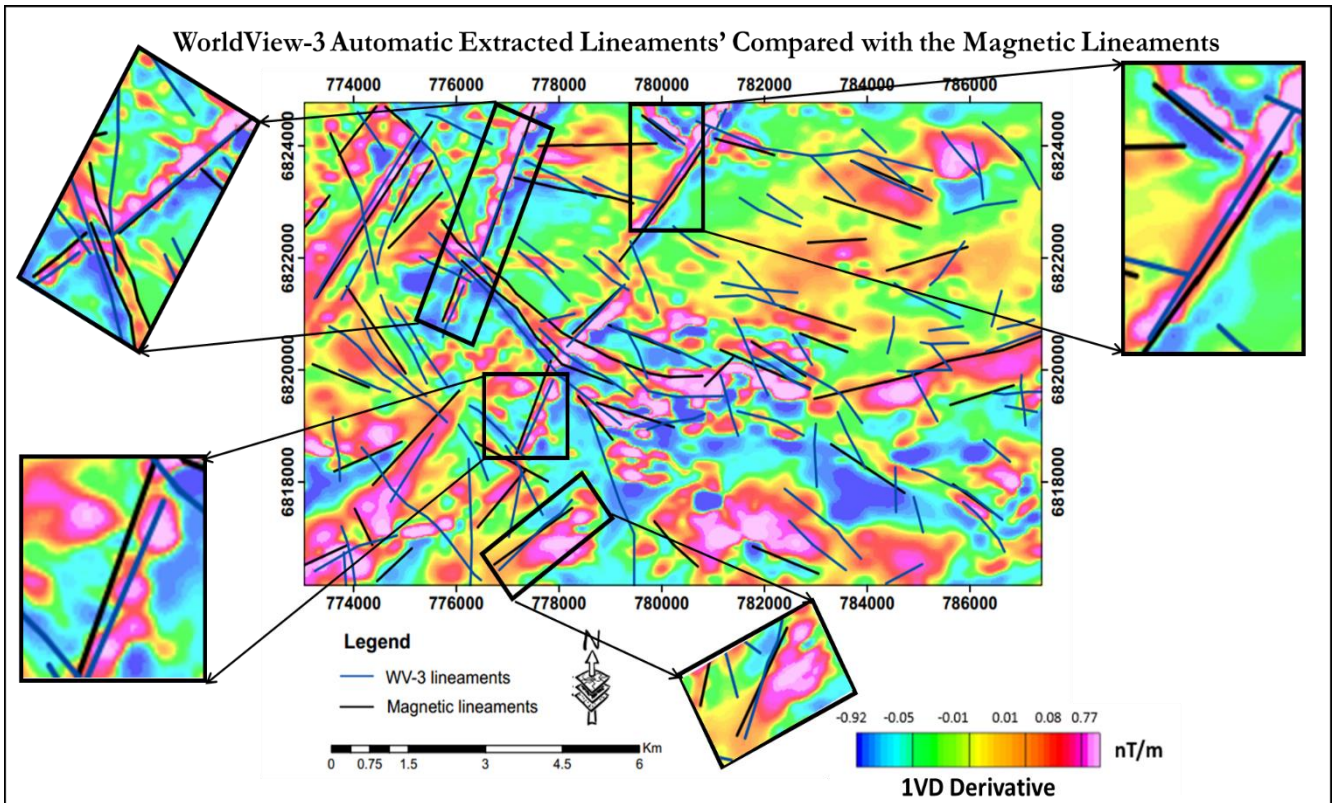
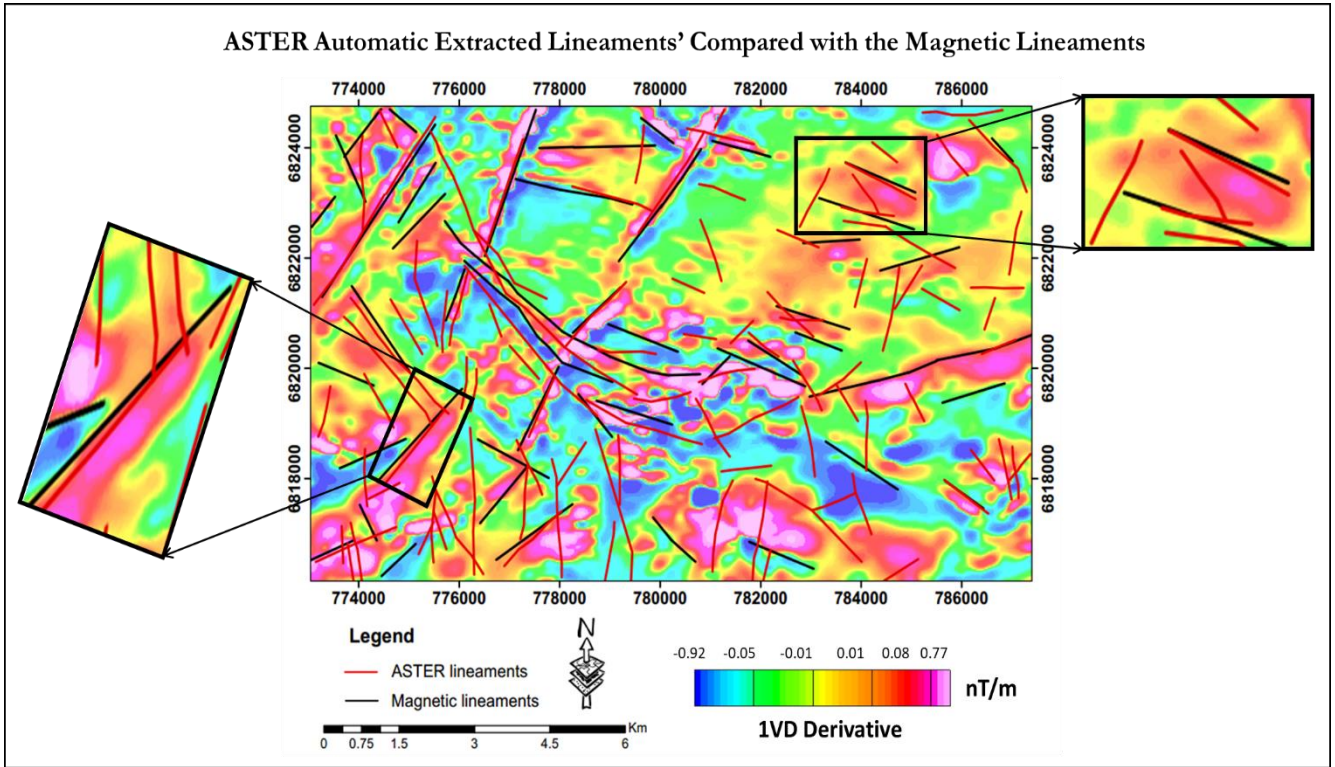
APPENDIX III: LINEAMENTS' EVIDENCE DISPLACEMENT SHOWING SENSE OF MOVEMENT



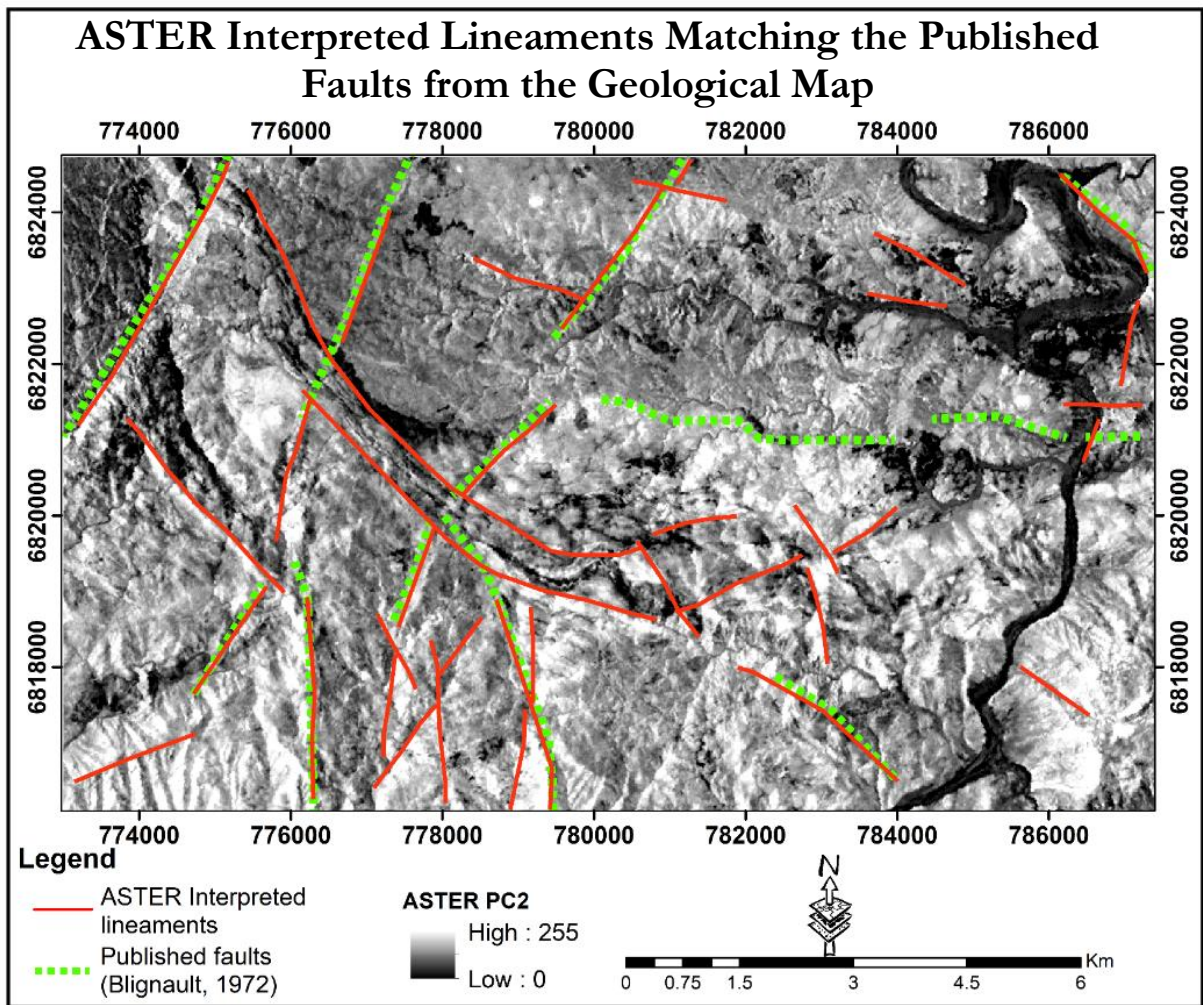
APPENDIX III: LINEAMENTS' EVIDENCE DISPLACEMENT SHOWING SENSE OF MOVEMENT



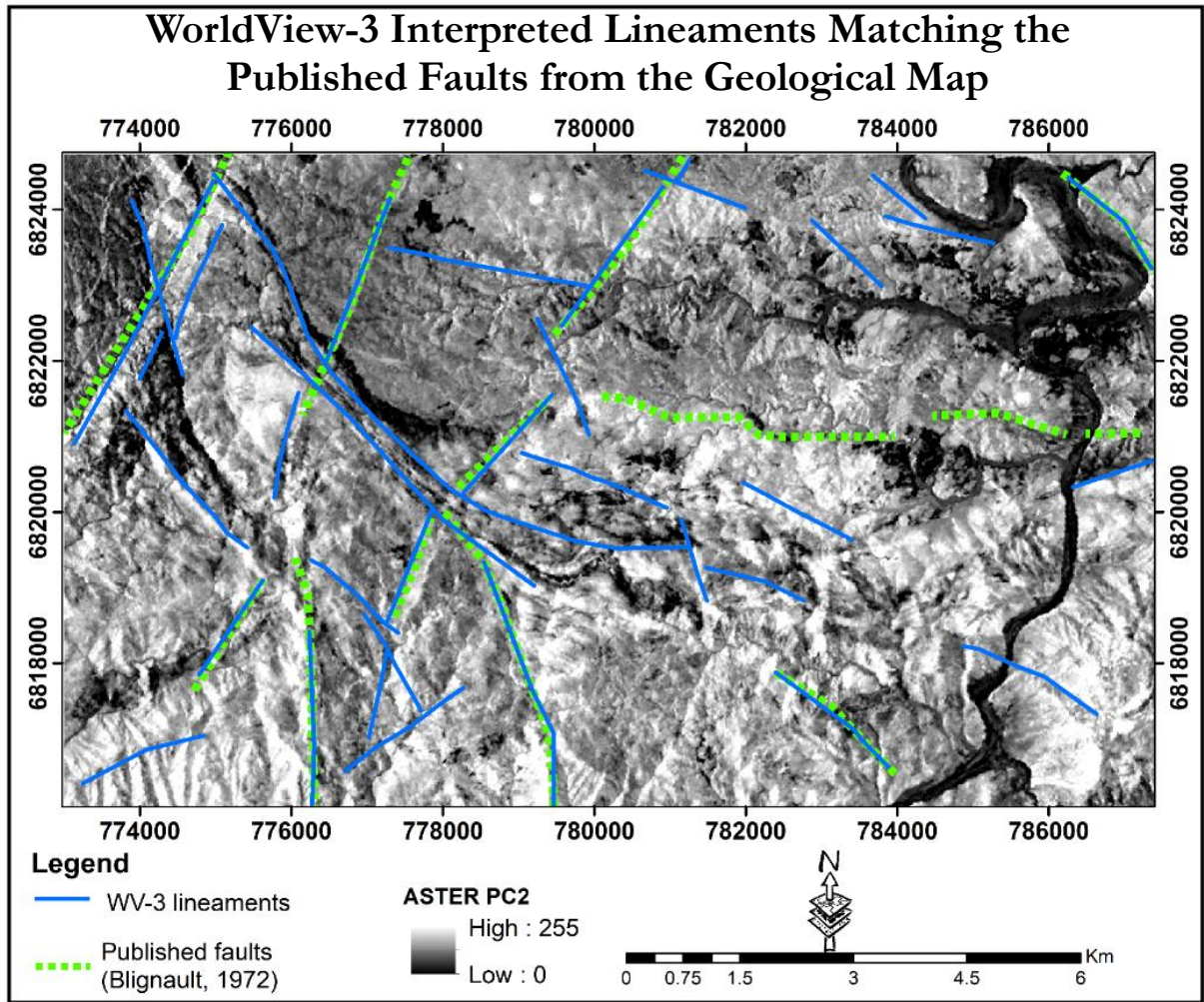
APPENDIX IV: COLLOCATED LINEAMENTS WITH THE MAGNETIC DELINEATED LINEAMENTS



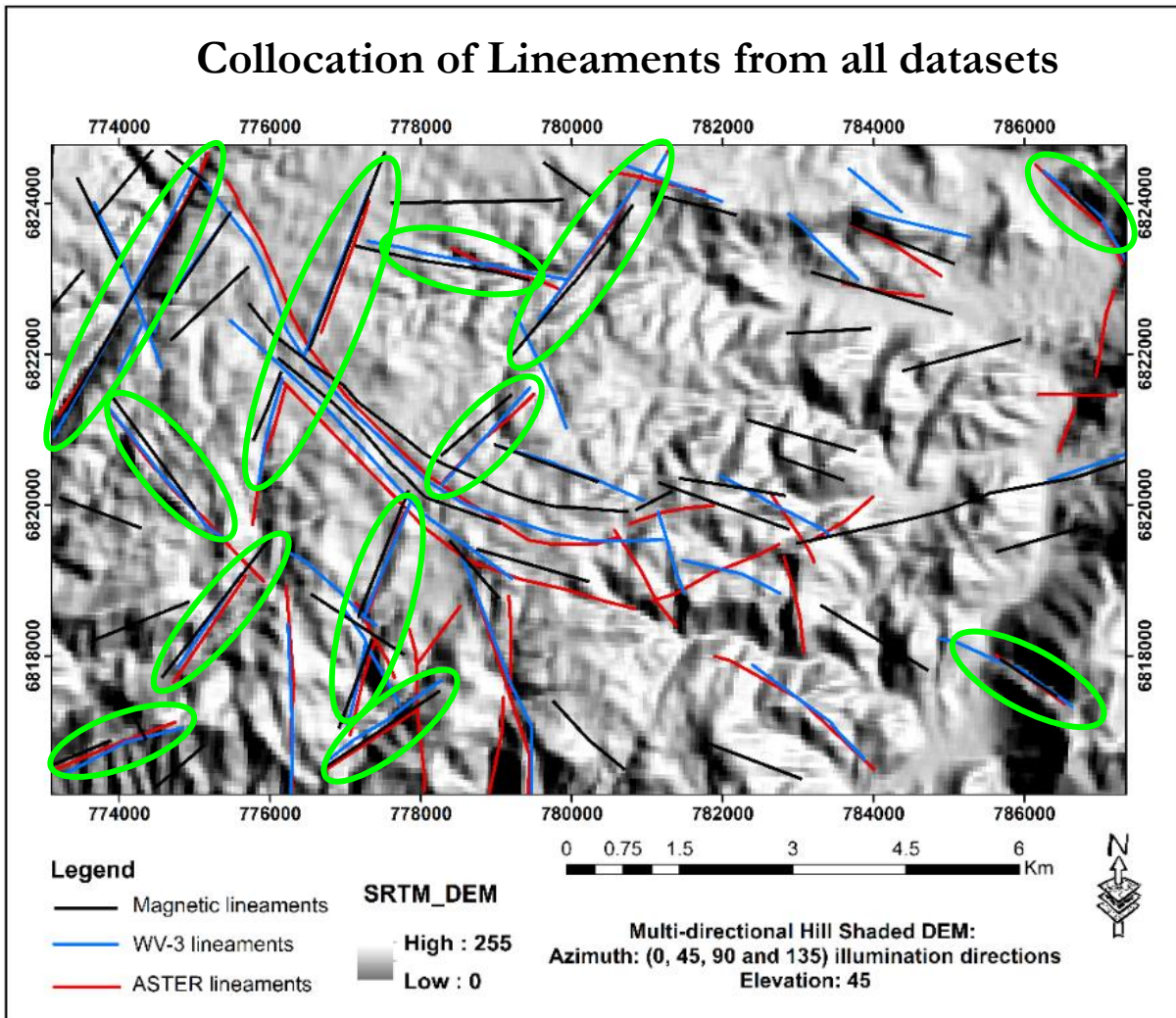
APPENDIX V: INTERPRETED LINEAMENTS CORRESPOND WITH THE PUBLISHED FAULTS ON THE GEOLOGICAL MAP



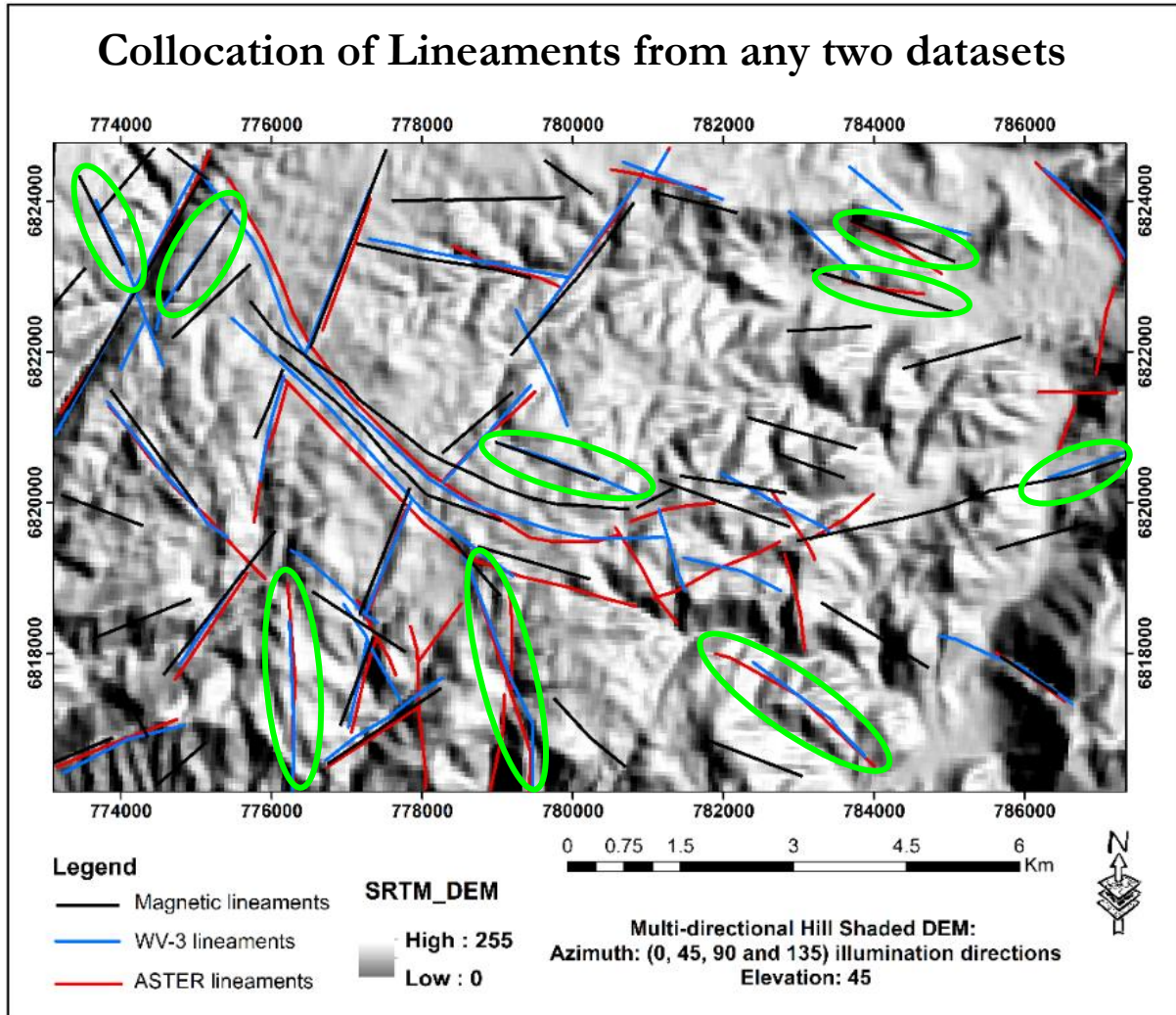
APPENDIX V: INTERPRETED LINEAMENTS CORRESPOND WITH THE PUBLISHED FAULTS ON THE GEOLOGICAL MAP



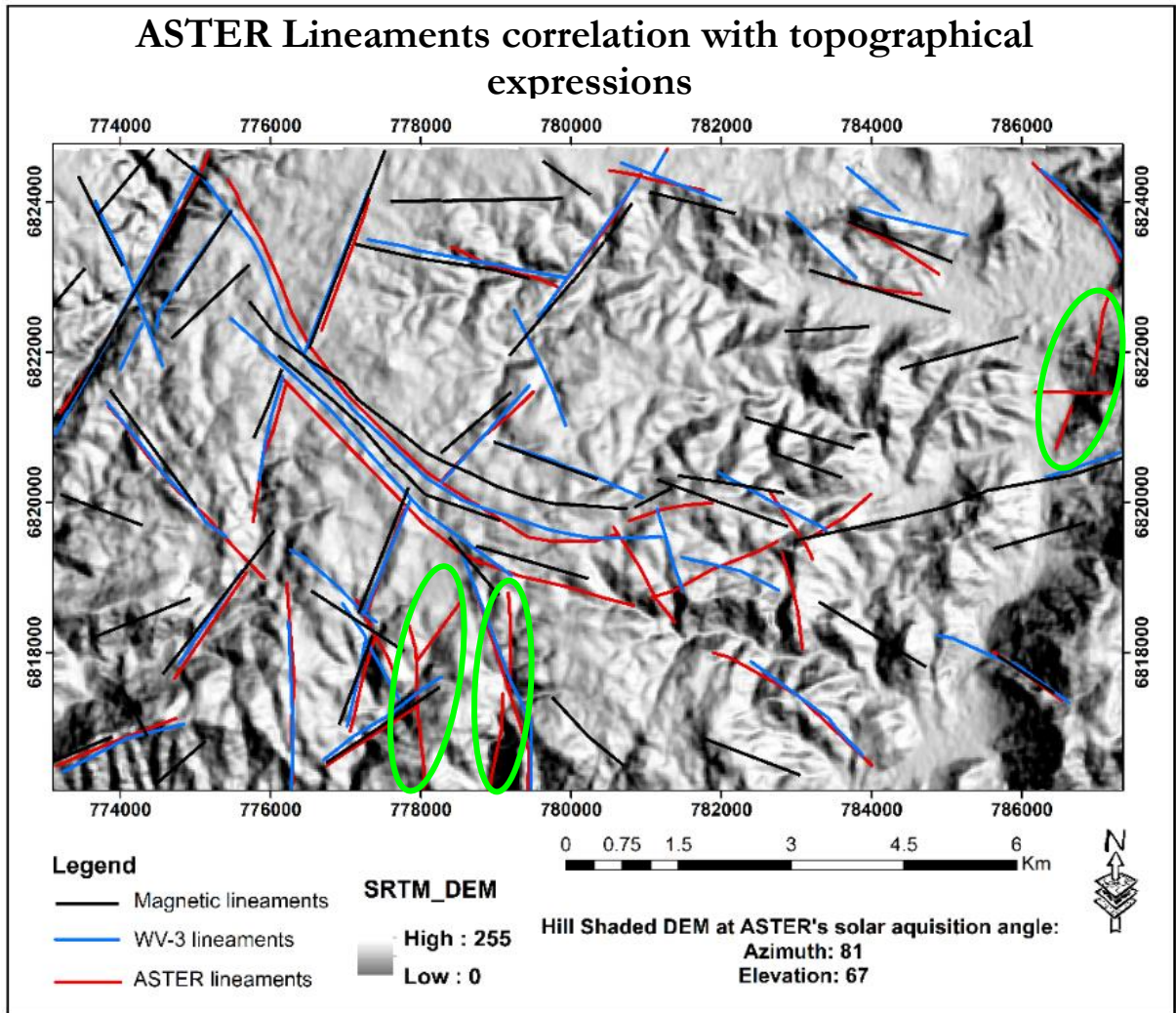
APPENDIX VI: COLLOCATION OF LINEAMENTS



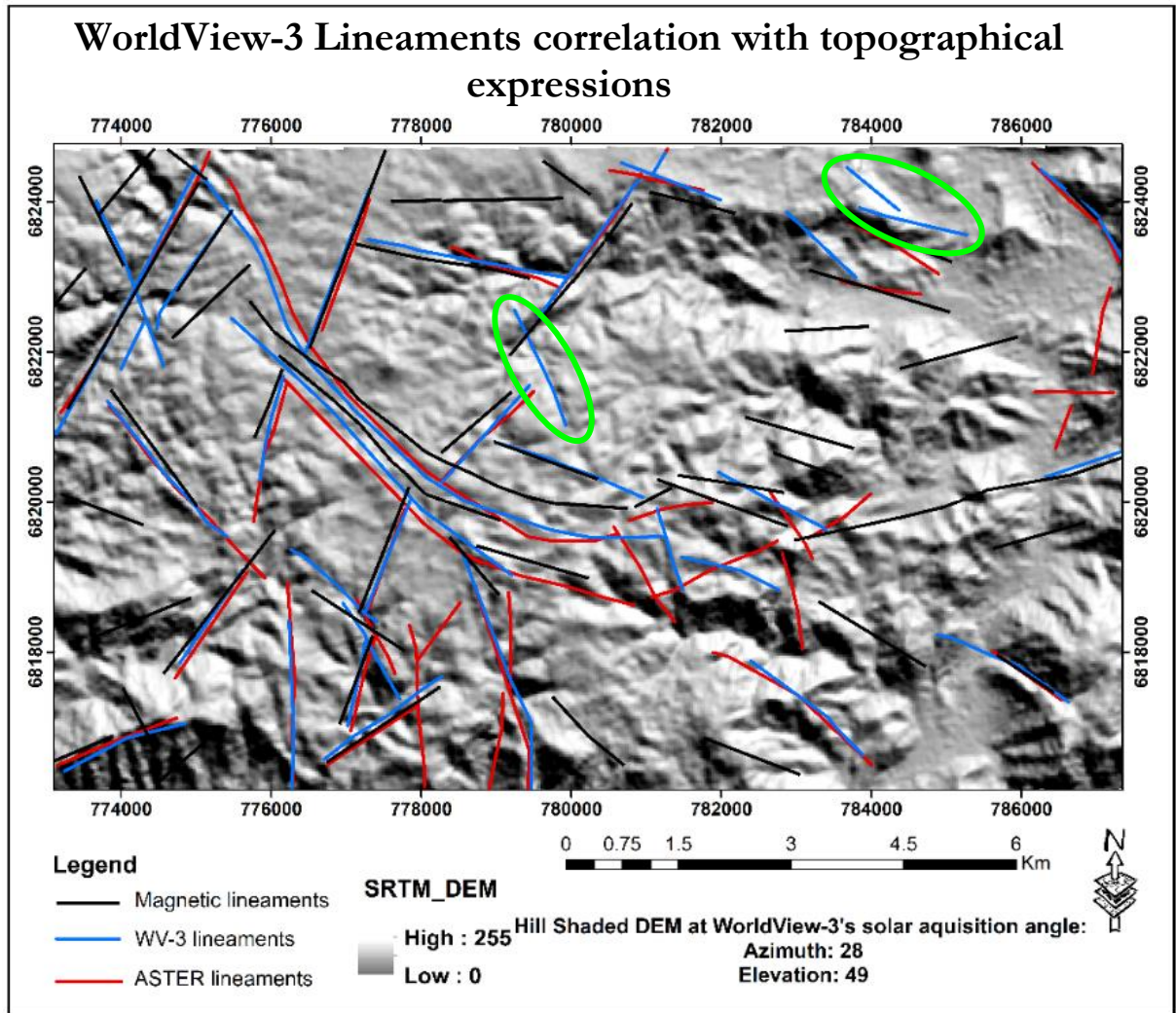
APPENDIX VI: COLLOCATION OF LINEAMENTS



APPENDIX VII: LINEAMENTS CORRELATION WITH TOPOGRAPHICAL EXPRESSIONS



APPENDIX VII: LINEAMENTS CORRELATION WITH TOPOGRAPHICAL EXPRESSIONS



APPENDIX VIII: SUMMARY OF THE TECTONIC ACTIVITIES IN THE HAIB AREA

Event	Mechanism/Characteristics	Period (Ga)	Reference
<ul style="list-style-type: none"> • Magmatism/Volcanism and plutonism 	<ul style="list-style-type: none"> • Intrusions and • Emplacement of Orange River Group (ORG) 	<ul style="list-style-type: none"> • Early 2.0 	<ul style="list-style-type: none"> • Barr & Reid 1992 • Thomas et al., 1993 • Thomas & Cornell 1994 • Blignault et al., 1983
<ul style="list-style-type: none"> • Orange River Orogeny (Eburnean Event) 	<ul style="list-style-type: none"> • Collision of San Francisco and Congolian Cratons – amalgamation – (Compression) • NW-SE tectonic force direction • Ductile strike-slip shearing and faulting, folding • Low grade greenschist metamorphism 	<ul style="list-style-type: none"> • 2.0 – 1.7 	<ul style="list-style-type: none"> • Thomas et al., 1993 • Macey 2017 • Petterson 2008 • Becker et al., 2006 • Begg et al., 2009
<ul style="list-style-type: none"> • Magmatism & plutonic intrusion • Hydrothermal Alteration 	<ul style="list-style-type: none"> • Intrusion of Viooldrift and Richtersveld Intrusive Suite • Haib copper porphyry mineralization 	<ul style="list-style-type: none"> • 1.9 – 1.7 • 1.7 – 1.6 	<ul style="list-style-type: none"> • Barr & Reid 1992 • Eglington 2006 • Reid 1977
<ul style="list-style-type: none"> • Namaquan Wilson Cycle 	<ul style="list-style-type: none"> • rifting, extension, ocean spreading and subduction phases 	<ul style="list-style-type: none"> • 1.6 – 1.4 	<ul style="list-style-type: none"> • (Cornell et al., 2006)
<ul style="list-style-type: none"> • Namaqua Orogeny (Kibaran Event) 	<ul style="list-style-type: none"> • Continental collision of Namaqualand and Kaapvaal Craton – amalgamation (Compression) • Strike-slip, ductile shearing, Folding, Thrusting • NE-SW tectonic direction with Crustal Extensional • Continued greenschist metamorphism • Overprinting Orange River Orogeny structures and all igneous assemblages 	<ul style="list-style-type: none"> • 1.4 – 1.1 	<ul style="list-style-type: none"> • Thomas et al., 1993 • Blignault 1983 • Reid 1987 • Colliston & Schoch 2006 • Becker 2006 • Sithole 2013 • Begg et al., 2009

APPENDIX VIII: SUMMARY OF THE TECTONIC EVOLUTION AND GEODYNAMICS OF THE HAIB AREA AND DATA SPECIFICATIONS

Summary of the tectonic evolution and geodynamics of the Haib area (based on this study, Barr & Reid, 1992; Cornell et al., 2006 and Sithole 2013)

Event	TIME		
	2.0 Ga	1.7 Ga	1.4 – 1.1 Ga
Magmatism/intrusion Volcanism/Plutonism	Orange River Group ----- Vioolsdrift and Richtersveld Intrusive Suites -----		
Orange River Orogeny (Eburnean Event)	----- Early Shearing – deformation ----- Compression, strike-slip shearing and faulting, folding Low grade metamorphism-Regional Greenschist Facies		
Alteration Mineralization	----- Haib Copper Porphyry Mineralization -----		
Namaquan Wilson Cycle	----- Rifting, crustal extension, ocean spreading -----		
Namaqua Orogeny (Kibaran Event)	----- Early and Late shearing – deformation ----- Compression, strike-slip shearing and faulting, folding, Thrusting, Greenschist metamorphism, continued crustal extensional component		

Detailed specifications of the data used in this research

Data/Imagery	ID	Product level	Swath width (Km)	subsystem	No. Bands	Spatial resolution	Acquisition date/year	Source	Availability
WorldView-3	18APR10093714	Radiance at sensor	13.1	VNIR	8	1.2	10 th April 2018	DigitalGlobe Foundation	Commercial
WorldView-3	18APR10093649	Radiance at sensor	13.1	VNIR	8	1.2	10 th April 2018	DigitalGlobe Foundation	Commercial
ASTER	AST_07XT3236	Surface reflectance	60	VNIR	3	15	9 th December 2005	NASA Earthdata	Free
ASTER	AST_07XT1495	Surface reflectance	60	VNIR	3	15	18 th December 2005	NASA Earthdata	Free
ASTER	AST_07XT4921	Surface reflectance	60	SWIR	6	30	9 th December 2005	NASA Earthdata	Free
ASTER	AST_07XT5224	Surface reflectance	60	SWIR	6	30	18 th December 2005	NASA Earthdata	Free
SRTM	s8_e011_1arc_v3.	-	-	TOPSAR	-	30	8 th September 2011	NASA Earth Explorer	Free
Magnetics	Haib_Magnetics	TMI	-	-	-	50	1994	GSN	Commercial